

Instantaneous Coulomb Interactions of Fermions on Graphene's Honeycomb Lattice

MASTER THESIS

Katja Kleeberg

August 2015

Prof. Dr. Lorenz von Smekal

Institut für Theoretische Physik I

Fachbereich 07-Mathematik und Informatik,

Physik, Geographie

JUSTUS-LIEBIG-



UNIVERSITÄT
GIESSEN

Contents

1. Introduction	4
2. Theoretical Background	7
2.1. Structure and Properties of Graphene	7
2.2. Tight-Binding Model	9
2.3. Chiral Symmetry Breaking and Dynamical Mass Generation in (2+1) Dimensions	11
2.4. The Dyson-Schwinger Equations (DSE's)	12
3. Dressing Functions	15
3.1. The Free Hamiltonian	15
3.2. Extraction of the Dressing Functions	15
4. Photon Propagator	18
4.1. Instantaneous Coulomb Interactions	18
4.1.1. Diagrammatic Representation	18
4.2. Transforming the Potential into Position Space	19
4.3. Periodic Potential	21
5. Numerical Methods	25
5.1. Discretization of the Brioullin Zone	25
5.2. Iteration Method	26
5.3. Quasi-Newton Method	27
5.4. Convolution Method	28
5.5. Parallelization with OpenCL	30
5.6. Runtime Comparison	31
6. Mass Renormalization	33
6.1. Finite Volume Effects and Convergence	33
6.2. Critical Coupling	35
6.3. Energy Dispersion	38
7. Fermi-velocity Renormalization	41
7.1. Converting the Hamiltonian to a smaller Unit Cell	41
7.2. Coulomb Potential on the new Lattice	46
7.3. Validation of the new Basis (Basis 2)	51
7.4. Renormalization of the Structure Function	53
8. Inclusion of Screening Effects	59
8.1. Partially Screened Potential	59
8.2. Renormalization	62
9. Conclusion and Outlook	65
A. Tight-Binding Model	67

B. Conventions and Relations	70
B.1. Basis 1	70
B.2. Basis 2	71
C. Comparison to the Dirac-cone Approximation	73
D. Fourier Transform and Convolution Theorem	75
E. Discrete Potential	76

1. Introduction

Graphene is a genuine two dimensional material with unique electronic and mechanical properties. It consists of carbon atoms arranged in a honeycomb lattice, building the basis for all the carbon allotropes like buckyballs (0d), nanotubes (1d) or graphite (3d).

Since the fundamental theoretical studies of the band structure of graphene from P. R. Wallace in 1947 [1], graphene was introduced as a semimetal with zero activation energy and peculiar energy-momentum relation.

Nevertheless it has been argued for a long time that a two dimensional crystal is thermodynamically unstable [2] until the graphene monolayer was synthesized in 2004 [3] by Novoselov and Geim (Nobel prize 2010).

Now, it is generally accepted that it is a material with quite high crystal quality [4] that can be produced by chemical vapour deposition or micromechanical cleavage of graphite [2]. It has a high potential for chemical modification [2] and various electrical applications [5].

The consideration of this work is based on the assumption that the p_z -electrons of graphene (being mainly responsible for the electronic properties of graphene) can be well described within a tight-binding approximation. This standard procedure presumes that the charge carriers are tightly bonded to their atomic kernel. Treating graphene in a tight-binding approach leads to a particular energy-momentum relation where the Fermi surface for neutral graphene reduces to two independent points in the Brioullin zone. In a low energy description an expansion around these points called Dirac points seems to be reasonable (Dirac-cone approximation). In this theory the low-energy excitations behave like relativistic Dirac particles, from which a quantum field theoretical model can be derived [6], where the basic low-energy approximation becomes exact at the Dirac points.

So graphene serves as a real model in which quantum electrodynamical effects in 3 space-time dimensions QED₃ can be studied. This low-energy approach provides an easy acces to the theoretical description and confirms the results of this work but is not applied here (see Appendix C for comparison). In this work the whole band structure and accordingly the complete energy regime of graphene is taken into account.

Graphene can be described by two independent sublattices forming the honeycomb lattice. Anyway, this two component basis of graphenes lattice demands for a spinor representation of the theory analogously to the spin formalism in quantum electrodynamics, for that reason the quantum number that takes this lattices symmetry into account is referred to as pseudo spin. Due to the two resulting independent Dirac points in momentum space the theory exhibits a valley symmetry similar to a chiral symmetry in ordinary QED₃ [6].

Breaking this symmetry would lead to the generation of a mass gap in the band structure of graphene (in analogy to chiral symmetry breaking of QED₃). That would turn graphene into an insulator phase. The existence of such a gap in the energy-momentum relation would be for example important with regard to the application of graphene as transistor material [7]. This phase transition between the semimetal and insulator phase for suspended graphene will be investigated in this work.

The Coulomb interaction between the electrons is introduced by an instantaneous approximation since the Fermi velocity is expected to be much smaller than the speed of light ($v_f/c \sim 1/300$) [8]. If the Coulomb interactions are strong enough (e.g. the coupling constant is large enough) the mentioned gap which turns graphene into the insulator phase can be generated at a certain critical point α_c . The physically realizable coupling values range up to $\alpha = e^2/4\pi\epsilon v_f \approx 2.2$ for suspended graphene ($\epsilon = 1$) [9], in natural units. Many theoretical models that describe the semimetal-insulator phase transition of graphene predicted critical coupling

values well below the limit of $\alpha \approx 2.2$ what is contradictory to the experimental finding that graphene stays in the semimetal phase [10]. So, a long time theoretical physicists were not able to explain that graphene experimentally behaves like a semimetal.

This has changed with the introduction of a more realistic potential based on phenomenological studies [11]. This potential was embedded in Hybrid-Monte-Carlo (HMC) simulations, where the phase transition can be located within the framework of lattice field theories [12, 13, 9]. This simulations, based on the evaluation of the euclidean path integral for interacting systems offer another access to the investigation of the semimetal-insulator phase transition of graphene. In Ref. [9] this has been elaborated in detail. Ultimately they were able to reproduce critical couplings above $\alpha \approx 2.2$ by applying the mentioned phenomenological potential with a smooth change into a long range Coulomb potential.

This settings should be simulated with the completely new approach of Dyson-Schwinger equations (DSE's) on the hexagonal lattice without low-energy approximation.

The thesis is organized as follows: In chapter 2 the general structure of graphene is introduced, as well as the tight-binding model forming the basis of the calculations. Furthermore the mechanism of chiral symmetry breaking within the relativistic quantum field theory is explained and the Dyson-Schwinger equations are developed diagrammatically.

In the next chapter the dressing functions are deduced with help of the Dyson-Schwinger equations and the free Hamiltonian of the theory within a static approximation is constructed. In the following chapter 4 the photon propagator has been developed in an instantaneous approximation, neglecting retardation effects. The potential has to be described periodically and symmetrically inside the Brioullin zone (smallest symmetry unit in momentum space) in order to respect the whole lattice symmetries of the graphene sheet and establish a comprehensive theory. This photon propagator was also converted into position space to prepare the application of the mentioned potential on the basis of the work from Ref. [11].

In chapter 5 the appropriate numerical methods are represented and compared with each other. In the following chapters the results are explained and illustrated in detail. For that, in chapter 6 at first the mass renormalization function is examined in the framework of Dyson-Schwinger equations within the tight-binding approach. The value of the critical coupling for the considered model can be extracted analytically and yields $\alpha_c = 0.457$ [14].

This value could also be calculated in the Dirac-cone approximation [15]; it is cutoff independent and should therefore provide the validation of the calculation techniques used here. After that validation and the evidence for a scaling behaviour similar to that of a phase transition of Miransky-type, also the renormalization of the Fermi-velocity (chapter 7) was taken into account. Here one gets some real difficulties considering the choice of the lattice describing the honeycomb lattice in position space. This problem is solved by the conversion of the whole formalism onto a smaller lattice in position space. This new formalism was again validated with help of the analytically obtained value for the critical coupling by neglecting the Fermi-velocity renormalization. Afterwards the Fermi-velocity renormalization has been introduced and the energy gap was calculated. This yields a critical coupling of about: $\alpha_c \approx 0.8$.

In chapter 8 the screening effects of the σ -bands and other inner electron orbitals are taking into account, excepting the screening effects from the π -bands themselves. This consideration is based on the mentioned phenomenological potential, that has already lead to success in case of the mentioned HMC simulations [13, 9]. Here a critical coupling of about $\alpha \approx 1.5$ has been found.

To take the screening effects of the π -bands among themselves into account, the so called Lindhard-function [16, 17] has to be dynamically included in the calculations. The Lindhard-function can be introduced analogically to a vacuum-polarization in QED_3 (see also Ref. [15])

but was not included in the calculations yet.

In a final step (chapter 9), the results are summarized and the widely ranged possibilities of this new ansatz are exhibited.

2. Theoretical Background

2.1. Structure and Properties of Graphene

Graphene is a one atom thick layer of carbon atoms arranged in a honeycomb lattice. It serves as the foundation of various allotropes of carbon. In fullerenes graphene is wrapped-up to a spherically structure (introducing pentagons). Rolling graphene provides nanotubes and by stacking graphene monolayers on each other graphite can be obtained [4]. The different carbon allotropes are illustrated in Fig. 1 and are also of high industrial interest.

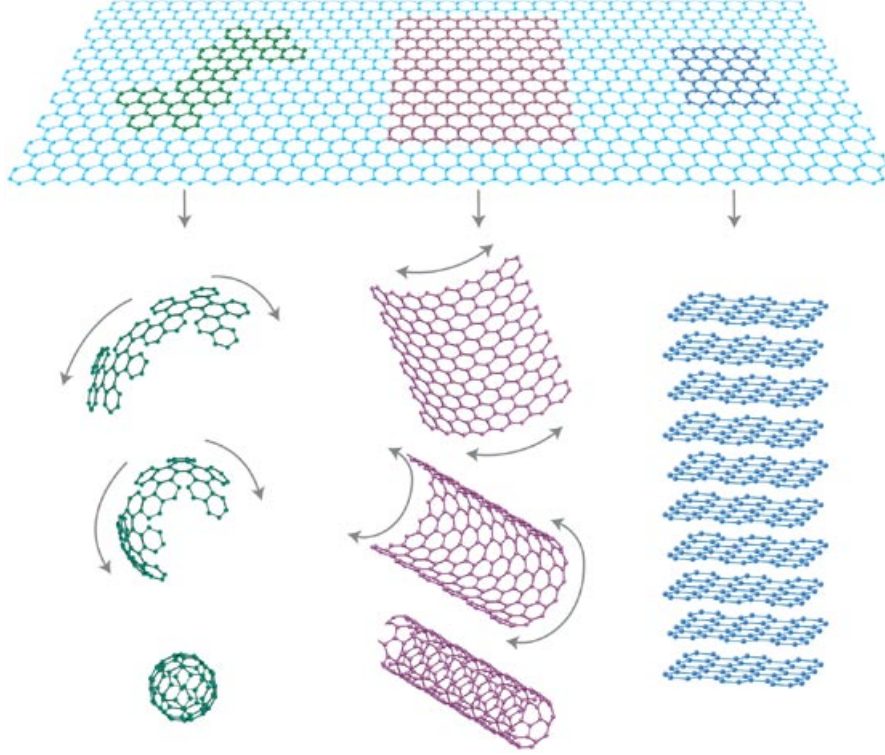


Figure 1: The figure shows allotropes of graphene, taken from [2].

In this work the main focus is placed on the composition and properties of graphene. In Fig. 2 the structure of graphenes honeycomb basis is depicted, it is composed of two independent triangular sublattices denoted by A and B respectively.

One carbon atom has four valence electrons, three of them form covalent σ -bonds in terms of an sp^2 -hybridization of the atomic orbitals ($2s$, $2p_x$ and $2p_y$) [6]. These flexible bonds keep the single carbon atoms together and are responsible for the various carbon structures presented above. The remaining p_z -electrons of the carbon atoms are forming two additional π -bands which are mainly responsible for the electronic properties of graphene. Assuming that this electrons are tightly bonded to their atomic kernel, they can be described within a tight-binding model that is introduced in the next section (see also Appendix A).

The two basis vectors of the triangular sublattices (Fig. 2) are given by

$$\vec{a}_1 = \frac{a}{2} \begin{pmatrix} \sqrt{3} \\ 3 \end{pmatrix}, \quad \vec{a}_2 = \frac{a}{2} \begin{pmatrix} \sqrt{3} \\ -3 \end{pmatrix}, \quad (2.1)$$

with the interatomic distance $a = 1.42 \text{ \AA}$ [5] between two carbon atoms. In this notation the nearest-neighbour vectors, also shown in Fig. 2, can be written as

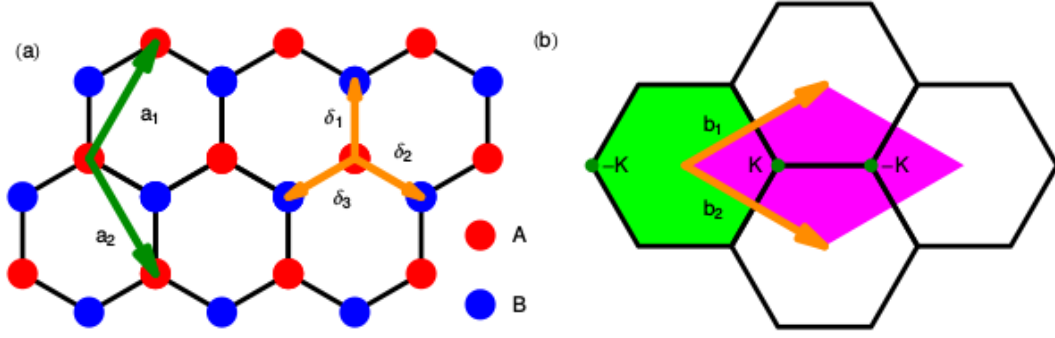


Figure 2: (a) The honeycomb lattice, resulting from a superposition of two independent triangular lattices A and B is illustrated. The two basis vectors are denoted by a_1 and a_2 and the vectors linking to the next carbon atoms are referred to as δ_i , where $i = \{1, 2, 3\}$. (b) Shows the reciprocal lattice with the green honeycomb cell illustrating the first Brillouin zone (BZ) and the pink rhomboid being a reduction of the second Brillouin zone. The picture was taken from Ref. [6].

$$\vec{\delta}_1 = \begin{pmatrix} 0 \\ a \end{pmatrix}, \quad \vec{\delta}_2 = \frac{a}{2} \begin{pmatrix} \sqrt{3} \\ -1 \end{pmatrix}, \quad \vec{\delta}_3 = \frac{a}{2} \begin{pmatrix} -\sqrt{3} \\ -1 \end{pmatrix}. \quad (2.2)$$

A short summary of this basis (Basis 1) can be found in Appendix B.1.

On the right hand side of Fig. 2, the appropriate reciprocal lattice vectors in momentum space are illustrated. Here the rhombic basis vectors in position space are leading to a hexagonal lattice in momentum space (green Brillouin zone). The reciprocal basis vectors denoted by \vec{b}_1 and \vec{b}_2 can be calculated via $a_i b_j = 2\pi \delta_{ij}$, yielding

$$\vec{b}_1 = \frac{2\pi}{3a} \begin{pmatrix} \sqrt{3} \\ 1 \end{pmatrix} \quad \text{and} \quad \vec{b}_2 = \frac{2\pi}{3a} \begin{pmatrix} \sqrt{3} \\ -1 \end{pmatrix}. \quad (2.3)$$

The green honeycomb in Fig. 2 illustrates the first BZ, while the pink rhomboid results from a reduction of the second BZ. Anyway, these two different descriptions are equivalent but the rhombic BZ will provide an important simplification for the further calculations.

From the sublattice structure in real space follows that there are two independent lattice points in momentum space, belonging to one BZ. These two points, called Dirac points, are playing an important role in the theoretical consideration of graphene. Their positions in momentum space are given by

$$K_{\pm} = \pm \frac{2\pi}{3a} \begin{pmatrix} 2/\sqrt{3} \\ 0 \end{pmatrix}. \quad (2.4)$$

This is the most common representation of the honeycomb lattice and the resulting BZ. The lattice in position space is decomposed in two sublattices, accepting a two component basis structure in momentum space (K^+ , K^-). In subsequent chapters it is shown that this choice of the basis is involving serious difficulties.

2.2. Tight-Binding Model

Based on the assumption that the electrons of the remaining p_z -orbitals (forming π -bands) are tightly bonded to their atomic kernel, we can start with the Hamiltonian for a tight-binding model in second quantization, which is derived in Appendix A and expresses that an electron is hopping from one site to an adjacent one (annihilated at one carbon atom and created at an adjacent site of the other sublattice or vice versa), as described by

$$\mathcal{H}_0 = -\kappa \sum_{\langle i,j \rangle} (a_i^\dagger b_j + b_j^\dagger a_i). \quad (2.5)$$

So a , a^\dagger and b , b^\dagger are the creation and annihilation operators for the respective sublattices. κ is referred to as the hopping parameter and determines the probability for an electron to hop from one carbon atom to an adjacent one. This is clear due to the notation in second quantization. It was experimentally fixed to a value of $\kappa = 2.8$ eV [5].

By performing a Fourier transform into momentum space with the operators [6]

$$a_i = \sqrt{\mathcal{AZ}} \int_{\mathcal{BZ}} \frac{d^2 k}{(2\pi)^2} e^{i\vec{k}\vec{r}_i} a_k \quad (2.6)$$

$$b_i = \sqrt{\mathcal{AZ}} \int_{\mathcal{BZ}} \frac{d^2 k}{(2\pi)^2} e^{i\vec{k}\vec{r}_i} b_k \quad (2.7)$$

and their Hermitian conjugated,¹ the Hamilton operator (2.5) can be described by

$$\mathcal{H}_0 = \mathcal{AZ} \int_{\mathcal{BZ}} \frac{d^2 k}{(2\pi)^2} (a_k^\dagger, b_k^\dagger) H(\vec{k}) \begin{pmatrix} a_k \\ b_k \end{pmatrix}, \quad (2.8)$$

where $\mathcal{AZ} = 3\sqrt{3}a^2/2$ is the unit cell area and the discrete representation of the delta distribution in two dimensions has been used. The area of the Brioullin zone is indicated by \mathcal{BZ} .

The associated Hamiltonian in momentum space yields

$$H(\vec{k}) = \mathbf{b}_1(\vec{k}) \sigma_1 + \mathbf{b}_2(\vec{k}) \sigma_2 = \begin{pmatrix} 0 & -\phi(\vec{k}) \\ -\phi^*(\vec{k}) & 0 \end{pmatrix}. \quad (2.9)$$

The two functions $\mathbf{b}_1(\vec{k})$ and $\mathbf{b}_2(\vec{k})$ are representing the real and imaginary part of the structure function $\phi(\vec{k})$, where

$$\kappa\phi(\vec{k}) = \kappa \sum_{n=1}^3 e^{i\vec{k}\vec{\delta}_n} = -\mathbf{b}_1(\vec{k}) + i \mathbf{b}_2(\vec{k}) \quad (2.10)$$

with

$$|\phi(\vec{k})|^2 = 3 + 2 \cos(\sqrt{3}k_y a) + 4 \cos\left(\frac{\sqrt{3}}{2}k_y a\right) \cos\left(\frac{3}{2}k_x a\right). \quad (2.11)$$

Here $\vec{\delta}_n$ are again the three nearest-neighbour vectors ($n = \{1, 2, 3\}$) of the honeycomb lattice which were already introduced in section 2.1 and σ_i are the Pauli matrices (see Appendix B) with which the matrix can be easily diagonalized by a rotation under conservation of the length of the vector.

Since the Pauli matrices build a basis of the vector space of 2×2 Hermitian matrices, a general

¹The associated backsubstitution is given by a discrete Fourier transform.

Hermitian matrix in two dimensions

$$\mathcal{A} = c\sigma_0 + d\sigma_1 + e\sigma_2 + f\sigma_3, \quad (2.12)$$

has the Eigenvalues:

$$\lambda = c \pm \sqrt{d^2 + e^2 + f^2}. \quad (2.13)$$

This procedure simply provides the Eigenvalues and hence the single particle energies of the Hamiltonian in Eq. (2.9):

$$E_{\pm}^{(0)}(\vec{k}) = \pm \kappa |\phi(\vec{k})|. \quad (2.14)$$

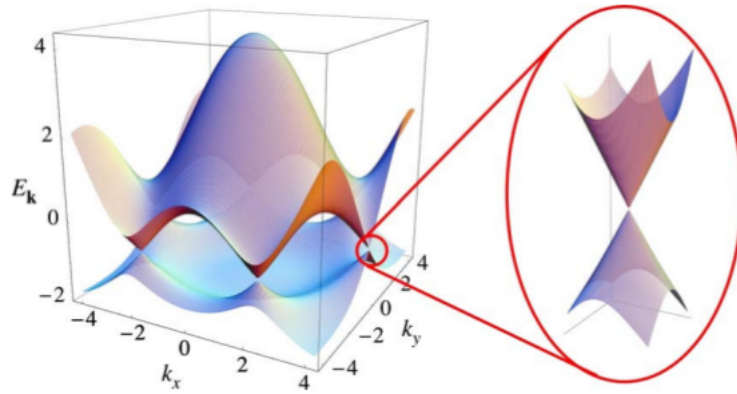


Figure 3: The dispersion relation for graphenes honeycomb lattice for $\kappa = 2.7$ eV and $\kappa' = -0.2$ t is shown, taken from [4]. On the right hand side a zoom of the band structure near a Dirac point is illustrated.

The dispersion relation (2.14) is illustrated in Fig. 3. It consists of two energy bands that can be interpreted as electron and hole states. The upper and lower band are touching each other in six points at the Fermi level, separating the valence from the conduction band. Two of these points, the above mentioned Dirac points, are independent from each other. The remaining points can be converted into each other by the corresponding symmetry transformations of the lattice.

So graphene is forming a semi-conductor with zero activation energy [1] based on the special constellation of carbon atoms in a honeycomb lattice. In Fig. 3 (see Eq. (A.11)) one can see that the symmetry between the valence and conductor band is broken, which is caused by the consideration of the next nearest neighbour potentials (see Appendix A), which are neglected here.

In Fig. 4, on the left hand side the high symmetry points of the Brioullin zone are indicated while the energy dispersion along these symmetry points is illustrated on the right hand side. The vanishing density of states at the Dirac points ensures the long-range character of the Coulomb potential since scattering processes are suppressed due to Pauli exclusion principle. As already mentioned a common ansatz is to expand the structure function near the Dirac points K_{\pm} . This provides the following energy-momentum relation

$$E_{\pm}(q) \approx \pm v_F q + \mathcal{O}[(q/K)^2] \quad (2.15)$$



Figure 4: On the left hand side the high symmetry points of the BZ are illustrated. On the right hand side the energy relation is plotted along these symmetry points [5].

with $v_F = 3\kappa a/2$ being the Fermi velocity and \vec{q} the momentum vector measured relatively to the Dirac point. It equates to a linear dispersion relation as it is known for massless relativistic particles. So this justifies the consideration of such Dirac like particles within a quantum field theory in (2+1) space-time dimensions.

2.3. Chiral Symmetry Breaking and Dynamical Mass Generation in (2+1) Dimensions

In this theory the Fermi velocity v_F takes the role of the velocity of light c . Consequently the appropriate Lagrangian can be easily deduced from quantum electrodynamics in three space-time dimensions (QED₃) [6]

$$\mathcal{L} = \sum_{i=1}^{N_f} \bar{\Psi}_i(t, \vec{r}) [i\hbar \mathcal{D}_0 + i\hbar v_F \gamma^1 \mathcal{D}_1 + i\hbar v_F \gamma^2 \mathcal{D}_2] \Psi_i(t, \vec{r}), \quad (2.16)$$

where $\mathcal{D}_\mu = \partial_\mu - ieA_\mu$ is the covariant derivative [18] and $\bar{\Psi} = \Psi^\dagger \gamma_0$. N_f denotes the different fermion flavours, in the following $N_f = 2$ is considered, which equates to the two possible spin states² $\sigma = \pm 1$. $\Psi_\sigma(t, \vec{r})$ is therefore a four component spinor with sublattice and valley degrees of freedom which can be obtained by the transformation of

$$\Psi_\sigma(\vec{p}) = \begin{pmatrix} \Psi_{\vec{K}_+, \sigma}(\vec{p}) \\ \Psi_{\vec{K}_-, \sigma}(\vec{p}) \end{pmatrix} = \begin{pmatrix} a_\sigma(\vec{K}_+ + \vec{p}) \\ b_\sigma(\vec{K}_+ + \vec{p}) \\ b_\sigma(\vec{K}_- + \vec{p}) \\ a_\sigma(\vec{K}_- + \vec{p}) \end{pmatrix} \quad (2.17)$$

which arise from the expansion at the two Dirac points (see Ref. [6] for a detailed description). Even in QED₃ the 4×4 dimensional γ matrices are needed to construct a chiral symmetry. For that reason we take the common Dirac matrices γ_0, γ_1 and γ_2 as adequate counterparts to the Pauli matrices of a higher dimension. An explicit indication of these matrices can be found in the Appendix of Ref. [19] or Ref. [20]. Accordingly there are two matrices that anticommute with these gamma matrices, which are denoted by γ_3 and γ_5 . On this basis the theory described by equation (2.16) would be invariant under the following transformations

$$\Psi_{K_\pm} \rightarrow e^{i\alpha\gamma_3} \Psi_{K_\pm}, \quad \Psi_{K_\pm} \rightarrow e^{i\alpha\gamma_5} \Psi_{K_\pm}. \quad (2.18)$$

²The different spin states could also be neglected, they merely lead to a doubling of the degrees of freedom. The decisive point is the sublattice-valley symmetry.

So there will be a $U(2)$ symmetry generated by $\mathbb{1}, \gamma_3, \gamma_5$ and $[\gamma_3, \gamma_5]$ for each fermion flavour. Accordingly we remain with a $U(2N_f)$ symmetry. A mass term

$$M \bar{\Psi}_{K_{\pm}} \Psi_{K_{\pm}} \quad (2.19)$$

would break this symmetry down to

$$SU(N_f) \times SU(N_f) \times U(1) \times U(1). \quad (2.20)$$

So this subvalley-lattice symmetry of the low energy description mimics a chiral symmetry and again becomes exact at the Dirac points.

2.4. The Dyson-Schwinger Equations (DSE's)

So if there is a mass gap $M(K_{\pm}) \neq 0$ in the chiral limit, it means that chiral symmetry has been broken and mass is generated. In perturbation theory the mass corrections are proportional to the bare mass in every order, so dynamical mass generation can not be explained by perturbation theory [21]. Taking this into account we have to find a non-perturbative approach to handle phenomena like mass generation. One extensive approach is to work with the quantum field theoretical ansatz of Dyson-Schwinger equations (DSE's) that will be applied to the tight-binding model of graphene in the following chapters.

Due to the primary interest in the electron behaviour the fermionic DSE should be studied for now. A visual access to the Dyson-Schwinger equations is given by considering the contributions to the dressed propagator in terms of their Feynman graphs. Regarding the contributions to the perturbation series

$$\text{---}\bullet\text{---} = \text{---} + \text{---}\text{[fermion loop]}\text{---} + \text{---}\text{[fermion loop]}\text{[fermion loop]}\text{---} + \text{---}\text{[fermion loop]}\text{[photon loop]}\text{---} + \text{---}\text{[photon loop]}\text{[fermion loop]}\text{---} + \text{---}\text{[fermion loop]}\text{[photon loop]}\text{[fermion loop]}\text{---} + \dots$$

it already seems to be reasonable to denote the self-energy by the Feynman diagram represented in equation (2.21).

$$\Sigma(p) = \text{---}\text{[fermion loop]}\text{---} \quad (2.21)$$

Here the dots summarize the single contributions to the photon propagator, the fermion-photon vertex and again the fermion propagator. They illustrate the inclusion of every possible insertion of the appropriate propagator, depicted separately in the diagram above.

So the solid dots represent fully dressed vertices or propagators. It can be shown that the propagator consists of the following self-energy interactions

$$\begin{aligned}
 \text{---}\bullet\text{---} &= \text{---} + \text{---}\text{---}\text{---} + \text{---}\text{---}\text{---}\text{---}\text{---} + \dots \\
 &= \text{---} + \text{---}\text{---}\text{---}
 \end{aligned}$$

That means that we are in principle simply summing up over all orders in perturbation theory. The explicit derivation of the DSE's can be found in [22] or [23]. This leads to the following expression, where $G_F^0(p)$ is the bare fermion propagator and $G_F(p)$ is the dressed one.

$$G_F(p) = G_F^0(p) + G_F^0(p) \Sigma(p) G_F^0(p) + G_F^0(p) \Sigma(p) G_F^0(p) \Sigma(p) G_F^0(p) + \dots \quad (2.22)$$

This is nothing else than a geometric series and can be rewritten as

$$G_F(p) = \frac{G_F^0(p)}{1 - \Sigma(p) G_F^0(p)}. \quad (2.23)$$

By rearranging this equation one gets the common form for the Dyson-Schwinger equation (2.24)

$$G_F(p)^{-1} = G_F^0(p)^{-1} - \Sigma(p) \quad (2.24)$$

which is illustrated in the following Eq. (2.25).

$$\text{---}\bullet\text{---} = \text{---} - \text{---}\text{---}\text{---} \quad (2.25)$$

Writing out Eq. (2.25) with the help of the appropriate Feynman rules yields

$$G_F(p)^{-1} = G_F^0(p)^{-1} - \frac{ie^2}{(2\pi)^4} \int d^4q \, \gamma^\mu G_F(q) \Gamma^\nu(q, p) D_{\mu\nu}(k) \quad (2.26)$$

for the general case of QED in four dimensions [23]. Reducing that to 3 dimensions and handling the complex integration with a Wick Rotation to Euclidean space one obtains the DSE for QED₃ [24]

$$G_F(p)^{-1} = G_F^0(p)^{-1} + \frac{e^2}{(2\pi)^3} \int d^3q \, \gamma_\mu G_F(q) \Gamma_\nu(q, p) D_{\mu\nu}(k), \quad (2.27)$$

with the photon propagator [18]

$$D_{\mu\nu}(p, \xi) = \left(\delta_{\mu\nu} - \frac{p_\mu p_\nu}{p^2} \right) \frac{1}{p^2 (1 + \Pi(p^2))} + \xi \frac{p_\mu p_\nu}{p^4}. \quad (2.28)$$

There are analogous Dyson-Schwinger equations for the dressed photon propagator and the

dressed fermion-boson vertex which cause some remarkable difficulties. All these equations are coupled and with every reference to a higher n -point function one has to take another DSE into account. So they form an infinite tower of coupled integral equations which have to be solved self-consistently. Thus the challenge is to find a systematic truncation procedure to obtain a satisfactory and computable approximation for the fermion propagator. This will be the subject of the following chapters.

3. Dressing Functions

3.1. The Free Hamiltonian

Now, the general description without the low energy approximation should be examined again. In addition to the considered tight-binding Hamiltonian from Eq. (2.8) an explicitly symmetry breaking mass term that generates a gap between valence and conduction band should be introduced.³ It is realized by a staggered chemical potential (analogous to (2.19))

$$\mathcal{H}_{\mu_3} = \mu_3 \sum_i (a_i^\dagger a_i - b_i^\dagger b_i), \quad (3.1)$$

which can arise for example from the environment (e.g. doped substrate) and creates an explicit asymmetry between the two sublattices [5]. It causes a higher charge density either on the A lattice or on the B lattice for $\mu_3 \neq 0$ and therefore gives rise to a charge density wave (CDW) formation.

The basic Hamiltonian is then given by

$$\mathcal{H} = \mathcal{H}_0 + \mathcal{H}_{\mu_3} - \mu \mathcal{N}, \quad (3.2)$$

where the last term assures a finite charge carrier density, with \mathcal{N} being the fermion number operator. It principally shifts the Eigenvalues of the Hamilton operator away from half filling. The associated Hamiltonian in momentum space (see Eq. (2.8)) can be obtained analogically to the calculation of the last section and yields

$$H(\vec{k}) = -\mu\sigma_0 + \mathfrak{b}_1(\vec{k})\sigma_1 + \mathfrak{b}_2(\vec{k})\sigma_2 + \mu_3\sigma_3, \quad (3.3)$$

from which the Eigenvalues and hence the single particle energies of the quasi free Hamiltonian can be simply derived by the same techniques as in the last chapter (Eq. (2.13))

$$E_{\pm}^{(0)}(\vec{k}) = -\mu \pm \sqrt{\kappa^2 |\phi(\vec{k})|^2 + \mu_3^2} = -\mu \pm \sqrt{\mathfrak{b}_1^2(\vec{k}) + \mathfrak{b}_2^2(\vec{k}) + \mu_3^2}. \quad (3.4)$$

Since the structure function is zero at the Dirac points:

$$\phi(K^+) = \phi(K^-) = 0 \quad (3.5)$$

a possible energy gap is caused by a nonzero staggered chemical potential or by its dynamical generation.

3.2. Extraction of the Dressing Functions

On the basis of the free Hamiltonian in momentum space (Eq. (3.3)) we can now introduce an appropriate free fermion propagator by the resolvent, exhibiting the necessary singularities

$$\begin{aligned} G_F^{(0)}(\omega, \vec{k}) &\equiv i(\gamma^0(\omega - H))^{-1} \\ &= \frac{i \left((\omega + \mu) \gamma^0 - \mathfrak{b}_1(\vec{k}) \gamma^1 + \mathfrak{b}_2(\vec{k}) \gamma^2 + \mu_3 \right)}{\left((\omega + \mu) - \mathfrak{b}_1^2(\vec{k}) - \mathfrak{b}_2^2(\vec{k}) - \mu_3 + i\epsilon \right)}. \end{aligned} \quad (3.6)$$

³This is evident due to the resulting energy-momentum relation (3.4).

Here Feynman boundary conditions are used and the gamma matrices $\gamma^i = \sigma_3 \sigma_i$ and $\gamma^0 = \sigma_3$ are given by the usual Pauli-matrices σ_i (see Appendix B).

Now we are assuming that the same ansatz is valid for the dressed propagator⁴ (analogically to the dressed fermion propagator discussed in section 2.4) with dressing functions $\mathcal{B}_i(\vec{k})$ ($i \in \{1, 2\}$), $\mathcal{M}(\vec{k})$ and $\mathcal{Z}(\vec{k})$ which eventually follows from renormalization theory and was worked out in Ref. [25]. The dressing functions $\mathcal{B}_i(\vec{k})$ equates to the renormalization of the Fermi velocity [15] and $\mathcal{M}(\vec{k})$ is the corresponding mass renormalization. So the general form for the propagator can be obtained

$$G_F^{-1}(k_0, \vec{k}) = -i(\mathcal{Z}(k_0 + \mu)\gamma^0 - \mathcal{B}_1(\vec{k})\gamma^1 - \mathcal{B}_2(\vec{k})\gamma^2 - \mathcal{M}(\vec{k})), \quad (3.7)$$

where γ^i are the Dirac matrices in Pauli representation σ^i

$$\gamma^0 = \sigma_3, \quad \gamma^i = \sigma_3 \sigma_i \quad \text{with} \quad i \in \{1, 2\},$$

that are introducing the Clifford algebra $\{\gamma_\mu, \gamma_\nu\} = 2g_{\mu\nu}$ for the two dimensional sublattice space (see Appendix B). The general propagator is given by (see Eq. (2.27))

$$G_F^{-1}(k_0, \vec{k}) = G_F^{(0)-1}(k_0, \vec{k}) + e^2 \int_{\mathcal{BZ}} \frac{dq^2}{(2\pi)^2} \int \frac{dq^0}{2\pi} D_C(k_0 - q_0, \vec{k} - \vec{q}) \gamma^0 G_F(q_0, \vec{q}) \Gamma^0(q, k). \quad (3.8)$$

So the fermion propagator in this approach yields

$$\begin{aligned} G_F^{-1} = & -i((k_0 + \mu)\gamma^0 - \mathfrak{b}_1(\vec{k})\gamma^1 - \mathfrak{b}_2(\vec{k})\gamma^2 - \mu_3) + e^2 \int_{\mathcal{BZ}} \frac{d^3 q}{(2\pi)^3} D_C(\vec{k} - \vec{q}) \gamma^0 \\ & \times \frac{i\mathcal{Z}(\gamma^0(q_0 + \mu) - \mathcal{B}_1(\vec{q})\gamma^1 - \mathcal{B}_2(\vec{q})\gamma^2 + \mathcal{M}(\vec{q}))}{\mathcal{Z}^2(q_0 + \mu)^2 - \mathcal{B}_1^2(\vec{q}) - \mathcal{B}_2^2(\vec{q}) - \mathcal{M}^2(\vec{q})^2} \gamma^0, \end{aligned} \quad (3.9)$$

here the photon propagator is already identified as a frequency independent quantity. This ansatz follows from a static approximation and is discussed in the next chapter. Also the full vertex is approximated by the bare one $\Gamma^0 = \gamma^0$, what follows from Ward-Takahashi identity [26] and remains justified since the wave function renormalization equals to one [15]. This in turn follows from a frequency independent photon propagator, so this is the only approximation which has been made here.

The dressing functions now can be derived by the projection onto the different gamma matrices

$$\mathcal{M}(\vec{k}) = \frac{1}{2i} \text{tr}(G_F^{-1}(k_0, \vec{k})) \quad (3.10)$$

$$\mathcal{B}_i(\vec{k}) = -\frac{1}{2i} \text{tr}(G_F^{-1}(k_0, \vec{k}) \gamma^i) \quad (3.11)$$

$$\mathcal{Z}(\vec{k}) = -\frac{1}{2i} \text{tr}(G_F^{-1}(k_0, \vec{k}) \gamma^i) \quad (3.12)$$

where both the Fermi-velocity renormalization and the mass renormalization function become frequency independent and the wave function renormalization is one ($\mathcal{Z} = 1$) due to the fre-

⁴This is the most general ansatz (without any symmetry assumptions) which is clear due to the expansion in gamma matrices.

quency independent photon propagator [7].

We finally get the following expressions for the dressing functions

$$\mathcal{M}(\vec{k}) = \mu_3 + e^2 \int_{\mathcal{BZ}} \frac{d^3 q}{(2\pi)^3} D_C(\vec{k} - \vec{q}) \frac{\mathcal{M}(\vec{q})}{(q_0 + \mu)^2 - \mathcal{B}_1^2(\vec{q}) - \mathcal{B}_2^2(\vec{q}) - \mathcal{M}^2(\vec{q})}, \quad (3.13)$$

$$\mathcal{B}_i(\vec{k}) = \mathfrak{b}_i(\vec{k}) + e^2 \int_{\mathcal{BZ}} \frac{d^3 q}{(2\pi)^3} D_C(\vec{k} - \vec{q}) \frac{\mathcal{B}_i(\vec{q})}{(q_0 + \mu)^2 - \mathcal{B}_1^2(\vec{q}) - \mathcal{B}_2^2(\vec{q}) - \mathcal{M}^2(\vec{q})}. \quad (3.14)$$

The integral over the q_0 component

$$I(\vec{q}) = \int_{-\infty}^{\infty} \frac{dq_0}{2\pi} \frac{i}{(q_0 + \mu)^2 - \Omega^2(\vec{q})} \quad (3.15)$$

with $\Omega^2(\vec{q}) = \mathcal{B}_1^2(\vec{q}) + \mathcal{B}_2^2(\vec{q}) + \mathcal{M}^2(\vec{q})$ can be calculated analytically either by a Wick rotation or by evaluating the integral with the residue theorem (here a Wick rotation is used).

In the following only the case $\mu = 0$ should be considered, which equates to an investigation at zero temperature. Initially one has to perform a Wick rotation to Euclidean space $q_0 \rightarrow i\omega$

$$I(\vec{q}) = \int_{-\infty}^{\infty} \frac{d\omega}{2\pi} \frac{1}{\omega^2 + \Omega^2(\vec{q})} \quad (3.16)$$

and simply evaluate the remaining integral. So one finds

$$I(\vec{q}) = \frac{1}{2\pi\Omega(\vec{q})} \arctan \left(\frac{\omega}{\Omega(\vec{q})} \right) \Big|_{-\infty}^{\infty} = \frac{1}{2\Omega(\vec{q})}, \quad (3.17)$$

and end up with the following equations for the dressing functions for a general consideration at zero temperature ($\mu = 0$)

$$\mathcal{M}(\vec{k}) = \mu_3 + e^2 \int_{\mathcal{BZ}} \frac{d^2 q}{(2\pi)^2} (-iD_C(\vec{k} - \vec{q})) \frac{\mathcal{M}(\vec{q})}{2\Omega(\vec{q})}, \quad (3.18)$$

$$\mathcal{B}_i(\vec{k}) = \mathfrak{b}_i(\vec{k}) + e^2 \int_{\mathcal{BZ}} \frac{d^2 q}{(2\pi)^2} (-iD_C(\vec{k} - \vec{q})) \frac{\mathcal{B}_i(\vec{q})}{2\Omega(\vec{q})}. \quad (3.19)$$

Alternatively, the DSE's for \mathcal{B}_1 and \mathcal{B}_2 can be combined to one Dyson-Schwinger equation for the structure function

$$\Phi(\vec{k}) = \phi(\vec{k}) + e^2 \int_{\mathcal{BZ}} \frac{d^2 q}{(2\pi)^2} (-iD_C(\vec{k} - \vec{q})) \frac{\Phi(\vec{q})}{2\Omega(\vec{q})}, \quad (3.20)$$

which might be closer to the physical interpretation.

4. Photon Propagator

4.1. Instantaneous Coulomb Interactions

Now, the interaction between the quasiparticles should be introduced by an instantaneous approximation which is suitable as long as the Fermi velocity is much smaller than the speed of light ($v_f/c \ll 1$). The magnetic interaction is neglected, because it is suppressed with the first order of v_f , so the Lagrange density including the interaction with a charged source j_μ

$$\mathcal{L} = -\frac{1}{4}F_{\mu\nu}F^{\mu\nu} - \frac{1}{2}\zeta(\partial_\sigma A^\sigma)^2 - j_\mu A^\mu, \quad (4.1)$$

reduces to

$$\mathcal{L} = -\rho(t, \vec{r})A^0(t, \vec{r}) + \frac{1}{2}[\nabla A^0(t, \vec{r})]^2 - \frac{1}{2}[\partial_0 A^0(t, \vec{r})]^2 \quad (4.2)$$

in Feynman-gauge ($\zeta = 1$) [15]. The charge distribution has to be restricted to the two dimensional graphene sheet (here identified by the xy-plane)

$$\rho(t, \vec{r}) = e \bar{\psi}(t, \vec{r})\gamma^0\psi(t, \vec{r})\delta(z). \quad (4.3)$$

The bare photon propagator in (3+1) dimensions is consequently given by [15]

$$D_{tl}^{00}(t, \vec{r}, z=0) = \int \frac{d\omega}{2\pi} \frac{d^2p}{(2\pi)^2} \frac{dp_z}{2\pi} \frac{-i}{\omega^2 - \vec{p}^2 - p_z^2 + i\epsilon} e^{-i\omega t} e^{i\vec{p}\vec{r}}, \quad (4.4)$$

and has to be restricted to the graphene plane as well.

By integrating over the p_z variable (with similar techniques as in section 3.2), the bare photon propagator in the instantaneous approximation yields

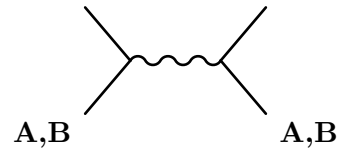
$$D_{Coul}^{(0)}(\vec{p}) = \frac{i}{2|\vec{p}|}, \quad (4.5)$$

which is also accessible by the photon propagator given by (Eq. 2.28) for a pure electric field ($\mu = \nu = 0$) at tree level (neglecting the vacuum polarization $\Pi(p^2) = 0$).

This photon propagator can now be used to solve the Dyson-Schwinger equations ((3.18) and (3.20)) and equates to a simple Coulomb-potential in position space.

4.1.1. Diagrammatic Representation

So in this first approach the photon propagator was approximated by the tree level propagator without vacuum polarization. That means screening effects were neglected for the moment. The common Feynman diagram for the Coulomb interaction is depicted on the right hand side.



Assuming a Coulomb interaction between the electrons of the sublattices A and B, one can

deduce the following composition of the fermion propagator (without vacuum polarization).

$$\text{A,B} \text{---} \text{---} \text{A,B} + \text{A,B} \text{---} \text{---} \text{A,B}$$

Here the second diagram represents the case of no momentum transfer that would principally diverge. But this diagram exactly cancels with the background interaction in the case of $\mu = 0$ as it is shown in Ref. [27] in detail. So, this contribution can be completely neglected. The remaining diagram can be elaborated in 4 different diagrams.

$$\begin{aligned} & \text{A} \text{---} \text{---} \text{A} + \text{A} \text{---} \text{---} \text{B} \\ & \quad \quad \quad \text{G}_{AA}^{-1} \quad \quad \quad \text{G}_{AB}^{-1} \\ & + \text{B} \text{---} \text{---} \text{A} + \text{B} \text{---} \text{---} \text{B} \\ & \quad \quad \quad \text{G}_{BA}^{-1} \quad \quad \quad \text{G}_{BB}^{-1} \end{aligned} \quad (4.6)$$

These diagrams strictly determine which interaction is important for the single dressing function and how the interaction has to be included in the appropriate Dyson-Schwinger equation. The interaction between two similar sites has to be propagated by a fermion propagator connecting an A site with an A site or a B site with a B site and analogical for the interaction of two sites from different sublattices.

Because of the structure of the fermion propagator in sublattice space (see Eq. (3.7))

$$G_F^{-1} = \begin{pmatrix} G_{AA}^{-1} & G_{AB}^{-1} \\ G_{BA}^{-1} & G_{BB}^{-1} \end{pmatrix} = i \begin{pmatrix} \mathcal{M} - (k_0 + \mu) & \mathcal{B}_1 - i\mathcal{B}_2 \\ -\mathcal{B}_1 - i\mathcal{B}_2 & \mathcal{M} + (k_0 + \mu) \end{pmatrix} \quad (4.7)$$

one would expect that the mass renormalization function only depends on the interaction between two similar sites and the Fermi-velocity renormalization should only depend on an interaction between sites from different sublattices.

4.2. Transforming the Potential into Position Space

Especially in the course of providing a more realistic potential it would be desirable to be able to start the procedure from a potential given in position space. Also for the calculations using the Fast Fourier Transform (FFT) method to solve the Dyson-Schwinger equations it would save computation time, which is discussed in section 5.4.

The simple $1/r$ -potential that eventually should provide the Photon propagator (see Eq. (4.5))

$$V(\vec{k}) = \frac{1}{|\vec{k}|} \quad (4.8)$$

can be easily transformed into position space with the help of a common Fourier transform (see Appendix D)

$$\tilde{V}(\vec{r}) = \int_{\mathbb{R}^2} \frac{d^2k}{(2\pi)^2} \frac{1}{|\vec{k}|} e^{i\vec{k}\vec{r}} = \frac{1}{2\pi} \frac{1}{|\vec{r}|} \quad (4.9)$$

if it could be calculated in the continuum. This simply provides a $1/r$ -potential in position space. On the discrete lattice things are more complicated, but in a first approach the discrete Fourier transform can be used as stated out in Appendix D. This discretization is based on the discrete lattice in position space which is given by

$$\vec{r}_{ij} = i\vec{a}_1 + j\vec{a}_2 \quad (4.10)$$

with integer values for i and j

$$i, j \in \{0, \dots, N-1\}. \quad (4.11)$$

$$(4.12)$$

Consequently the corresponding reciprocal basis is determined by the reciprocal basis vectors \vec{b}_1 and \vec{b}_2 that are divided in N parts. So the momentum vector is limited to the certain points

$$\vec{k}_{mn} = \frac{n}{N}\vec{b}_1 + \frac{m}{N}\vec{b}_2 \quad (4.13)$$

with integer values for m and n

$$m, n \in \{0, \dots, N-1\}. \quad (4.14)$$

$$(4.15)$$

So, this leads to

$$\tilde{V}(r_{ij}) = \frac{\mathcal{BZ}}{N^2(2\pi)^2} \sum_{mn} \frac{1}{|\vec{k}_{mn}|} e^{\frac{2\pi i}{N}(im+jn)} \quad (4.16)$$

or better

$$\tilde{V}(r_{ij}) = \frac{\text{const.}}{a^2 N^2 (2\pi)^2} \sum_{mn} V(k_{mn}) e^{\frac{2\pi i}{N}(im+jn)} \quad (4.17)$$

with a being the interatomic distance of two carbon atoms (a is also contained in $V(k_{mn})$). Now the question is when this expression becomes similar to that of equation (4.9). At first we have to consider $N \rightarrow \infty$ for a more precise discretization of the Brioullin zone that turns into a continuous representation in momentum space. $N \rightarrow \infty$ means an infinite number of unit cells in position space, but additionally it has to be required that the lattice point distance in position space approaches zero ($a \rightarrow 0$). Then even the momentum space area reaches infinity and the above expressions become equal [26]; in terms of approaching the continuum limit.

In our case a is a real constant determined by the real honeycomb lattice of our graphene sheet, so we have to treat the approximation of our potential as a simple $1/r$ -potential in position space quite carefully.

There is no reason to expect the same renormalization functions for the different approaches

but they should deliver the same critical coupling constants since the wavelength λ approaches infinity for zero momentum and therefore the continuums description becomes valid for

$$\lambda \gg a.$$

So in any case we expect the same critical coupling since it represents a fixpoint of the theory, either basing our calculations on an ansatz in position space or an ansatz in momentum space. There is one additional point that has to be taken into account and which crucially affects the calculations, the term $V(\vec{p}=0)$ has simply been approximated by the value of the neighbouring points for every lattice size. This point is a null set and does not decisively contribute to the integral of the Dyson-Schwinger equation, so this approximation is justified. But the on-site term in position space causes a shift in momentum space and influences the value of the integral dominantly.

$$V(k_{mn}) = \mathcal{AZ} \sum_{ij} \tilde{V}(r_{ij}) e^{-\frac{2\pi i}{N}(im+jn)} = \mathcal{AZ} \left(\tilde{V}(0) + \sum_{ij \setminus \{0,0\}} \tilde{V}(r_{ij}) e^{-\frac{2\pi i}{N}(im+jn)} \right) \quad (4.18)$$

This dominance makes sense from a physical point of view since $\tilde{V}(0)$ has the meaning of the on-site repulsion in position space. So, as long as we do not use a realistic potential where the on-site term should definitely come from more physical considerations its value is set to

$$\tilde{V}(0) = \frac{\mathcal{BZ}}{N^2(2\pi)^2} \sum_{mn} V(k_{mn}) \quad (4.19)$$

especially in order to recompute the analytical value of the critical coupling, starting with a potential in position space.

4.3. Periodic Potential

To get a continuous potential that takes the lattice symmetries into account, a periodic potential which respects the translational invariance of the lattice has to be used. In the case of an instantaneous Coulomb interaction one principally has to think about constructing a periodic $1/p$ -potential on the BZ.

At first, this potential should be investigated on the BZ given by the honeycomb

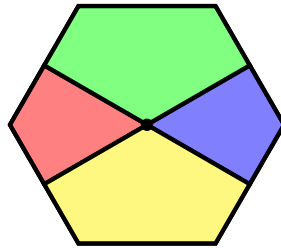


Figure 5: The first BZ is shown. The colored areas show the equivalent parts of the second BZ.

Here the situation seems to be clear. The potential can be simply constructed by evaluating the distance to the center of the BZ. That can be continued for each further Brioullin zone, from which one gets a potential in momentum space with the desired properties, automatically fulfilling Born-von-Karman boundary conditions [17] that can be mathematically expressed by

$$V(\vec{p}) = V(\vec{p} + n_1 \vec{b}_1 + n_2 \vec{b}_2), \quad (4.20)$$

here \vec{b}_1 and \vec{b}_2 are the basis vectors of the Brillouin zone and $\{n_1, n_2\} \in \mathbb{Z}$.

The advantage by considering the honeycomb, is that only the shortest distance to a lattice point is taken into account. The first BZ is graphically constructed by drawing the perpendicular bisectors of each connecting line between the lattice point and its neighbours. So by construction the honeycomb only contains points that are closer to its center than to any other lattice point. That is exactly the behaviour that is required for the potential. In this way a completely symmetric potential is gained.

Unfortunately, the calculation should be based on the reduced Brioullin zone in order to have a simple approach to evaluate the integral in momentum space. So the potential has to be formulated in terms of a rhombic BZ.

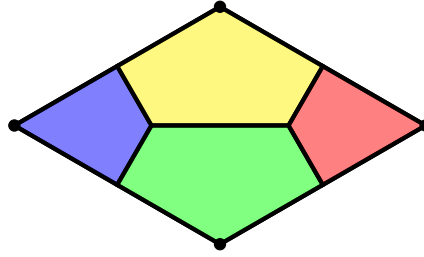


Figure 6: The reduced second Brioullin zone is shown, with the help of the colored areas the deduction from the first Brioullin zone can be simply understood.

As it is indicated in Fig. 5 and Fig. 6 with the help of the colored areas the potential on the rhombic BZ can be constructed from that on the honeycomb lattice. This can be realized by searching the shortest path from a point of the BZ to the lattice point on a twisted torus, representing periodic boundary conditions. The torus in this case is twisted because of the rhombic form of the BZ. This exactly equates to use the shortest path to one of the corners of the Brioullin zone, so we end up with the following potential

$$V(\vec{k}) = V(\vec{k}_{min}) \quad (4.21)$$

with

$$\vec{k}_{min} = \min(k_{m,n}, k_{m-N,n}, k_{m,n-N}, k_{m-N,n-N}). \quad (4.22)$$

The obtained potential is qualitatively illustrated in Fig. 7 for a lattice size of $N = 900$, of course the corner regions are dominant.

To get a better insight of the structure of the potential, the z-range has been cutted and a contour plot was made (see Fig. 8). Here the numerical realization of the required symmetries can be nicely observed. This translational invariance provides a consistent result even for shifted Brioullin zones and takes the lattice symmetry into account.

The same techniques can be applied in position space were a general vector is given by

$$\vec{r} = r_{i,j} = i\vec{a}_1 + j\vec{a}_2,$$

so the periodic structure can be analogically obtained by taking the shortest path on the torus. This is realized by

$$V(\vec{r}) = V(\vec{r}_{min}), \quad (4.23)$$

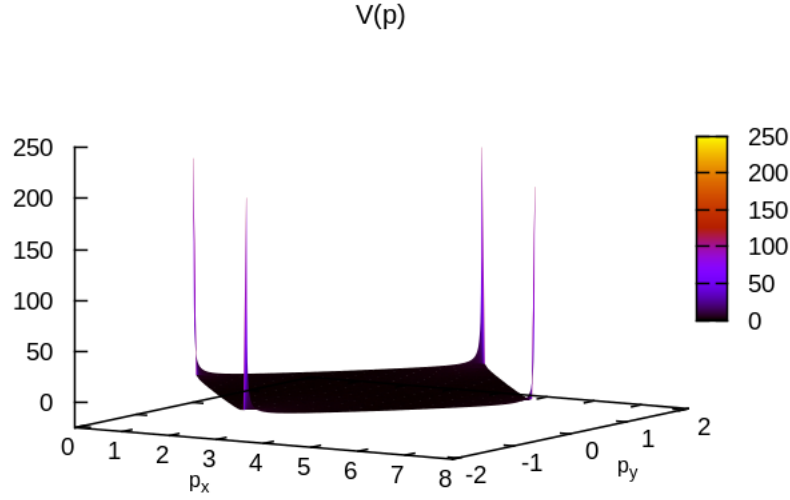


Figure 7: The periodic potential in momentum space is represented on the rhombic BZ. Obviously the corners, where a bare Coulomb potential would diverge still dominate the potential.

with

$$\vec{r}_{min} = \min(r_{i,j}, r_{i-N,j}, r_{i,j-N}, r_{i-N,j-N}), \quad (4.24)$$

in this way we can also obtain a periodic and symmetric potential in position space.

Thereby especially a potential that provides exactly the same results for the DSE's, independent of the position of the origin, can be obtained. For example one can similarly construct a BZ with the Γ -point (see Fig. 4) being the center of the BZ instead of the M-point, for such a BZ we now get exactly the same solution as for the choice of our BZ.

If we are assuming a periodic potential in position space and doing a Fourier transform into momentum space we obtain a potential exhibiting the same properties. This potential is again represented qualitatively ($N = 900$) in Fig. 9 where we can observe the required behaviour. Due to the finite discretization (see section 4.2) one would not expect exactly the same potential.

The potential in momentum space that is calculated from a Fourier transform of the appropriate potential in position space has to be always real-valued. This is because the Fourier transform of a real-valued function that is even on the considered symmetry cell is also real-valued and even [28].

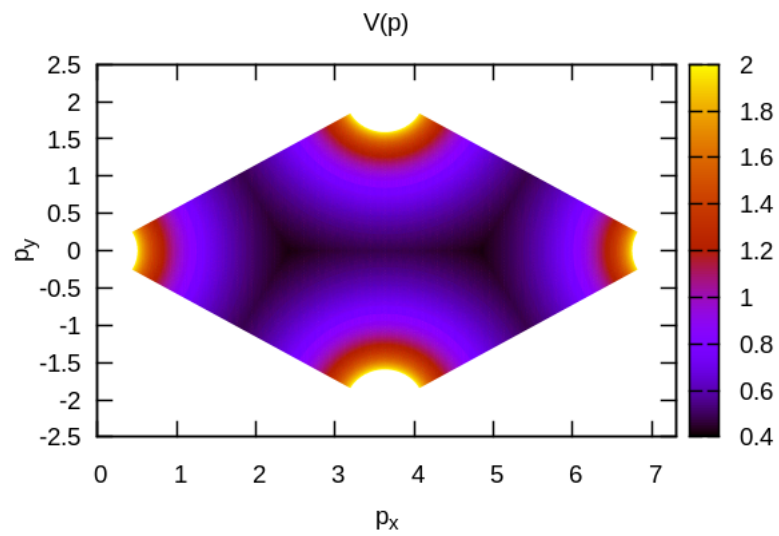


Figure 8: A contour plot of the periodic potential on the Brioullin zone is shown. The required periodicity can be observed.

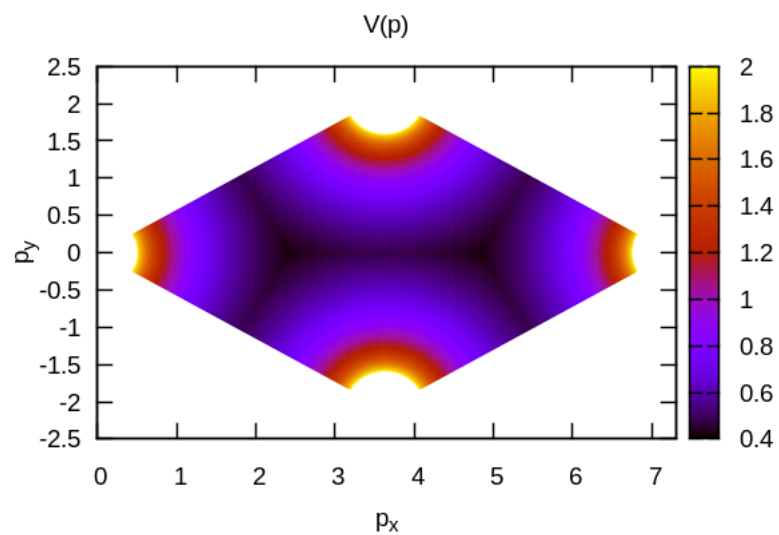


Figure 9: A contour plot of the periodic potential obtained from a Fourier transform of the potential in position space on the Brioullin zone is shown. The required periodicity can be observed.

5. Numerical Methods

5.1. Discretization of the Brioullin Zone

Based on the resulting integrals of section 3.2 with the periodic potential V from the last section, the DSE's read

$$\mathcal{M}(\vec{k}) = \mu_3 + \frac{e^2}{4} \int_{\mathcal{BZ}} \frac{d^2q}{(2\pi)^2} V(\vec{k} - \vec{q}) \frac{\mathcal{M}(\vec{q})}{\sqrt{|\Phi(\vec{q})|^2 + \mathcal{M}^2(\vec{q})}}, \quad (5.1)$$

$$\Phi(\vec{k}) = \phi(\vec{k}) + \frac{e^2}{4} \int_{\mathcal{BZ}} \frac{d^2q}{(2\pi)^2} V(\vec{k} - \vec{q}) \frac{\Phi(\vec{q})}{\sqrt{|\Phi(\vec{q})|^2 + \mathcal{M}^2(\vec{q})}}. \quad (5.2)$$

Now the momentum integral should be evaluated by discretizing the BZ.

The integral over the BZ (pink rhomboid depicted in Fig. 2) can then be transformed into the sum

$$\int_{\mathcal{BZ}} \frac{d^2q}{(2\pi)^2} \longrightarrow \sum_{m,n} \frac{(\Delta k)^2}{(2\pi)^2} \quad (5.3)$$

where $(\Delta k)^2$ is the area of the smallest momentum unit on the lattice given by

$$(\Delta k)^2 = \left| \frac{\vec{b}_1}{N} \times \frac{\vec{b}_2}{N} \right| = \frac{\mathcal{BZ}}{N^2}. \quad (5.4)$$

The expressions from Eq. (5.3) becomes equal in the continuums limit as explained in the last section 4.3. So, Eq. (5.1) and Eq. (5.2) yield

$$M_{mn} = \mu_3 + \frac{e^2}{4} \sum_{i,j} \frac{(\Delta k)^2}{(2\pi)^2} V(k_{mn} - q_{ij}) \frac{M_{ij}}{\sqrt{|\Phi_{ij}|^2 + M_{ij}^2}}, \quad (5.5)$$

$$\Phi_{mn} = \phi_{mn} + \frac{e^2}{4} \sum_{i,j} \frac{(\Delta k)^2}{(2\pi)^2} V(k_{mn} - q_{ij}) \frac{\Phi_{ij}}{\sqrt{|\Phi_{ij}|^2 + M_{ij}^2}}, \quad (5.6)$$

in the discretized momentum space (see Eq. (4.13)), with the corresponding discretized dressing functions Φ_{ij} and M_{ij} .

The coupling constant α is given by $\alpha = e^2/(4\pi\epsilon v_f)$ [5], the Fermi-velocity follows from section 2.2: $v_f = \frac{3}{2}a\kappa$. That yields the following equations

$$M_{mn} = \mu_3 + \frac{3a}{8\pi} \frac{\mathcal{BZ}}{N^2} \alpha \kappa \sum_{i,j} V(k_{mn} - q_{ij}) \frac{M_{ij}}{\sqrt{|\Phi_{ij}|^2 + M_{ij}^2}}, \quad (5.7)$$

$$\Phi_{mn} = \phi_{mn} + \frac{3a}{8\pi} \frac{\mathcal{BZ}}{N^2} \alpha \kappa \sum_{i,j} V(k_{mn} - q_{ij}) \frac{\Phi_{ij}}{\sqrt{|\Phi_{ij}|^2 + M_{ij}^2}}. \quad (5.8)$$

For suspended graphene $\epsilon = 1$ is assumed. With the dimensionless potential

$$\mathcal{V}_{ijmn} = \mathcal{V}(k_{mn} - q_{ij}) = V(k_{mn} - q_{ij})/a \quad (5.9)$$

a basis independent expression for the Dyson-Schwinger equations can be found in units of the hopping parameter κ

$$M_{mn}/\kappa = \mu_3/\kappa + \frac{3a^2}{8\pi} \frac{\mathcal{B}\mathcal{Z}}{N^2} \alpha \sum_{ij} \mathcal{V}_{ijmn} \frac{M_{ij}/\kappa}{\sqrt{(|\Phi_{ij}|/\kappa)^2 + (M_{ij}/\kappa)^2}}, \quad (5.10)$$

$$\Phi_{mn}/\kappa = \phi_{mn}/\kappa + \underbrace{\frac{3a^2}{8\pi} \frac{\mathcal{B}\mathcal{Z}}{N^2}}_{=:c} \alpha \sum_{ij} \mathcal{V}_{ijmn} \frac{\Phi_{ij}/\kappa}{\sqrt{(|\Phi_{ij}|/\kappa)^2 + (M_{ij}/\kappa)^2}}. \quad (5.11)$$

In the following the declaration of κ is suppressed, but all renormalization functions are indicated in units of κ , furthermore the dimensionless constant c is introduced

$$M_{mn} = \mu_3 + c \alpha \sum_{ij} \mathcal{V}_{ijmn} \frac{M_{ij}}{\sqrt{|\Phi_{ij}|^2 + M_{ij}^2}}, \quad (5.12)$$

$$\Phi_{mn} = \phi_{mn} + c \alpha \sum_{ij} \mathcal{V}_{ijmn} \frac{\Phi_{ij}}{\sqrt{|\Phi_{ij}|^2 + M_{ij}^2}}. \quad (5.13)$$

These structurally similar equations can still be summarized within a vector notation by again using the different parts of the structure function \mathcal{B}_1 and \mathcal{B}_2 (see Eq. (3.19)) and \mathcal{M} . So with the vectors

$$\mathcal{G} = \{\mathcal{M}, \mathcal{B}_1, \mathcal{B}_2\} \quad \text{and} \quad \mathbf{g} = \{\mu_0, \mathbf{b}_1, \mathbf{b}_2\}, \quad (5.14)$$

equation 5.15 is obtained.

$$\mathcal{G}_{mn} = \mathbf{g}_{mn} + c \alpha \sum_{ij} \mathcal{V}_{ijmn} \frac{\mathcal{G}_{ij}}{|\mathcal{G}_{ij}|}. \quad (5.15)$$

With this notation it is easier to understand what happens in the next sections.

5.2. Iteration Method

One method to solve the coupled set of equations (5.15) is to iterate the values of the components of \mathcal{B}_{mn} as long as the changes of these values are small enough to assume that the iteration has converged. Here the initial values of the matrix M_{ij} were set to 1 and the initial values of the structure function were set to their bare values $\Phi_{ij} = \phi_{ij}$ at the beginning of the iteration.

In the presented calculations the maximum relative deviation that was tolerated was of the order of 10^{-8} . So the applied criterion to stop the iteration and accept the iteration as converged can be expressed as follows:

$$\max \left\| \frac{\mathcal{G}_{mn} - \mathcal{G}_{mn}^{new}}{\mathcal{G}_{mn}} \right\| \leq 10^{-8}, \quad (5.16)$$

here \mathcal{G}_{mn}^{new} is the value of \mathcal{G}_{mn} obtained by the next iteration step. So in each iteration step the whole vector \mathcal{G}_{mn} is updated. The maximum has to be evaluated in terms of every momentum index and every component of the vector \mathcal{G} .

The discrepancy to zero (Eq. 5.16) is unfortunately not directly related to the deviation from the exact solution of \mathcal{G} . Especially in the regime near the critical coupling where the correlation length is large, the contribution in every iteration step is small but may still drift away continuously. So due to the phenomenon of critical slowing down an enormous increase of necessary iteration steps in the area around the critical coupling is observed.

How a more reliable estimate of the error for \mathcal{G}_{mn} can be obtained is pointed out in the next section, but it is not included in the calculations yet.

5.3. Quasi-Newton Method

Another possibility to solve Eq. (5.15) is to apply a Quasi-Newton method which reduces to the ordinary Newton method in one dimension.

Describing Eq. (5.15) in units of κ with consecutive indices yields

$$\mathcal{G}_i = \mathbf{g}_i + c \alpha \sum_k \mathcal{V}_{ki} \frac{\mathcal{G}_k}{|\mathcal{G}_k|}, \quad (5.17)$$

where i and $k \in \{0, \dots, N^2 - 1\}$.

This expression can be converted into a multidimensional equation that depends on the set of variables \mathcal{G}_k

$$F_i(\mathcal{G}_0, \mathcal{G}_1, \dots, \mathcal{G}_{N^2-1}) = (\mathbf{g}_i - \mathcal{G}_i) + c \alpha \sum_k \mathcal{V}_{ki} \frac{\mathcal{G}_k}{|\mathcal{G}_k|} = 0 \quad (5.18)$$

for every component of \mathcal{G} .

This equation can now obviously be solved by a root-finding method, e.g. the Newton-Raphson method [28].

Expanding a multidimensional function into an ordinary Taylor series yields

$$F_i(x + \Delta x) = F_i(x) + \sum_{j=0}^{N^2} \frac{\partial F_i}{\partial x_j} \Delta x_j + \mathcal{O}(\Delta x^2), \quad (5.19)$$

which is equal to

$$F(x + \Delta x) = F(x) + \mathcal{J} \Delta x + \mathcal{O}(\Delta x^2) \quad (5.20)$$

in matrix notation with the Jacobian matrix \mathcal{J} . By neglecting terms of higher order ($\mathcal{O}(\Delta x^2)$) and setting $F(x + \Delta x) = 0$ which corresponds to the root finding of the tangent in the standard Newton method, one obtains a linear equation system

$$\mathcal{J} \Delta x = -F, \quad (5.21)$$

that has to be solved for Δx and x has to be updated in every iteration step

$$x_{new} = x_{old} + \Delta x. \quad (5.22)$$

In order to solve Eq. (5.18) where x equates to the vector \mathcal{G}_i and \mathcal{G} represents either \mathbf{M} or Φ , one has to identify the Jacobian matrix that can be calculated analytically

$$\mathcal{J}_{ij} = -\delta_{ij} + c \alpha \frac{\mathcal{V}_{ji}}{|\mathcal{G}_j|} \left(1 + \frac{\mathcal{G}_j^2}{|\mathcal{G}_j|^2} \right). \quad (5.23)$$

To solve Eq. (5.21) an LU-decomposition is used, the algorithm works for a small number of lattice points. In the Newton method the necessary number of iterations seems to be reduced in comparison to the direct iteration method. That gives rise to the assumption that this method might be worthwhile near the critical coupling, where critical slowing down is dominant, if a more effective way of solving Eq. (5.21) is found. Until now the LU-decomposition in such high dimensions is too extensive. But the method seems to be promising since the point is reached where the number of iterations surmounts the effort of solving Eq. (5.21).

Moreover the deviations from zero in Eq. (5.16) equate to the percentage value of F , hence

Eq. (5.21) has to be solved likewise to get an error measurement even for the iteration method. So, having an effective method to solve this equation system seems to be desirable anyway for future calculations.

5.4. Convolution Method

A much more effective way of solving equations (5.12) and (5.13) is to exploit the fact that the Dyson-Schwinger equations have the form of a convolution from a mathematical point of view. A general convolution is given by

$$(f * g)(\vec{x}) = \int d\vec{y} f(\vec{y}) g(\vec{x} - \vec{y}). \quad (5.24)$$

Considering the continuous representation of Dyson-Schwinger equations again ((5.1) and (5.2))

$$M(\vec{k}) = \mu_3 + \frac{e^2}{4} \alpha \int d^2 q V(\vec{k} - \vec{q}) \frac{M(\vec{q})}{\sqrt{|\Phi(\vec{q})|^2 + M^2(\vec{q})}}, \quad (5.25)$$

$$\Phi(\vec{k}) = \phi(\vec{k}) + \frac{e^2}{4} \alpha \int d^2 q V(\vec{k} - \vec{q}) \frac{\Phi(\vec{q})}{\sqrt{|\Phi(\vec{q})|^2 + M^2(\vec{q})}}, \quad (5.26)$$

we immediately find that the Dyson-Schwinger equations are consisting of a convolution (compare to (5.24)). To solve the Dyson-Schwinger equations, the integral

$$\int V(\vec{k} - \vec{q}) \chi(\vec{q}) d\vec{q} \quad (5.27)$$

has to be evaluated. Here $\chi(\vec{q})$ depends on either considering the DSE for the mass renormalization function or the Fermi-velocity renormalization.

By considering the convolution theorem (specified in Appendix D) in two dimensions

$$\mathcal{F}(f * g) = (2\pi)^2 \mathcal{F}(f) \mathcal{F}(g) \quad (5.28)$$

and especially the equivalent inverse

$$\mathcal{F}(f) * \mathcal{F}(g) = (2\pi)^2 \mathcal{F}(f \cdot g), \quad (5.29)$$

one finds

$$\int V(\vec{k} - \vec{q}) \cdot \chi(\vec{q}) d\vec{q} = (2\pi)^2 \mathcal{F}[\tilde{V}(\vec{x}) \cdot \tilde{\chi}(\vec{x})], \quad (5.30)$$

where \mathcal{F} represents the Fourier transform and $\tilde{V}(\vec{x})$ and $\tilde{\chi}(\vec{x})$ are the corresponding Fourier transformed functions in position space. So the Dyson-Schwinger equations are given by

$$\mathcal{M}(\vec{k}) = \mu_3 + e^2 \pi^2 \mathcal{F}[\tilde{V}(\vec{x}) \cdot \tilde{\chi}_M(\vec{x})], \quad (5.31)$$

$$\Phi(\vec{k}) = \phi(\vec{k}) + e^2 \pi^2 \mathcal{F}[\tilde{V}(\vec{x}) \cdot \tilde{\chi}_\Phi(\vec{x})], \quad (5.32)$$

and the two dimensional integral (5.27) can also be evaluated by performing three independent Fast Fourier Transformations (two in the case of a given potential in position space) which provide an enormous numerical advantage. The detailed calculation to obtain equations (5.31) and (5.32) can be found in Appendix D. Now the origin of this effective numerical method should

be investigated.

Considering a Discrete Fourier Transform (DFT) of N sampling points in one dimension as example

$$\mathcal{F}_k = \sum_{j=0}^{N-1} e^{\frac{2\pi i}{N}jk} f_j = \mathcal{A}_{jk} f_j k, \quad (5.33)$$

one can easily come to the conclusion that N^2 complex multiplication steps are necessary to execute the sum. Hence the required effort to solve the Dyson-Schwinger equations from the last section would be of the same order than solving the DSE's by simply executing the sum of Eq. (5.12) or Eq. (5.13).

During the 1960s a far better method has been established by Cooley and Turkey [29]. It has been shown that the usual DFT of the order of N^2 can be effectively reduced to a numerical algorithm which only requires $\mathcal{O}(N \log_2(N))$ operations. This algorithm calling the Fast Fourier Transform (FFT) means an immense advantage regarding the computation time of solving the DSE's.

The basic idea can easily be understood by an examination of the composition of a usual Fourier transform of discretely sampled data of the length N into two discrete Fourier transforms of the length $N/2$. This composition is based on the separation of even and odd summands:

$$\mathcal{F}_k = \sum_{j=0}^{N/2-1} e^{\frac{2\pi i}{N}2jk} f_{2j} + \sum_{j=0}^{N/2-1} e^{\frac{2\pi i}{N}(2j+1)k} f_{2j+1} \quad (5.34)$$

$$= \sum_{j=0}^{N/2-1} e^{\frac{2\pi i}{(N/2)}jk} f_{2j} + w^k \sum_{j=0}^{N/2-1} e^{\frac{2\pi i}{(N/2)}jk} f_{2j+1} \quad (5.35)$$

$$= \mathcal{F}_k^{\text{even}} + w^k \mathcal{F}_k^{\text{odd}}, \quad (5.36)$$

with $w = e^{\frac{2\pi i}{N}}$.

Obviously, the conversion of one DFT of the order of N to two DFT's of the half length requires $N/2$ complex multiplications [29]. Assuming that the number of sampling points can be expressed in powers of 2

$$N = 2^\gamma \quad \gamma = \log_2(N), \quad (5.37)$$

an arbitrary Fourier Transform can be decomposed in N first order Fourier transforms in γ splitting steps. In every step we need $N/2$ complex multiplications, so consequently we get an algorithm of the order of $N/2 \log_2(N) \sim N \log_2(N)$. The process can be illustrated by the following reduction chain

$$\mathcal{F}[N] \rightarrow 2 \mathcal{F}[N/2] \rightarrow 4 \mathcal{F}[N/4] \cdots \rightarrow N \mathcal{F}[1]$$

were $\mathcal{F}[N]$ indicates a Fourier transform of the order N which is divided by two, with the doubling of the number of Fourier transforms. Here the Fourier transform of the order one is simply equal to the input data [30].

In current software libraries the FFT is often realized for arbitrary N but is still optimized for N being a power of 2 or multiples of 2, 3 and 5 depending on prime factorization. This is also the case for the Open Computing Language (OpenCL) [31, 32] library 'clFFT' that has been used in this work, a detailed description can be found on the official website for AMD Compute

Libraries (ACL). So allowed values for N can be expressed in the following form

$$N = 2^x 3^y 5^z,$$

that gives reason to the sometimes unusual choice of N . For a better comparison the same values of N were used, even for the FFT method realized with help of the free software library 'Fastest Fourier Transform in the West' (FFTW) developed by Matteo Frigo and Steven G. Johnson at the MIT [33]. This subroutine library was implemented in the non-parallelized version of the program and principally allows arbitrary values of N .

5.5. Parallelization with OpenCL

The described procedure of using a FFT to solve the Dyson-Schwinger equations really accelerates the calculation and provides the possibility of reaching much higher numbers of lattice points. This is crucial in order to do a reliable analysis, but even more runtime can be saved: Another step regarding code optimization has been made by using the powerful tool of parallel programming. It was essentially defined by Almasi and Gottlieb (1989) [32] with the aim of a highly increased program performance. This benefit of runtime is caused by systematically parallelized computing steps that are allowed to be executed concurrently. The application programming interface (API) of choice to realize the parallelization of the C++ code was OpenCL. The hardware component that is eligible with respect to its construction properties to support these calculations is the Graphics Processor Unit (GPU). OpenCL enables a programmer to combine the use of Central Processing Units (CPU's) and GPU's and therefore computer-intensive parts of the program can be transferred to the GPU which architecture allows a concurrent evaluation.

In the following a short overview about how an OpenCL code can be constructed should be given, for detailed information and a lot of source code examples see in Ref. [31] or Ref. [32]. The advantage of OpenCL is that one can control a variety of devices from different vendors. Consequently GPU's from different vendors can be used by the same program with the help of several platforms which provide the vendor specific implementation of OpenCL. So the OpenCL API (administrated by the Khronos Group) gives an efficient access to a wide choice of hardware.

The relevant quantity considering a parallel process is the number of work-items. The part of a program offloaded to the GPU (called kernel) can be executed in parallel as many times as work-items are defined. So, for example a matrix multiplication of an order of N^2 can be perfectly parallelized by executing each step independently and in parallel. That is exactly what has to be done for the parallelization of the iteration method described in section 5.2. The parallelization would also be quite useful in order to solve equations that cannot be numerically simplified with the convolution theorem, as it would be the case for a dynamical inclusion of the static Lindhard susceptibility [16, 17].

With the OpenCL API at hand it was also successful to accelerate the FFT method by using the mentioned FFT algorithm provided by OpenCL (clFFT). This algorithm is already optimized and gives a simple access with regard to runtime optimization.

Unfortunately, the necessary preparation to finally get a kernel function that runs in parallel on a defined device with an appropriate platform is somewhat exhausting but is worthwhile in terms of these widely ranged possibilities.

In preparation one has to discover and initialize the mentioned platform as well as the devices that should be used. Furthermore a context has to be created, which provides an execution environment and manages the host-device interaction with the help of a command queue. All

the data needed inside the kernel have to be present on the device, so probably a lot of data have to be transferred from the host to the device before the program execution takes place and vice versa afterwards. The real source code is present in a character string and has to be imported to create a so called 'cl_program'. This program then contains the single kernels that have to be extracted from the compiled program. For this a wrapper class that quite nicely simplifies the whole procedure has been used. To even reduce the effort in setting arguments of a kernel, variadic templates were used which turned out to be quite comfortable. After the required preparation the kernel is ready to be executed on a huge number of work-items. The parallel calculations from this work were made on 'GeForce GTX TITAN' GPU's from Nvidia, the implemented platform is given by CUDA (vendor specific programming language from Nvidia).

5.6. Runtime Comparison

In this section a short review of the obtained runtime optimization is given. In Fig. 10 the solution method exploiting the convolution theorem is compared to solution method where the sum within the DSE is simply executed. For that, the needed time per iteration is plotted against the number of lattice points N . The time per iteration is averaged for different values of the coupling α to reach more reliable data.

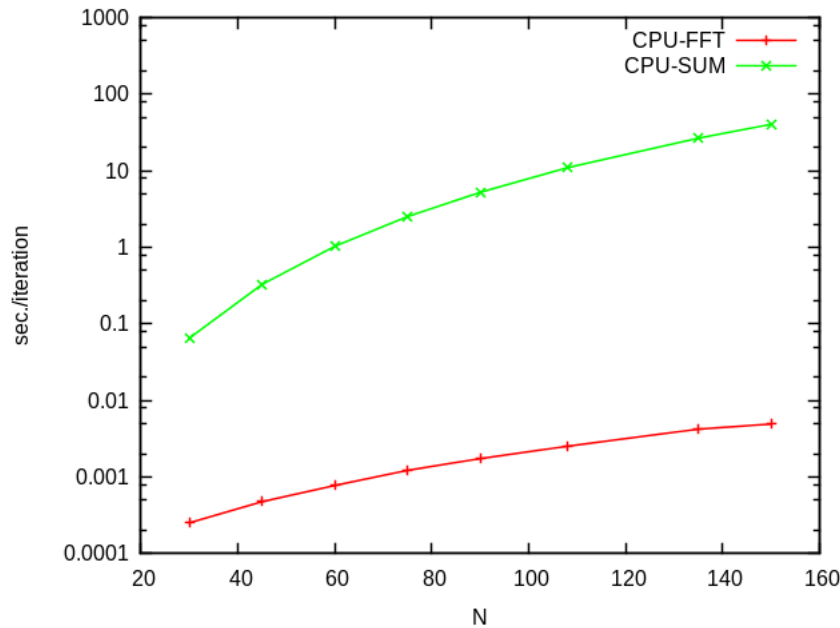


Figure 10: For comparison, the averaged time per iteration is plotted against the number of lattice points in one direction N for solving the DSE'S with neglected Fermi-velocity renormalization. This is plotted for the method using the convolution theorem as described in section 5.4 (FFT) and the method that simply executes the sum of Eq. (5.12) in every iteration step (SUM).

For a better comparison the time per iteration is plotted logarithmically. The range of N grows only up to $N = 150$, where the summation method already needs much more time. Obviously, by applying the convolution method from section 5.4 a great progress in saving runtime was made.

In Fig. 11 additionally the calculation on a CPU is compared to a calculation on a GPU (both

using the convolution method), where now much higher values of N can be obtained very easily. By using the GPU algorithm a lot of additional runtime can be saved as it is shown in Fig. 11, the GPU method is about 7 times faster than the calculation on a CPU.

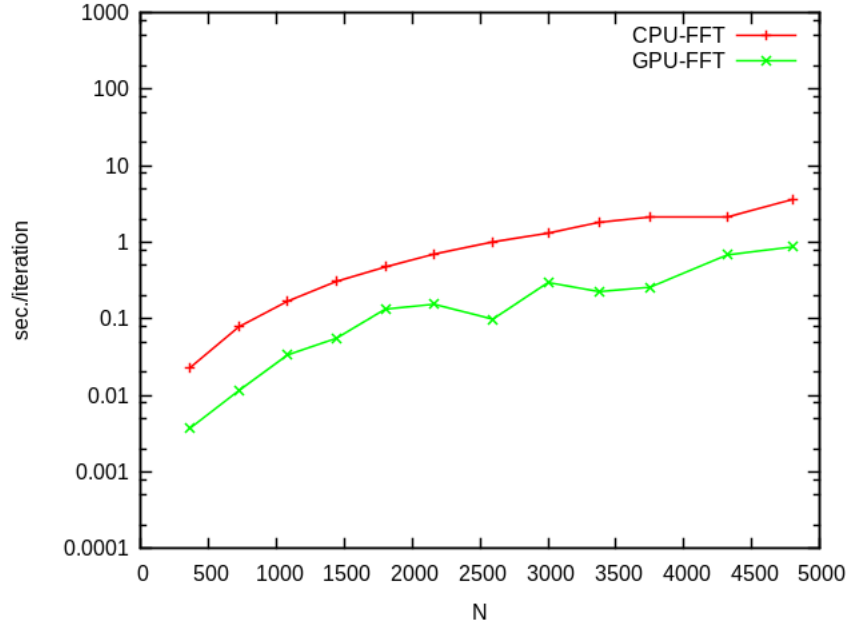


Figure 11: The solution method using the convolution theorem for the calculation on a CPU is compared to the same method calculated on a GPU.

That saves additional runtime but the crux of the matter was definitely to introduce the calculation scheme that lowers the order of calculation steps by using an FFT. Finally the calculation procedure has been sufficiently improved to reach volumes with which a reliable extraction of the critical coupling is possible.

6. Mass Renormalization

In this chapter the mass function $\mathcal{M}(\vec{q})$ should be investigated, while the Fermi-velocity renormalization is neglected. This rather simple problem can be solved analytically. This has been done in Ref. [14] and provides a critical coupling of $\alpha_c \approx 0.457$.

In order to recompute the analytically obtained critical coupling constant of Ref. [14], where the Fermi velocity renormalization and also screening effects were neglected, the dressing functions \mathcal{B}_1 and \mathcal{B}_2 simplify to their bare values:

$$\mathcal{B}_i(\vec{k}) = \mathbf{b}_i(\vec{k}). \quad (6.1)$$

So this chapter serves as a validity check for the applied calculation scheme where the whole band structure is taken into account (without low energy approximation). This ansatz leads to an exact discription and takes also the high momentum regime into account. So for the critical coupling we surely expect to find the analytical value.

6.1. Finite Volume Effects and Convergence

In the following equation (5.12) is solved by the convolution method described in section 5.4. The mass renormalization function is evaluated on the Dirac point K^+ .

This provides an order parameter for the semimetal-insulator phase transition due to the generation of a gap in the band structure. If there is a nontrivial solution of Eq. (5.12) the chiral condensate is nontrivial as well [7].

Equation (5.12) was solved for an increasing number of lattice points, in order to examine the convergence behaviour. The number of lattice points in one direction in momentum space is denoted by N , as introduced in section 4.2. Another advantage of the framework of Dyson-Schwinger equations is that the complete calculations for this approximation can be executed in the chiral limit, setting μ_3 to zero.

The number of lattice points in the following results varies from $N = 150$ to $N = 3000$ and increases in steps of about 150. With this number of lattice points we will see that the critical coupling can be deduced quite precisely. In previous calculations the critical coupling was even recomputed with a number of lattice points only up to 300.

To find the critical coupling Eq. (5.12) has to be solved additionally for different values of the coupling constant α .

For higher coupling constants in the insulator phase not close to the critical coupling the situation is rather unproblematic. In Fig. 12 the results for a few of these couplings are illustrated, the reciprocal number of lattice points in one dimension $1/N$ is plotted against the generated mass gap evaluated at the Dirac point K^+ in units of κ . In order to extrapolate to $N \rightarrow \infty$ it seems to be more significant to plot $M(K^+)$ against the reciprocal value of N .

In Fig. 13 the finite volume behaviour is plotted for couplings near the critical coupling together with the corresponding fits. One can see that the value for $M(K^+)$ seems to converge for higher N as one would expect for the integration of a $1/r$ -potential by a simple power count.

For the extrapolation to an infinite number of lattice points a polynomial fit up to the second order of $1/N$ was made:

$$f(x) = a \left(\frac{1}{N} \right)^2 + b \left(\frac{1}{N} \right) + c, \quad (6.2)$$

where c exactly delivers the value of M for an infinite number of lattice points: $c = M_\infty$.

In the overcritical regime (Fig. 12) an almost linear behaviour can be found; here it is very simple to extract a good approximation of M_∞ even for a very small number of lattice points.

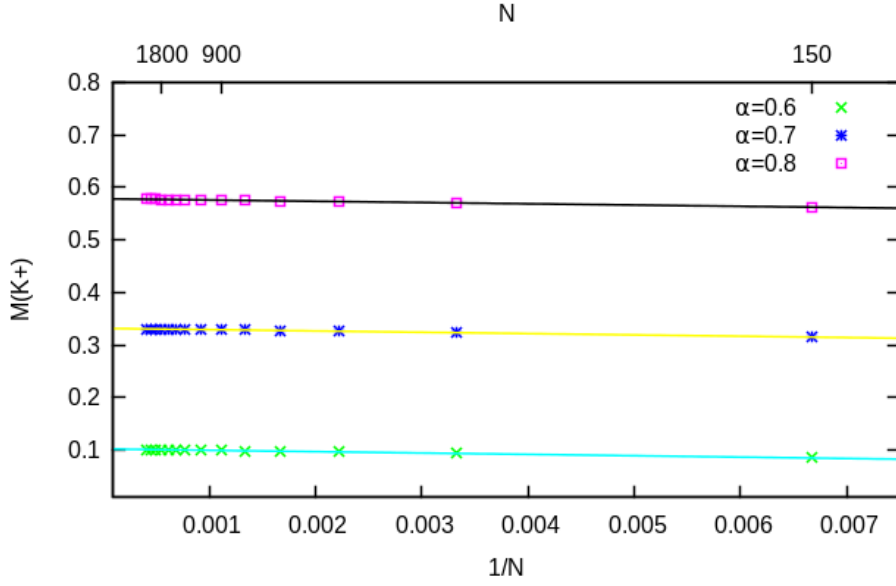


Figure 12: The generated gap at K^+ is plotted against the reciprocal of N for different α away from critical coupling. The datapoints are fitted quadratically as shown in Equation (6.2).

By continuing the consideration of smaller coupling constants (Fig. 13), obviously a quadratic fit is necessary to do reliable extrapolations. Principally it is of course possible to only use a linear fit but then one has to calculate up to a higher number of lattice points for such small coupling constants.

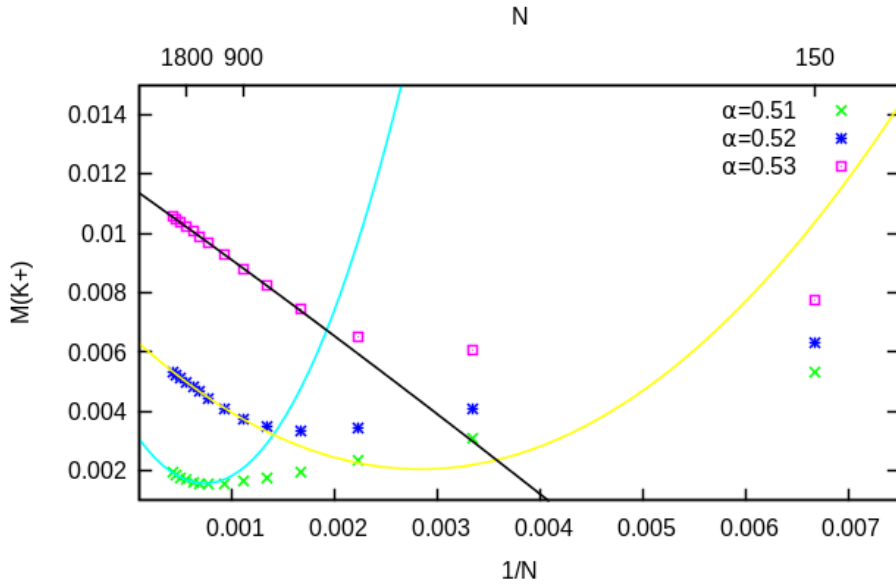


Figure 13: The convergence behaviour for the near-critical regime is plotted against the reciprocal number of lattice points.

In Fig. 13 a principal change of the convergence behaviour can be observed, a minimum evolves which seems to be shifted to larger N values as α decreases. One can now clearly see a deviation

from the linear behaviour. To get good extrapolation fits in the near-critical regime one has to discard the values lying on the right side of the minimum. They apparently do not provide a good estimate for higher lattice points. So with a decreasing coupling constant more and more values have to be rejected.

In Fig. 13 it is illustrated how the number of useable points for the extrapolation shrinks with a decreasing coupling constant. So there seems to be a natural constraint for coming closer to the critical coupling. The number of lattice points is too small to provide values on the left side of the minimum for coupling constants smaller than $\alpha = 0.5$. For smaller coupling constants a much higher number of lattice points is necessary, which is due to the fact that the achieved resolution in momentum space is always restricted by the smallest momentum unit $p = \frac{2\pi}{N}$ (analogous to an UV-cutoff).

The obtained error for the extraction of M_∞ from the fit parameter c is lying well below 1% for all coupling constants. But the errorbars obtained from the least square fit routine are not quite representative as discussed in section 5.3.

6.2. Critical Coupling

In Fig. 14 the extrapolated values M_∞ are plotted against the coupling constant. One can observe that the mass generation turns on at some value of α , which should be equal to $\alpha_c = 0.457$ due to analytical calculations [14] and calculations in the Dirac cone approximation [15]. In Ref. [15] also the typical Miransky scaling that can be deduced as general QED₃ phase transition effect [34, 7] could be verified.

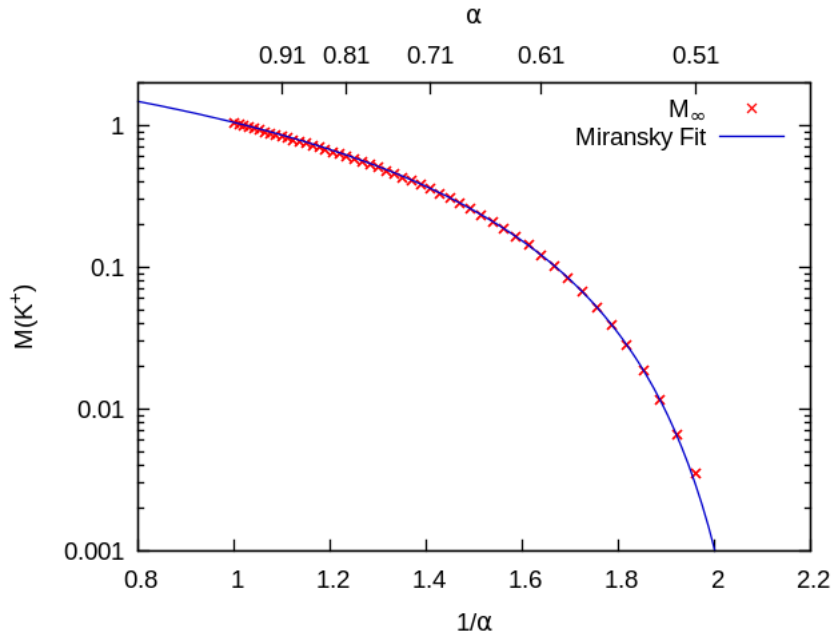


Figure 14: The extrapolated values for different coupling constants are plotted against the reciprocal coupling constant. A fit of Miransky-type has been applied and provides a good agreement with the data points.

In order to validate our calculation model we require a Miransky scaling behaviour reproducing the analytically obtained coupling constant. So our computed data points are fitted to the function:

$$M_\infty = a \exp\left(\frac{b}{\sqrt{\frac{1}{\alpha_c} - \frac{1}{\alpha}}}\right). \quad (6.3)$$

In Fig. 14 the obtained results are illustrated, where the part below the line, representing the phase transition, can be identified by the insulator phase of graphene. Here a nonzero chiral condensate emerges.

The corresponding fit parameters, where α_c identifies the critical coupling for the semimetal-insulator phase transition, are given by:

$$\begin{aligned} a &= 96.8091 \pm 2.913 \quad (3.009\%), \\ b &= -4.92754 \pm 0.03307 \quad (0.6711\%), \\ \alpha_c &= \mathbf{0.457847} \pm 0.0004941 \quad (0.1079\%). \end{aligned} \quad (6.4)$$

The analytically provided value of the critical coupling constant [14]

$$\alpha_c = \frac{8\pi^2}{\Gamma^4(1/4)} \approx 0.45695 \quad (6.5)$$

is consequently well recomputed.

So finally we can conclude that an appropriate accuracy has been reached for the recalculation of the critical coupling constant.

Another significant representation of the phase transition is depicted in Fig. 15.

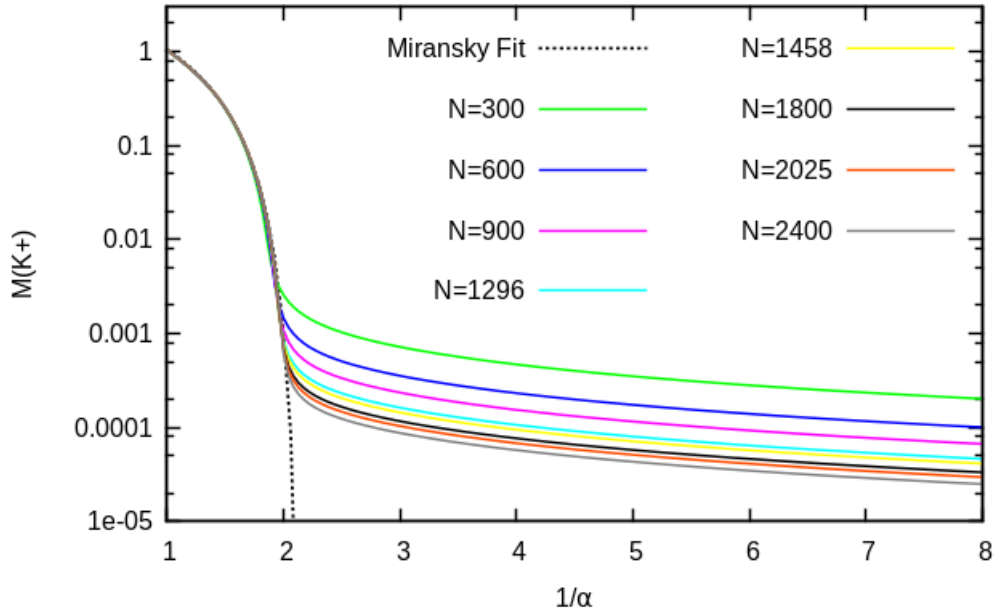


Figure 15: The mass renormalization function evaluated at K^+ is plotted against the reciprocal coupling constant for different lattice sizes. The Miransky-Fit from Fig. 14 is also shown for comparison.

Here the generated mass gap at the Dirac point is plotted against different couplings α for a variety of lattice point numbers N . Additionally the obtained Miransky-Fit is plotted and one can nicely observe how the Miransky behaviour is better and better reconstructed with an increasing number of lattice points.

Exactly the same calculation has been executed for a Coulomb interaction that was constructed in position space as it was worked out in section 4.2. So, we started with a potential in position space and directly applied our solution method using the advantage of the Fast Fourier Transform, described in section 5.4.

In Fig. 16 the results of this analysis is indicated by $M_\infty\text{-X}$, for comparison the results obtained from the potential given in momentum space are also illustrated ($M_\infty\text{-P}$).

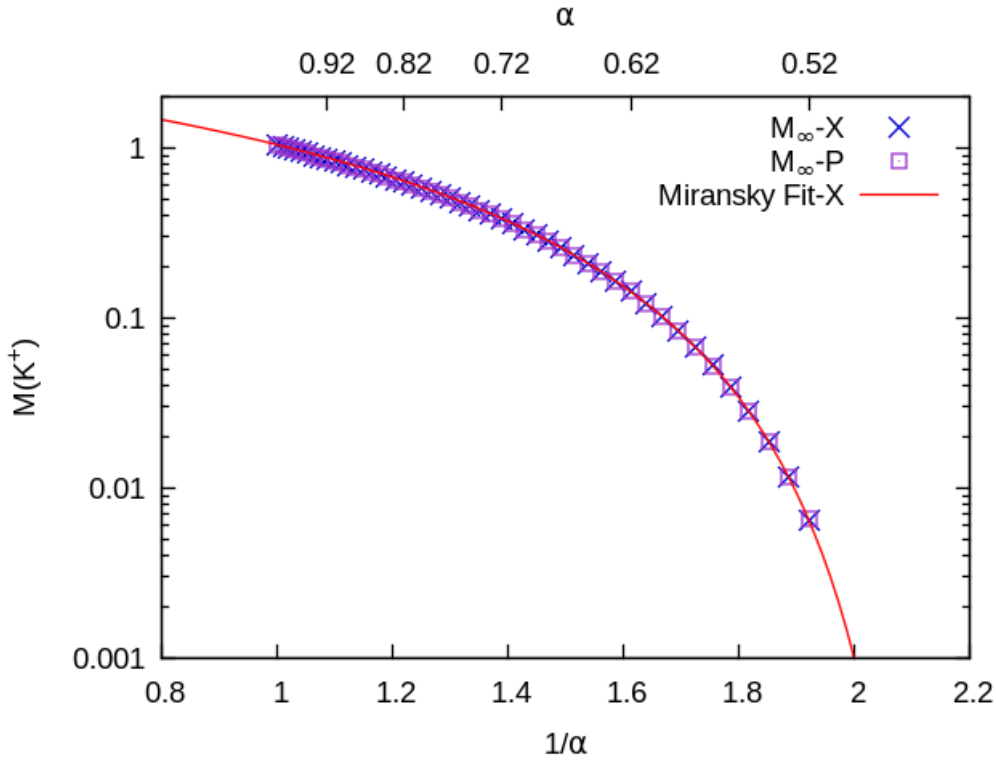


Figure 16: The extrapolated values are plotted against the reciprocal coupling constant. The obtained results for a constructed potential in position space and in momentum space are compared. A fit of Miransky-type has been applied to the data from a given potential in position space.

From these results a very good agreement of both calculations can be concluded. The data points gained with the potential in position space almost exactly match the data points obtained from the original discretized photon propagator in momentum space. Here the Miransky function 6.3 has been applied to the new data points $M_\infty\text{-X}$ and delivers almost the same fit parameters:

$$\begin{aligned}
 a &= 96.3753 \pm 2.186 \quad (2.268\%), \\
 b &= -4.92416 \pm 0.02493 \quad (0.5062\%), \\
 \alpha_c &= \mathbf{0.457847} \pm 0.0003726 \quad (0.08139\%).
 \end{aligned} \tag{6.6}$$

For reasonable comparison the Miransky-Fit has been applied to the data point region of $1/\alpha \in [1.5; 2.0]$ in both cases; this region of course is crucial to obtain a good consistency since the Miransky behaviour only has to hold in the regime near the critical coupling.

Ultimately, convincing arguments, to assume that the potential in position space was correctly implemented has been found. So, the basis to apply a more realistic potential that is typically given in position space has been elaborated.

6.3. Energy Dispersion

In the following the obtained energy dispersion relation where mass renormalization is included should be investigated.

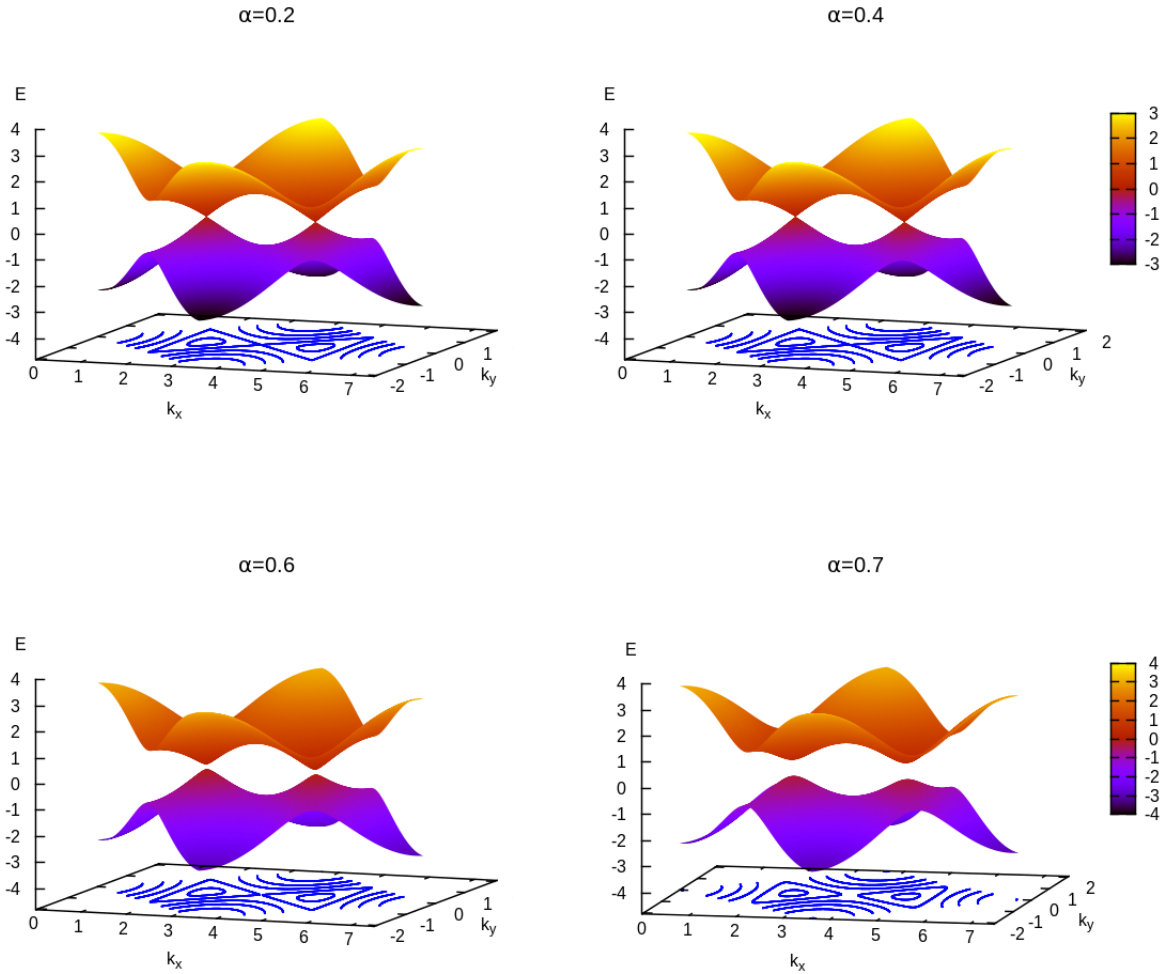


Figure 17: The energy relation for the first Brioullin zone is shown for different coupling constants in units of κ . The momenta are given in units of $1/a$.

In Fig. 17 the energy relation is plotted for the first BZ for different values of α . One can see the qualitative changes with an increasing coupling constant and the gap opening at a coupling between $\alpha = 0.4$ and $\alpha = 0.6$. Additionally a contour plot was applied from which the structure of the BZ can be deduced.

To gain a better insight into what happens to the dispersion relation, the energy-momentum relation is plotted along the high symmetry points of the BZ which was pointed out in Fig. 4.

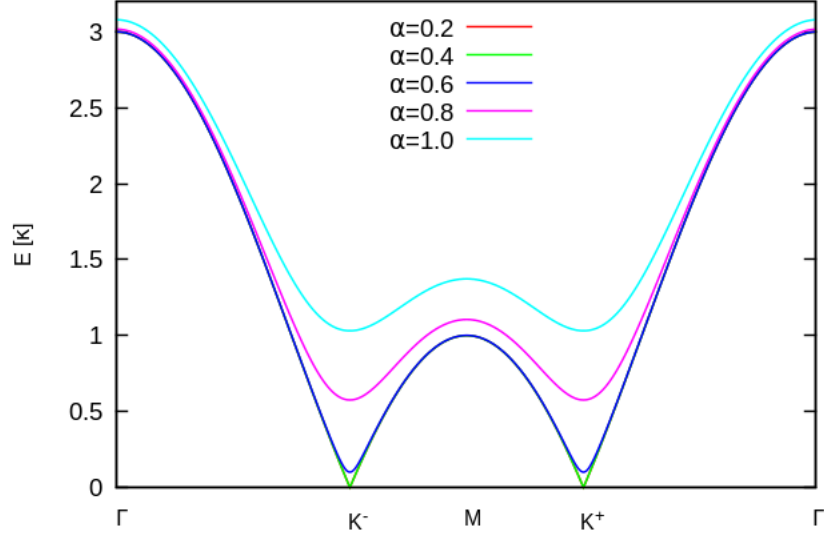


Figure 18: The energy-momentum relation is plotted along the high symmetry point of the Brioullin zone for different values of α .

This plot is illustrated in Fig. 18 where the gap opening can be nicely observed. For the values $\alpha = 0.2$ and $\alpha = 0.4$ the mass renormalization functions do not differ since the critical coupling is not reached. For higher values of α a gap evolves, which turns graphene into the insulator phase.

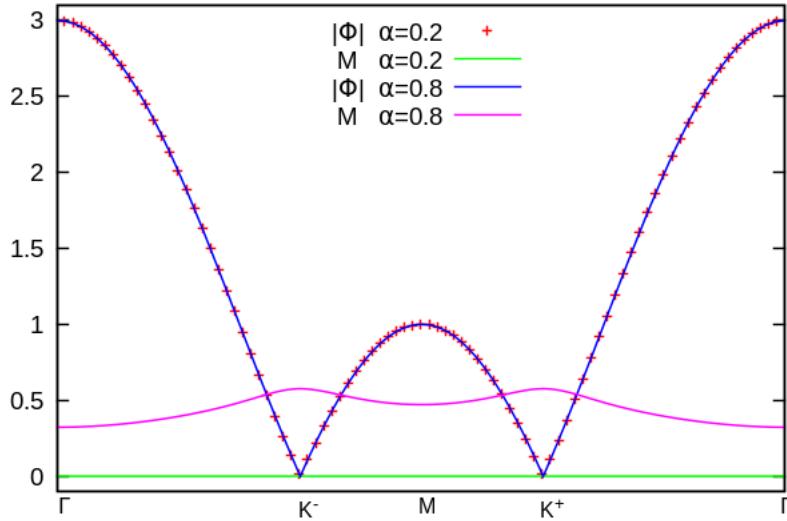


Figure 19: The single parts of the energy-momentum relation described in Eq. (6.7) are plotted along the high symmetry points for different couplings α . Obviously the Fermi-velocity renormalization has been neglected due to the similar values of $|\Phi|$ for the different values of α .

More precisely, the energy relation can still be decomposed into two parts:

$$E(\vec{k}) = \sqrt{\mathcal{M}^2(\vec{k}) + |\Phi(\vec{k})|^2} = \sqrt{\mathcal{M}^2(\vec{k}) + |\phi(\vec{k})|^2}. \quad (6.7)$$

In the current consideration the structure function has not been renormalized. Only the mass renormalization causes the deviation from the very original energy momentum-relation illustrated in Fig. 3. In Fig. 19 these two parts of the energy relation are depicted separately. As an example the mass renormalization function and the structure function are plotted for a coupling constant $\alpha = 0.2$ well below the critical coupling where neither a mass renormalization nor a renormalization of the structure function can be observed. In the case of $\alpha = 0.8$ a mass renormalization can be observed and of course the absolute value of the structure function remains bare.

This differences are very important to understand with regard to the next section, where the renormalization of the structure function - the so called Fermi-velocity renormalization - should be included.

7. Fermi-velocity Renormalization

In the following the renormalization of the whole band structure should be taken into account, that means the Dyson-Schwinger equation (5.2) for the structure function is now dynamically included in the calculation.

For that we have to take a thorough look at the used BZ. In the whole examination one important point has been ignored: The structure function is not periodic in the Brioullin zone that was considered until now. So principally the considerations which we have made until now for the Fermi-velocity renormalization and the Dyson-Schwinger equation of the structure function (Eq. (5.2)) seems to be wrong, regarding the evaluation on the primary BZ. In the next section we will develop a method to save the elaborated procedure and find a totally symmetric and periodic description of all these relevant quantities.

7.1. Converting the Hamiltonian to a smaller Unit Cell

The fact that the structure function is not periodic in the BZ which was chosen, can be understood by investigating the structure function in indices of the BZ (see Appendix B.1)

$$\phi_{mn} = \sum_{n=1}^3 e^{i\vec{k}\delta_n} = e^{\frac{2\pi i}{3N}(m-n)} + e^{\frac{2\pi i}{3N}(m+2n)} + e^{\frac{-2\pi i}{3N}(2m+n)}. \quad (7.1)$$

From that the shift invariance of the absolute value follows $|\phi_{mn}| = |\phi_{m+Nn}| = |\phi_{mn+N}|$ but the simple shift symmetry

$$\phi_{mn} \neq \phi_{m+Nn}, \quad \phi_{mn} \neq \phi_{mn+N},$$

is not valid! The valid symmetry transformations are rather given by

$$\phi_{m+Nn} = e^{\frac{2\pi i}{3}} \phi_{mn} \quad \text{and} \quad \phi_{mn+N} = e^{-\frac{2\pi i}{3}} \phi_{mn}.$$

So, if we are working with functions that are only depending on the absolute value of the structure function like e.g. the energy (Eq. (2.14)) there won't be a problem. But in case of a calculation with the independent parts $\mathbf{b}_1(\vec{k})$ and $\mathbf{b}_2(\vec{k})$ one has to be extremely cautious.

If the BZ should really be the smallest symmetry unit, a smaller elementary cell has to be considered (gaining a larger Brioullin zone in momentum space) so that even the structure function is periodic on that lattice. One possibility to represent the honeycomb lattice and all the connected functions periodically, is to use the basis vectors

$$\vec{a}'_1 = \vec{\delta}_1, \quad \vec{a}'_2 = \vec{\delta}_2, \quad (7.2)$$

where $\vec{\delta}_n$ ($n \in \{1, 2, 3\}$) again indicates the nearest neighbour vectors given by

$$\vec{\delta}_1 = a \begin{pmatrix} 0 \\ 1 \end{pmatrix}, \quad \vec{\delta}_2 = \frac{a}{2} \begin{pmatrix} \sqrt{3} \\ -1 \end{pmatrix}, \quad \vec{\delta}_3 = \frac{a}{2} \begin{pmatrix} -\sqrt{3} \\ -1 \end{pmatrix}.$$

Consequently the whole calculation has to be converted from the lattice given by the basis vectors \vec{a}_1 and \vec{a}_2 (see Eq. 2.1, forming Basis 1) to the lattice given by the basis vectors \vec{a}'_1 and

\vec{a}'_2 (Basis 2, see Appendix B.2 for a short summary). The two different representations of the lattice are depicted in Fig. 20.

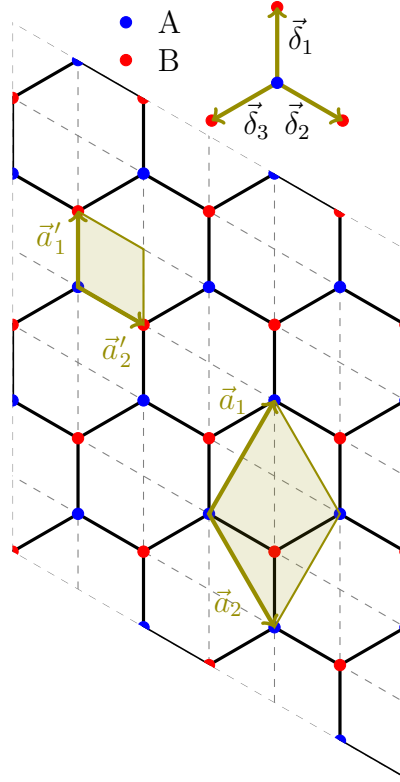


Figure 20: The different realizations of representing the honeycomb lattice (Basis 1, Basis 2) are illustrated by the corresponding basis vectors. Additionally the nearest-neighbour vectors $\vec{\delta}_n$ are shown.

The basis vectors \vec{a}_1 and \vec{a}_2 are representing the standard unit cell with which the analytically expected value for the critical coupling was successfully recomputed if the Fermi-velocity renormalization is neglected. The fact that the mass renormalization function only depends on the absolute value of the structure function assures the correctness of the results from the last section. The graphene lattice, constructed with \vec{a}_1 and \vec{a}_2 in fact requires a smaller Brioullin zone but the interatomic distances between A and B sublattice can not be resolved. That is why the structure function, necessarily depending on this distance is not periodic in this area. The associated Brioullin zone for each basis is shown in Fig. 21.

The corresponding basis vectors for the new lattice in momentum space are

$$\vec{b}'_1 = \frac{2\pi}{3a} \begin{pmatrix} \sqrt{3} \\ 3 \end{pmatrix}, \quad \vec{b}'_2 = \frac{4\pi}{3a} \begin{pmatrix} \sqrt{3} \\ 0 \end{pmatrix}. \quad (7.3)$$

On the new lattice a general vector in position space is similarly given by

$$\vec{r} = i \vec{a}'_1 + j \vec{a}'_2, \quad (7.4)$$

but not all lattice points are occupied by carbon atoms. Here we have three different types of sites: A and B sites, similarly to the former lattice and empty sites. Mathematically this can

be expressed by appropriate coefficients for red sites (A), blue sites (B) and empty sites (C):

$$\begin{aligned} \vec{x} &= i \vec{a}'_1 + j \vec{a}'_2 & (i+j)\%3 = 0 & \text{blue sites,} \\ \vec{y} &= i \vec{a}'_1 + j \vec{a}'_2 & (i+j)\%3 = 1 & \text{red sites,} \\ \vec{z} &= i \vec{a}'_1 + j \vec{a}'_2 & (i+j)\%3 = 2 & \text{empty sites,} \end{aligned} \quad (7.5)$$

where the % sign denotes the modulo operator. The complete lattice is indicated by G in the following ($G = A \cup B \cup C$). The momentum space is again naturally discretized via

$$\vec{p} = \frac{1}{N} (m \vec{b}'_1 + n \vec{b}'_2), \quad (7.6)$$

with $\vec{a}'_i \vec{b}'_j = 2\pi\delta_{ij}$.

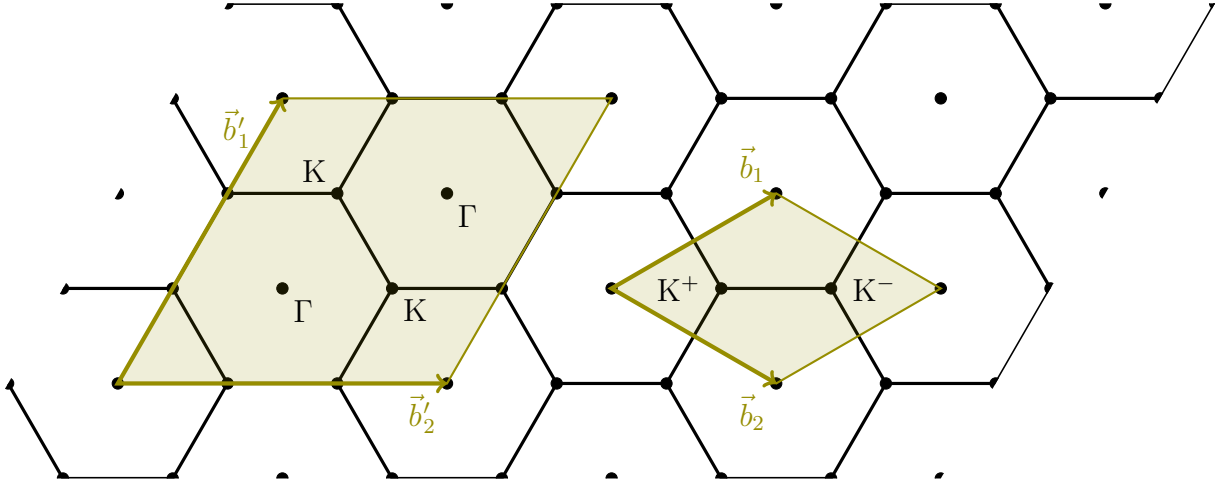


Figure 21: The corresponding BZ's of the different lattices in position space (see Fig. 20) are illustrated.

In the following the Hamiltonian from Eq. (3.3) has to be converted to the new basis as well as constructing a new potential that retains the elaborated properties. The free Hamiltonian in tight-binding approximation is still given by

$$\mathcal{H} = -\kappa \sum_{\langle x,y \rangle} (a_x^\dagger b_y + b_y^\dagger a_x) + \mu_3 \sum_{x,y} (a_x^\dagger a_x - b_y^\dagger b_y) - \mu \sum_{x,y} (a_x^\dagger a_x + b_y^\dagger b_y) \quad (7.7)$$

in position space. To obtain the corresponding Hamiltonian in momentum space we have to do a Fourier transform on the lattice, where now the creation and annihilation operators only exist on certain lattice points. So primarily, we have to think about how to do a Fourier transform only on a part of the lattice. The discrete Fourier transforms of these operators are given by

$$a_p = \sum_{r \in G} e^{-i\vec{p}\vec{r}} a_r \Big|_{r \in A} = \sum_{x \in A} e^{-i\vec{p}\vec{x}} a_x = \sum_{x_{ij} \in A} e^{-\frac{2\pi i}{N}(im+jn)} a_x \quad (7.8)$$

$$b_p = \sum_{y \in B} e^{-i\vec{p}\vec{y}} b_y \quad (7.9)$$

and analogically for the annihilation operators. These restrictions on either A sites, B sites or

empty sites can also be expressed by introducing the following function

$$Z(i, j, r) = \frac{1}{3} \left(1 + e^{-\frac{2\pi i}{3}(i+j-r)} + e^{-\frac{4\pi i}{3}(i+j-r)} \right) = \begin{cases} 1, & (i+j)\%3 = r \\ 0, & \text{else} \end{cases} \quad (7.10)$$

with $r \in \{0, 1, 2\}$ for the different lattice types. The multiplication of this function will always assure that a function only exists on one of the three lattice types and therefore provide a neat way of calculation.

For functions that are only existing on one of the three types of lattice sites a shift symmetry in momentum space is obtained:

$$F(m, n) = \sum_{(i+j)\%3=r} e^{-\frac{2\pi i}{N}(im+jn)} F(i, j), \quad (7.11)$$

$$F(m + Nk/3, n + Nk/3) = z^{-kr} F(m, n), \quad (7.12)$$

with $z = e^{\frac{2\pi i}{3}}$ and the corresponding momentum vector $p(m + Nk/3, n + Nk/3) = \vec{p}_k = \frac{k}{3}(\vec{b}_1 + \vec{b}_2)$. So the BZ for such functions can be divided into three independent areas. The different areas are shown in Fig. 22.

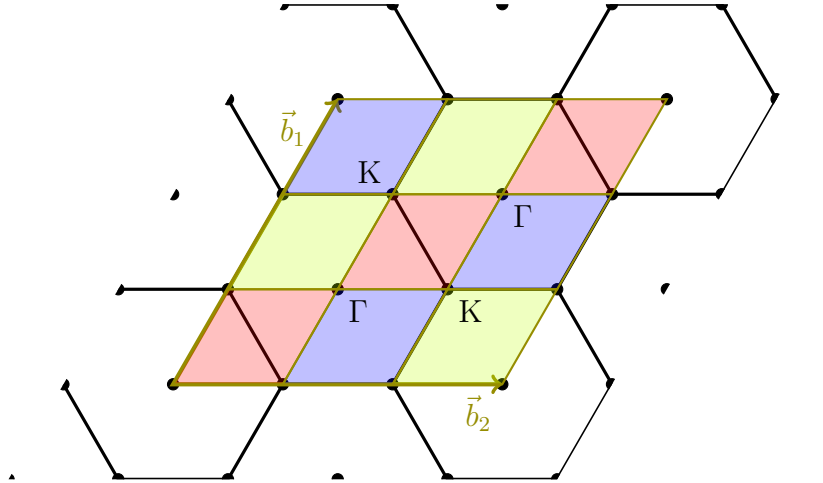


Figure 22: Shown is the decomposition of the Brioullin zone into the several symmetry contributions. The different colored areas are independent from each other, but the same-colored parts can be converted into each other by certain symmetry transformations if the function only exist on one lattice type in position space.

The three different colored areas are independent from each other, the surface area of this three independent parts exactly equates to the area of one honeycomb or rather the area of the old BZ (Basis 1). If a function is only defined on A sites ($r=0$) all same-colored parts of the Brioullin zone are identical. For functions that are existing either on B sites or empty sites the same-colored areas can be converted into each other with the help of the appropriate symmetry transformation (Eq. (7.12)).

So obviously the description on this small lattice in position space is needed for functions which depend on the interatomic distance of A sites and B sites ($r=1$). Functions that are only depending on the atomic distance between similar sites are exactly equal in these areas ($r=0$).

Consequently for the mass renormalization it would be sufficient to do the whole computation on the smaller Brioullin zone, but here graphenes structure function (depending on A-B distances) is not periodic anymore.

From equation (7.12) similarly the shift symmetry for the creation and annihilation operators follow

$$a_{p+p_k} = a_p \quad \text{and} \quad b_{p+p_k} = z^{-k} b_p. \quad (7.13)$$

By using the following relation for a partial sum over the lattice (this can be derived by writing out the sum of the right hand side):

$$w(m, n, r) = \sum_{(i+j)\%3=r} e^{-\frac{2\pi i}{N}(im+jn)} = \frac{1}{3} \sum_{k=0}^2 z^{rk} \delta(\vec{p} - \vec{p}_k), \quad (7.14)$$

one can perform the Fourier transformation of the single terms in the free Hamiltonian from equation (7.7),

$$\mathcal{H}_0^{ab} = -\kappa \sum_{\langle x, y \rangle} a_x^\dagger b_y = -\kappa \sum_{x \in A} \sum_{n=1}^3 a_x^\dagger b_{x+\delta_n} = -\frac{\kappa}{N^4} \sum_{x \in A} \sum_{n=1}^3 \sum_{p, q \in \mathcal{BZ}'} e^{-i\vec{p}\vec{x}} e^{i\vec{q}(\vec{x}+\vec{\delta}_n)} a_p^\dagger b_q \quad (7.15)$$

$$= -\kappa \frac{1}{3N^2} \sum_{n=1}^3 \sum_{p, q \in \mathcal{BZ}'} \sum_{k=0}^2 \delta(\vec{q} - (\vec{p} + \vec{p}_k)) e^{i\vec{q}\vec{\delta}_n} a_p^\dagger b_q, \quad (7.16)$$

where \mathcal{BZ}' is now the BZ of the new basis.

With the equations from (7.13) and $e^{i\vec{p}_k\vec{\delta}_n} = z^k$ one finds

$$\mathcal{H}_0^{ab} = -\frac{\kappa}{N^2} \sum_{p \in \mathcal{BZ}'} \sum_{n=1}^3 e^{i\vec{p}\vec{\delta}_n} a_p^\dagger b_p, \quad (7.17)$$

so the z -factors identically cancel and we end up with the already known result from Basis 1 (Eq. (2.8) and (2.9)). For the other parts of the free Hamiltonian, similar relations can be deduced:

$$\mathcal{H}_0^{ba} = -\kappa \sum_{\langle x, y \rangle} b_y^\dagger a_x = -\frac{\kappa}{N^2} \sum_{p \in \mathcal{BZ}'} \sum_{n=1}^3 e^{-i\vec{p}\vec{\delta}_n} b_p^\dagger a_p, \quad (7.18)$$

$$\mathcal{H}_m^a = m \sum_{x \in A} a_x^\dagger a_x = \frac{m}{N^2} \sum_{p \in \mathcal{BZ}'} a_p^\dagger a_p, \quad (7.19)$$

$$\mathcal{H}_m^b = m \sum_{y \in B} b_y^\dagger b_y = \frac{m}{N^2} \sum_{p \in \mathcal{BZ}'} b_p^\dagger b_p. \quad (7.20)$$

So the Hamiltonian can be represented in momentum space and is again completely given by (compare to Eq. (2.8) with the full Hamiltonian (3.3))

$$\mathcal{H} = (\mathcal{H}_0^{ab} + \mathcal{H}_0^{ba}) + (\mathcal{H}_{\mu_3}^a - \mathcal{H}_{\mu_3}^b) - (\mathcal{H}_\mu^a - \mathcal{H}_\mu^b) \quad (7.21)$$

$$= \frac{1}{N^2} \sum_{p \in \mathcal{BZ}'} \begin{pmatrix} a_p^\dagger & b_p^\dagger \end{pmatrix} \begin{pmatrix} \mu_3 - \mu & -\phi(\vec{p}) \\ -\phi^*(\vec{p}) & -\mu_3 - \mu \end{pmatrix} \begin{pmatrix} a_p \\ b_p \end{pmatrix}. \quad (7.22)$$

Hence exactly the same structure as in the calculation for Basis 1 (compare to Eq. (3.3)) is

obtained, which is not surprisingly due to the fact that the energy should remain the same. But now we are really calculating on a lattice where all the functions that we need are totally periodic.

The structure function on this basis can then be written as (see Appendix B.2)

$$\phi(\vec{p}) = \phi_{mn} = \kappa \left(e^{\frac{2\pi i}{N}m} + e^{\frac{2\pi i}{N}n} + e^{\frac{2\pi i}{N}(m+n)} \right). \quad (7.23)$$

From that the associated symmetry transformations follow immediately:

$$\begin{aligned} \phi_{m+N,n} &= \phi_{n,m+N} = \phi_{m,n}, \\ \phi_{m,n} &= \phi_{n,m}, \\ \phi_{N-m,N-n} &= \phi_{m,n}^*, \\ \phi_{m+Nk/3,n+Nk/3} &= z^k \phi_{m,n} \iff \phi(\vec{p} + \vec{p}_k) = z^k \phi(\vec{p}_k), \end{aligned} \quad (7.24)$$

so the structure function is now periodic and the Brioullin-zone really is the smallest symmetry unit in momentum space. Additionally it was demonstrated, that one finally gets exactly the same Dressing functions for this lattice as for Basis 1, but has to evaluate the integral over the large Brioullin zone of Basis 2. Structurally the DSE's of Eq. (5.15) are completely identical based on the same Hamiltonian in momentum space. So we now obtain completely symmetric and translational invariant versions of the DSE's from Eq. (5.12) and Eq. (5.13)

$$M_{\vec{k}} = \mu_3 + c \alpha \sum_{\vec{q} \in \mathcal{BZ}'} \mathcal{V}_{\vec{q}-\vec{k}} \frac{M_{\vec{q}}}{\Omega_{\vec{q}}}, \quad (7.25)$$

$$\Phi_{\vec{k}} = \phi_{\vec{k}} + c \alpha \sum_{\vec{q} \in \mathcal{BZ}'} \mathcal{V}_{\vec{q}-\vec{k}} \frac{\Phi_{\vec{q}}}{\Omega_{\vec{q}}}, \quad (7.26)$$

with Ω from section 3.2. This verification of symmetry conservation allows a shift in momentum space, so the DSE's can be equivalently written as

$$\begin{aligned} M_{\vec{k}} &= \mu_3 + c \alpha \sum_{\vec{q} \in \mathcal{BZ}'} \mathcal{V}_{\vec{q}} \frac{M_{\vec{k}+\vec{q}}}{\Omega_{\vec{k}+\vec{q}}}, \\ \Phi_{\vec{k}} &= \phi_{\vec{k}} + c \alpha \sum_{\vec{q} \in \mathcal{BZ}'} \mathcal{V}_{\vec{q}} \frac{\Phi_{\vec{k}+\vec{q}}}{\Omega_{\vec{k}+\vec{q}}}. \end{aligned} \quad (7.27)$$

in the discretized form, with c is now given via \mathcal{BZ}' indicating the BZ of the new lattice (Basis 2). All renormalization functions are now discretized within the new lattice.

7.2. Coulomb Potential on the new Lattice

So now the potential has to be discretized on a new lattice. For a sublattice interaction between either A sites or B sites, there won't be a problem. Such a potential should be even periodic on the small Brioullin zone ($r=0$ in Eq. (7.12)), but for an interaction between A and B sites we have again the problem that this function is not periodic on the small BZ.

Accordingly, this problem has to be considered on the small unit cell to be able to take the interaction between two adjacent carbon atoms into account.

If the interaction between the two sublattices should be taken into account, distances $(\vec{x} - \vec{y})$ where $\vec{x} \in A$ and $\vec{y} \in B$ has to be included. On the grounds that this interaction matrix only depends on the distance between the relevant sites, the A site can be fixed to the origin. Then

only the interaction with all B sites of the lattice has to be considered. Generally one has to distinguish between two kinds of interaction, the interaction between similar sites, denoted by \mathcal{V}^A and the interaction between sites from different sublattices (\mathcal{V}^{AB}).

So the interaction can be simplified by:

$$\mathcal{V}^A(\vec{r}) = \mathcal{V}(\vec{x} - \vec{y})|_{\vec{x}, \vec{y} \in A} = \mathcal{V}(\vec{r})|_{\vec{r} \in A}, \quad (7.28)$$

$$\mathcal{V}^{AB}(\vec{r}) = \mathcal{V}(\vec{x} - \vec{y})|_{\vec{x} \in A, \vec{y} \in B} = \mathcal{V}(\vec{r})|_{\vec{r} \in B}, \quad (7.29)$$

with an A site in the origin. The relation between these potentials and their counterparts \mathcal{V}^B and \mathcal{V}^{BA} in momentum space is deduced in Appendix E. With that it should be possible to convert the formalism to the old BZ again (Basis 1), but it has not been tested numerically yet.

By considering the potential in momentum space one finds the representation of the potential between similar sites in terms of a Fourier transformed potential defined on the whole lattice:

$$\begin{aligned} \mathcal{V}_{\vec{p}}^A &= \sum_{\{i,j\} \in G} \mathcal{V}_{ij}|_{\{i,j\} \in A} e^{-\frac{2\pi i}{N}(im+jn)} \\ &= \sum_{\{i,j\} \in G} \mathcal{V}_{ij} e^{-\frac{2\pi i}{N}(im+jn)} \frac{1}{3} \left(1 + e^{-\frac{2\pi i}{3}(i+j)} + e^{-\frac{4\pi i}{3}(i+j)} \right) \\ &= \frac{1}{3} \sum_{\{i,j\} \in G} \mathcal{V}_{ij} \left(e^{-\frac{2\pi i}{N}(im+jn)} + e^{-\frac{2\pi i}{N}(i(m+N/3)+j(n+N/3))} + e^{-\frac{2\pi i}{N}(i(m+2N/3)+j(n+2N/3))} \right) \\ &= \frac{1}{3} \sum_{k=0}^2 \mathcal{V}_{\vec{p}+\vec{p}_k} \end{aligned} \quad (7.30)$$

with

$$\mathcal{V}_{\vec{p}} = \sum_{\{i,j\} \in G} \mathcal{V}_{ij} e^{-\frac{2\pi i}{N}(im+jn)}. \quad (7.31)$$

From that the required symmetry (see Eq. (7.12)) follows directly:

$$\mathcal{V}_{\vec{p}+\vec{p}_k}^A = \mathcal{V}_{\vec{p}}^A. \quad (7.32)$$

The equivalent consideration for \mathcal{V}^{AB} yields:

$$\begin{aligned} \mathcal{V}_{\vec{p}}^{AB} &= \sum_{\{i,j\} \in G} \mathcal{V}_{ij}|_{\{i,j\} \in B} e^{-\frac{2\pi i}{N}(im+jn)} \\ &= \sum_{\{i,j\} \in G} \mathcal{V}_{ij} e^{-\frac{2\pi i}{N}(im+jn)} \frac{1}{3} \left(1 + e^{-\frac{2\pi i}{3}(i+j+2)} + e^{-\frac{4\pi i}{3}(i+j+2)} \right) \\ &= \sum_{\{i,j\} \in G} \mathcal{V}_{ij} \left(e^{-\frac{2\pi i}{N}(im+jn)} + e^{-\frac{4\pi i}{3}} e^{-\frac{2\pi i}{N}(i(m+N/3)+j(n+N/3))} + e^{-\frac{8\pi i}{3}} e^{-\frac{2\pi i}{N}(i(m+2N/3)+j(n+2N/3))} \right) \\ &= \frac{1}{3} \left(\mathcal{V}_{\vec{p}} + e^{\frac{2\pi i}{3}} \mathcal{V}_{\vec{p}+\vec{p}_1} + e^{\frac{4\pi i}{3}} \mathcal{V}_{\vec{p}+\vec{p}_2} \right) \\ &= \frac{1}{3} \sum_{k=0}^2 e^{\frac{2\pi i}{3}k} \mathcal{V}_{\vec{p}+\vec{p}_k} \end{aligned}$$

and provides the expected symmetry as well:

$$\mathcal{V}_{\vec{p}+\vec{p}_k}^{AB} = e^{\frac{-2\pi i}{3}k} \mathcal{V}_{\vec{p}}^{AB} = z^{-k} \mathcal{V}_{\vec{p}}^{AB}. \quad (7.33)$$

The influence from both interactions simply add in momentum space

$$\mathcal{V}_{\vec{p}}^{A,AB} = \sum_{\substack{x \in A \\ y \in AB}} \mathcal{V}_{xy} e^{-i\vec{p}(\vec{x}-\vec{y})} = \sum_{\substack{(i+j)\%3=0 \\ (i+j)\%3=1}} \mathcal{V}_{xy} e^{\frac{2\pi i}{N}(im+jn)} = \mathcal{V}_{\vec{p}}^A + \mathcal{V}_{\vec{p}}^{AB}, \quad (7.34)$$

since the sum can always be decomposed in the single contributions

$$\sum_{\{i,j\} \in G} = \sum_{(i+j)\%3=0} + \sum_{(i+j)\%3=1} + \sum_{(i+j)\%3=2}. \quad (7.35)$$

This leads to

$$\mathcal{V}_{\vec{p}+\vec{p}_k}^{A,AB} = \mathcal{V}_{\vec{p}}^A + z^{-k} \mathcal{V}_{\vec{p}}^{AB}. \quad (7.36)$$

Both potentials $\mathcal{V}_{\vec{p}}^A$ (left) and $\mathcal{V}_{\vec{p}}^{A,AB}$ (right) are illustrated in Fig. 23.

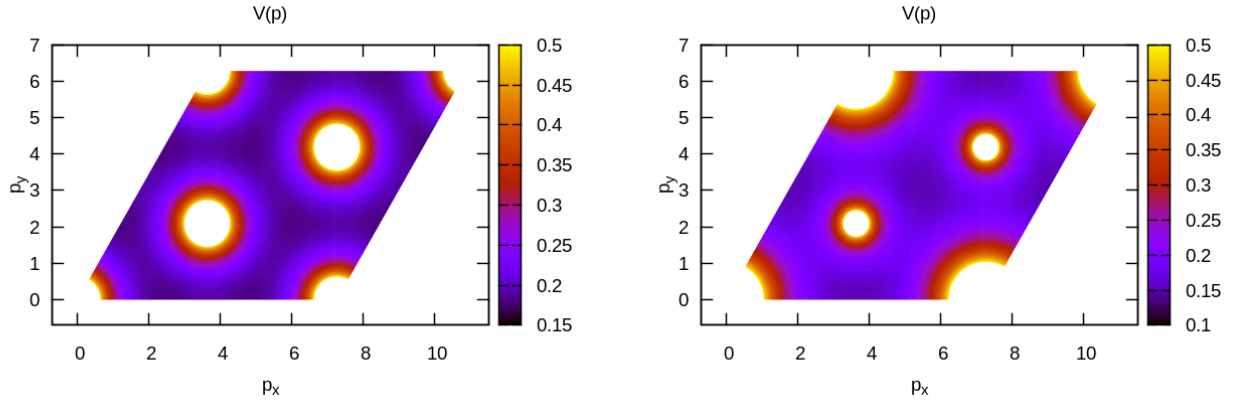


Figure 23: The potentials for the different interaction types are shown in momentum space: \mathcal{V}^A on the left hand side and $\mathcal{V}^{A,AB}$ on the right hand side. They have been obtained by a Fourier transform of the appropriate potential in position space. For a better view on the structure the z -range is restricted to $z = 0.5$.

It can be observed that the symmetry from Eq. (7.32) is valid in case of the left picture, for the potential on the right hand side this symmetry is broken, as expected. These potentials were again calculated in position space and then transformed into momentum space. The on-site term in position space can either be calculated by Eq. (4.19) on the old basis (the on-site term should remain the same) or on the basis of Eq. (7.30). Interactions with B or C sites would not contribute to the on-site repulsion anyway, as it is shown in the following. By using the on-site term of Basis 1 one might consider a factor of $1/3$ in terms of the three times larger Brioullin zone.

The DSE's from Eq. (5.12) and Eq. (5.13) then yield

$$\begin{aligned} M_{\vec{k}} &= \mu_3 + c \alpha \sum_{\vec{q} \in \mathcal{BZ}'} \mathcal{V}_{\vec{q}}^{A,AB} \frac{M_{\vec{k}+\vec{q}}}{\Omega_{\vec{k}+\vec{q}}}, \\ \Phi_{\vec{k}} &= \phi_{\vec{k}} + c \alpha \sum_{\vec{q} \in \mathcal{BZ}'} \mathcal{V}_{\vec{q}}^{A,AB} \frac{\Phi_{\vec{k}+\vec{q}}}{\Omega_{\vec{k}+\vec{q}}}. \end{aligned} \quad (7.37)$$

These are the equations we have finally used to even take the Fermi-velocity renormalization into account.

If we split the sum over the BZ in three areas (analogically to the three rows from Fig. 22):

$$\sum_{\vec{q} \in \mathcal{BZ}'} \longrightarrow \sum_{k=0}^2 \sum_{\vec{q}},$$

where \vec{q} only covers the independent part of the BZ (for example the first row indicated by \mathcal{B}_3), we find the following relations

$$\begin{aligned} M_{\vec{p}} &= \mu_3 + c \alpha \sum_{k=0}^2 \sum_{\vec{q} \in \mathcal{B}_3} (\mathcal{V}_{\vec{q}}^A + z^{-k} \mathcal{V}_{\vec{q}}^{AB}) \frac{M_{\vec{p}+\vec{q}}}{\Omega_{\vec{p}+\vec{q}}} \\ &= \mu_3 + 3 c \alpha \sum_{\vec{q} \in \mathcal{B}_3} \mathcal{V}_{\vec{q}}^A \frac{M_{\vec{p}+\vec{q}}}{\Omega_{\vec{p}+\vec{q}}} \\ &= \mu_3 + c \alpha \sum_{\vec{q} \in \mathcal{BZ}'} \mathcal{V}_{\vec{q}}^A \frac{M_{\vec{p}+\vec{q}}}{\Omega_{\vec{p}+\vec{q}}} \\ \Phi_{\vec{p}} &= \phi_{\vec{p}} + c \alpha \sum_{k=0}^2 \sum_{\vec{q} \in \mathcal{B}_3} (\mathcal{V}_{\vec{q}}^A + z^{-k} \mathcal{V}_{\vec{q}}^{AB}) z^k \frac{\Phi_{\vec{p}+\vec{q}}}{\Omega_{\vec{p}+\vec{q}}} \\ &= \phi_{\vec{p}} + 3 c \alpha \sum_{\vec{q} \in \mathcal{B}_3} \mathcal{V}_{\vec{q}}^{AB} \frac{\Phi_{\vec{p}+\vec{q}}}{\Omega_{\vec{p}+\vec{q}}} \\ &= \phi_{\vec{p}} + c \alpha \sum_{\vec{q} \in \mathcal{BZ}'} \mathcal{V}_{\vec{q}}^{AB} \frac{\Phi_{\vec{p}+\vec{q}}}{\Omega_{\vec{p}+\vec{q}}} \end{aligned} \quad (7.38)$$

by using the transformations from Eq. (7.36) and Eq. (7.24) and $\sum_{k=0}^2 z^{-k} = \sum_{k=0}^2 z^k = 0$. Additionally, the symmetries of the renormalization functions were used:

$$M_{\vec{p}+\vec{p}_k} = M_{\vec{p}} \quad \text{and} \quad \Phi_{\vec{p}+\vec{p}_k} = z^k \Phi_{\vec{p}}. \quad (7.39)$$

So, principally we are able to convert the integral to the small Brioullin zone again by exploiting the known symmetry transformations. For that we have to know how to construct the interaction between A and B sites on the Basis 1, an ansatz has been made in Appendix E but has not been tested numerically yet.

That is exactly what we would expect from the diagrammatical consideration (see section 4.1.1) the different parts of the fermion propagator are only influenced by certain interactions. So a possible Fermi-velocity renormalization can only come from an interaction between A and B sites. Furthermore, if an interaction between A sites and C sites is additionally included (that would equate to the potential given in Eq. (7.31)), nothing would change due to the z -symmetry and the shift invariance of the other parts of the DSE's. That is exactly what could be confirmed numerically. The same results as generated with a potential which only

takes the interaction between A and B sites into account, can be obtained with a potential even considering empty sites. The obtained potential by taking all lattice points into account is illustrated in Fig. 24 in momentum space and is of course quite similar to that of the old basis (Basis 1).

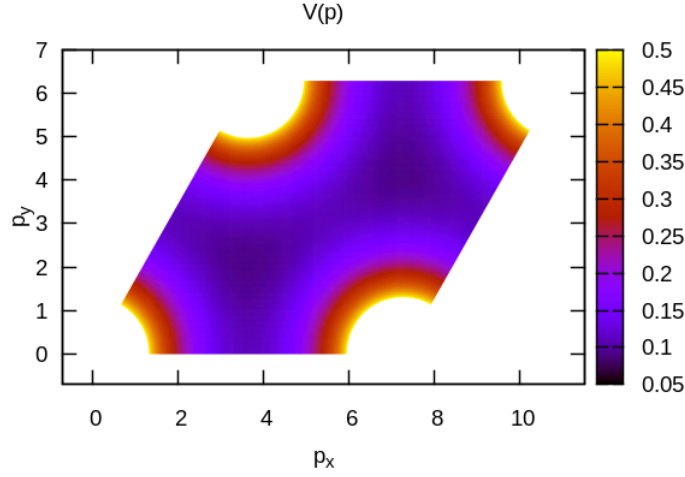


Figure 24: The potential of equation (7.31) is illustrated on the Brioullin zone. It delivers the same results as obtained from $V^{A,AB}$ due to the shift invariance of the Brioullin zone. The z-range is again limited at $z = 0.5$.

This kind of potential was used to include a more realistic potential in chapter 8. For a comparison, in Fig. 25 the associated potentials in position space are plotted along the index i (see (7.4)) identifying the y-axis. \mathcal{V}^A and \mathcal{V}^{AB} equate to zero at the appropriate lattice points.

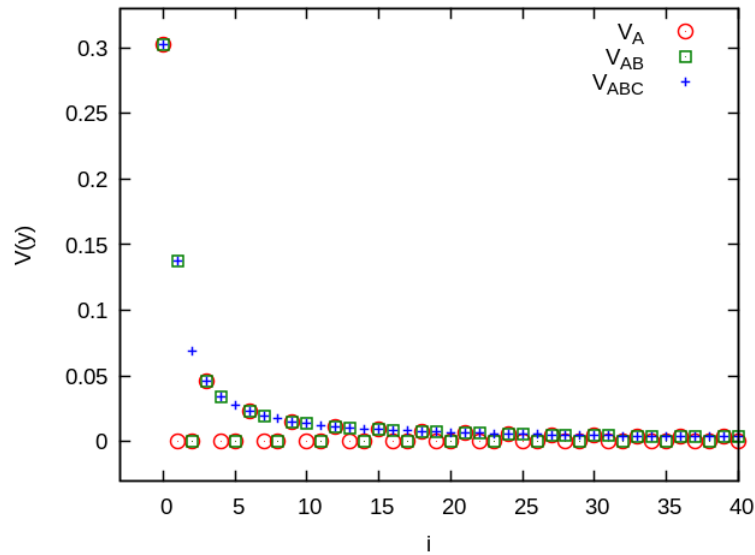


Figure 25: For a comparison the considered potentials from this chapter are plotted against the index i of the position space vector(see Eq. (7.4)) indicating the y-axis.

7.3. Validation of the new Basis (Basis 2)

At first, as a cross check of the whole examination the analytical value of the last chapter should be also reproduced for the new Brioullin zone with the adapted potential. For that the calculations described in the last section were completely repeated, with a potential constructed in position space and taking the Coulomb interaction between all carbon atoms into account. If then only the mass renormalization function is iterated one would expect the same result as obtained on the small BZ, that was shown in the last section: The interaction between electrons from different sublattices do not influence the mass renormalization function (see Eq. (7.38)). Alternatively, if the iteration of the structure function is included but the potential given by \mathcal{V}^A is used, exactly the same results were obtained. This kind of interaction cannot cause a Fermi-velocity renormalization as it was shown in the last section. And that is exactly what was found numerically.

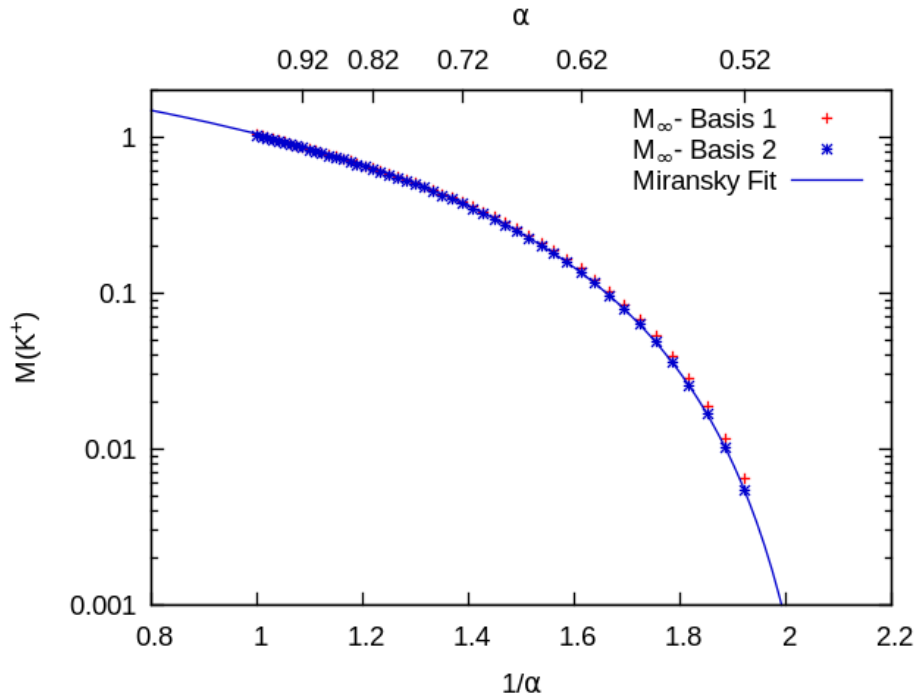


Figure 26: The energy gap is plotted against the reciprocal value of α for the new Brioullin zone (Basis 1) and has been fitted to the function of Eq. (6.3), in expectation of a similar scaling behaviour as on the former lattice (Basis 1). For a better comparison also the results from Basis 1 are shown.

As expected we obtain the same finite volume behaviour as represented in section 6.1 and therefore did exactly the same extrapolation. In Fig. 26 a comparison of the extrapolated ($N \rightarrow \infty$) values for Basis 1 and Basis 2 are shown. The values calculated on Basis 2 were again fitted to the scaling behaviour expected in case of a phase transition of Miransky-type (Eq. (6.3)). The following parameters were obtained

$$\begin{aligned}
 a &= 108.186 \pm 2.508 \quad (2.318\%), \\
 b &= -5.03867 \pm 0.02547 \quad (0.5056\%), \\
 \alpha_c &= \mathbf{0.458502} \pm 0.0003733 \quad (0.08142\%).
 \end{aligned} \tag{7.40}$$

In comparison to the values from Eq. (6.4) an adequate accordance regarding the results for the critical coupling are provided. In Fig. 26 one can clearly see that the differences between the values for Basis 1 and Basis 2 increase for coupling constants closer to the critical coupling. Here the extrapolation becomes more difficult. Furthermore, for reliable results on the new lattice the calculation was executed up to much higher values of N based on the larger Brioullin zone. In the results represented here we solved the Dyson-Schwinger equation (5.12) from $N = 360$ until $N = 5625$ in steps of about 360 (due to section 5.4 the exact value is based on an optimization regarding prime factorization). With the development of an effective calculation scheme a lot of runtime can be saved and the whole calculation can be executed for a much higher number of lattice points. Now the calculations are not restricted due to runtime problems anymore but to the size of our main memory. So the program has to be additionally optimized in regard to the necessary memory.

The results are represented in Fig. 27 in detail. As expected, we can observe the same effects as in the last section. With higher numbers of lattice points N a better description of the Miransky-type scaling behaviour can be reached.

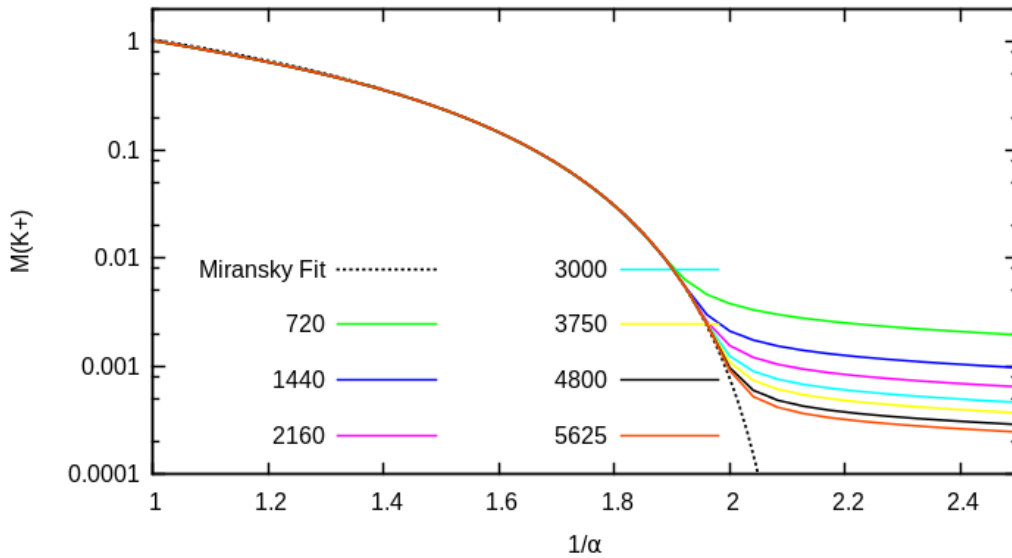


Figure 27: The order parameter for the semimetal-insulator phase transition ($M(K+)$) is plotted against the reciprocal of α for different values of N . The Miransky-Fit from Fig. 26 is also shown for a better comparison.

Taking the difficulties of the extrapolation into account and considering the fact that the results do not rely on the real errors of the solution of the DSE's (as explained in section 5.3) a good agreement of the results from the different BZ's can be found.

7.4. Renormalization of the Structure Function

With the new method at hand, now the Fermi-velocity renormalization should be considered. As already explained, the structure function (Eq. (5.13)) is then dynamically included in the evaluation procedure in every iteration step.

The calculation can still be executed within the chiral limit (setting $\mu_3 = 0$).

At some point it might be reasonable to introduce a small symmetry breaking mass term to receive a stable iteration away from the trivial solution. For that reason we also tried to implement a mass term given by $\mu_3 \sim 1/N$, that ansatz avoids an additional extrapolation to zero masses, so we achieve a simultaneous extrapolation to the chiral limit while extrapolating to an infinite volume ($N \rightarrow \infty$). The infinite volume extrapolation has been done analogically to the second order extrapolation described in section 6.1. That technique worked pretty well and delivers the same results as obtained by the direct calculation with $\mu_3 = 0$ within the tolerated errors. But of cause the finite volume behaviour itself differs because of the introduced mass term depending on N . Consequently the extrapolation to an infinite volume seems to be more complicated.

So for simplicity the symmetry breaking mass term was again set to zero. Here a similar finite-volume behaviour as in the last sections can be observed, although the iteration of the structure function has been included. For higher values of the coupling constant away from the phase transition again the quadratic fit from Eq. (6.2) can be applied without problems (see Fig. 28).

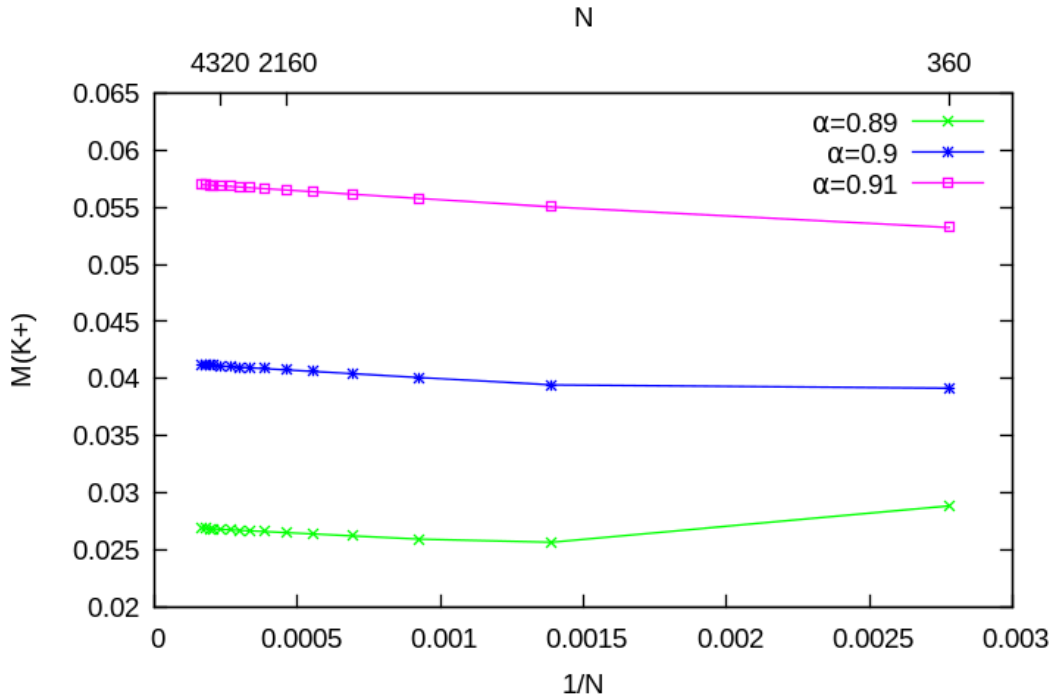


Figure 28: The energy gap at the Dirac point is plotted against the reciprocal value of N . The development of a minimum can be observed.

That quickly changes in the lower coupling regime, analogically to the mass renormalization without Fermi-velocity renormalization a minimum evolves. Data points that are computed for a number of lattice points N below the minimum has to be rejected. On that way the quality of the critical coupling extraction again directly depends on the number of lattice points that can be reached. In Fig. 29 one can see that reliable extrapolations for values below $\alpha = 0.88$ cannot be obtained for the applied region of lattice points.

The results were obtained for a number of lattice points, starting with $N = 360$ until $N = 6000$ in steps of about 360.

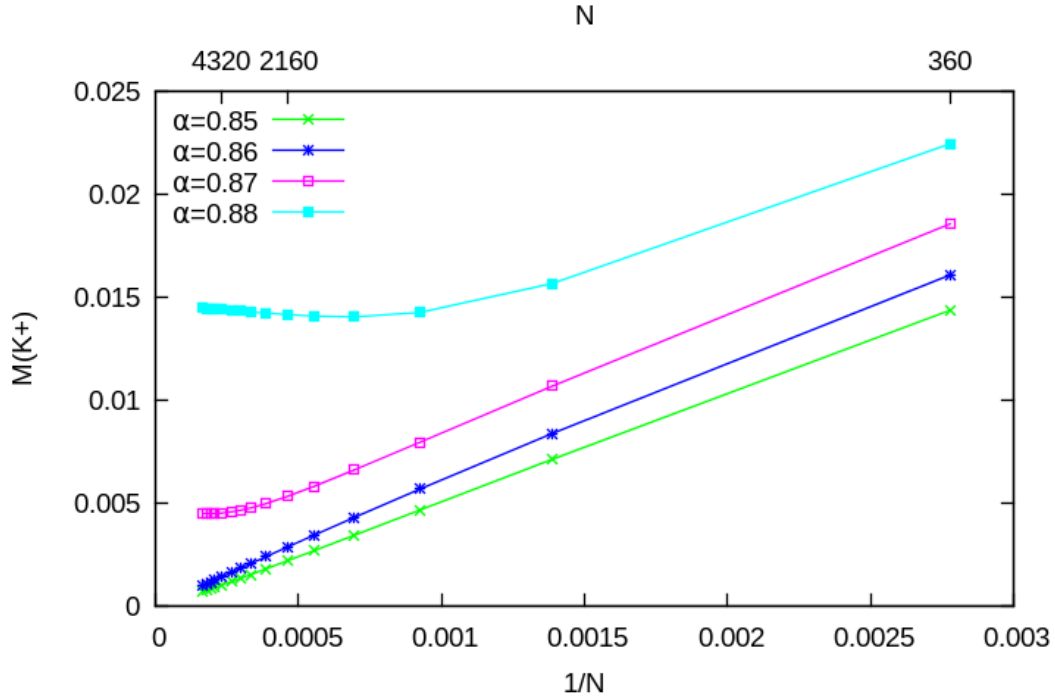


Figure 29: The energy gap at the Dirac point is plotted against the reciprocal value of N for coupling values near the critical coupling.

Now the extrapolated results should be investigated and the location of the phase transition should be identified. For that again a Miransky-Fit has been used to determine the critical coupling, represented in Fig. 30.

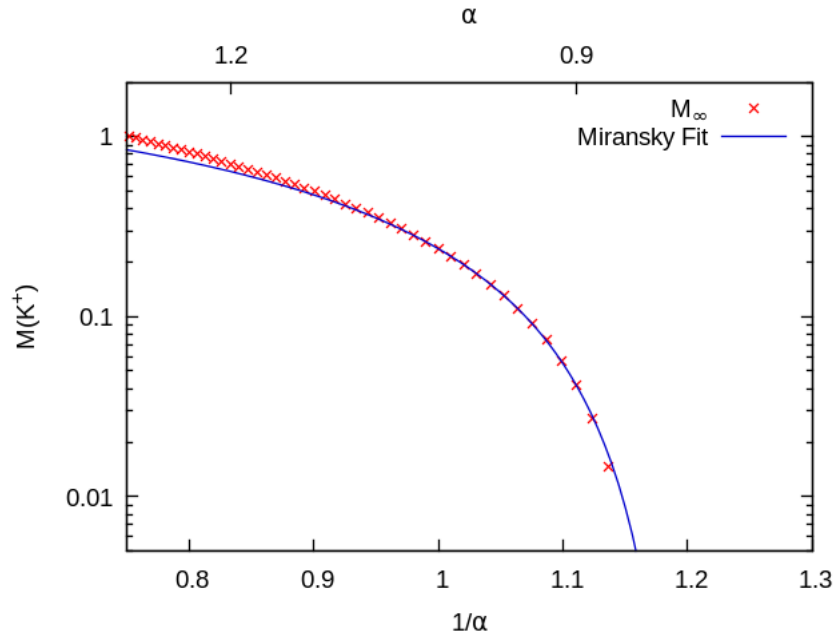


Figure 30: The extrapolated data has been fitted to the function 6.3 identifying a phase transition of Miransky-type.

At the regime near the phase transition, the function from Eq. (6.3) nicely fits the extrapolated data points. Away from the critical coupling the data points were not reproduced very well, but of course we only expect the Miransky-type behaviour to be valid near the critical coupling. For couplings that are large enough (in the symmetry broken regime) one can always find a point where the expected scaling behaviour is not valid anymore.

The similar behaviour can be deduced from Fig. 31.

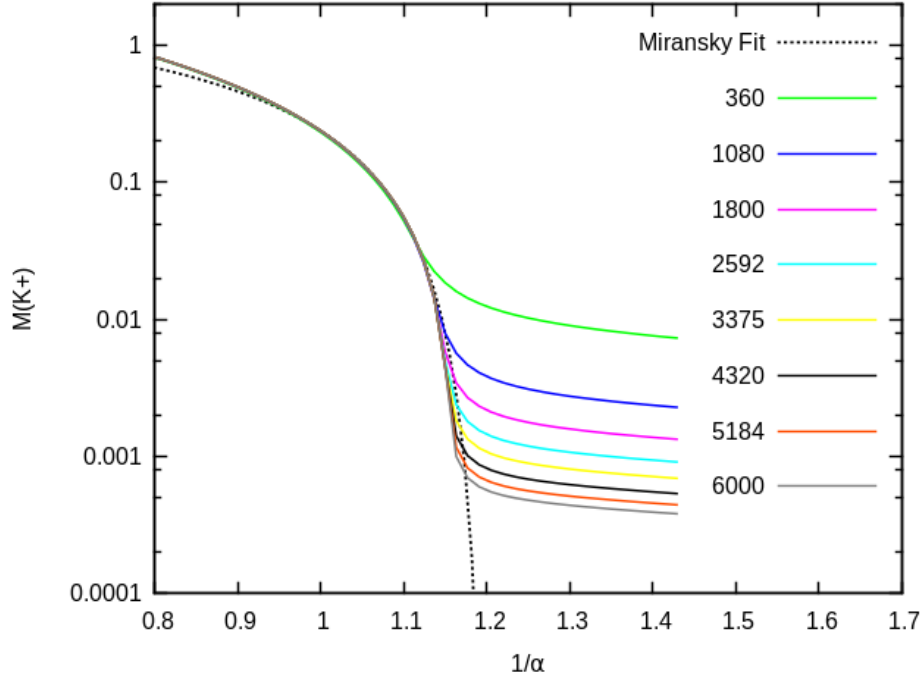


Figure 31: The energy gap at the Dirac point is plotted against the reciprocal value of α for different sizes of lattice points.

From the described fit, the following fit-parameters were obtained

$$\begin{aligned} a &= 12.2552 \pm 0.9661 \quad (7.883\%), \\ b &= -1.81546 \pm 0.04935 \quad (2.718\%), \\ \alpha_c &= \mathbf{0.824664} \pm 0.002075 \quad (0.2516\%). \end{aligned} \tag{7.41}$$

As one would expect, a larger coupling constant as in the previous approximation where Fermi-velocity renormalization has been neglected was extracted. This is due to the change of the Fermi-velocity renormalization that lowers the effective coupling. This result of $\alpha_c \approx 0.83$ can be directly compared with the results obtained within the Dirac-cone approximation for a zero vacuum polarization ($\Pi(p) = 0$). In Ref. [15] they found a critical coupling of about $\alpha_c \approx 1.22$. This difference can be explained with the Dyson-Schwinger equations itself, in contrast to Eq. (5.12) (for the mass renormalization) the equation for the Fermi-velocity renormalization (Eq. (5.13)) is more sensitive to higher momenta. This is explained in Appendix C in detail and gives rise to the overestimation of the influence of the Fermi-velocity renormalization in the Dirac-cone approximation.

In the following the reason for the increased critical coupling and the structure of the Fermi-velocity renormalization should be investigated. For that the energy dispersion is again plotted along the high symmetry points for a couple values of α represented in Fig. 32.

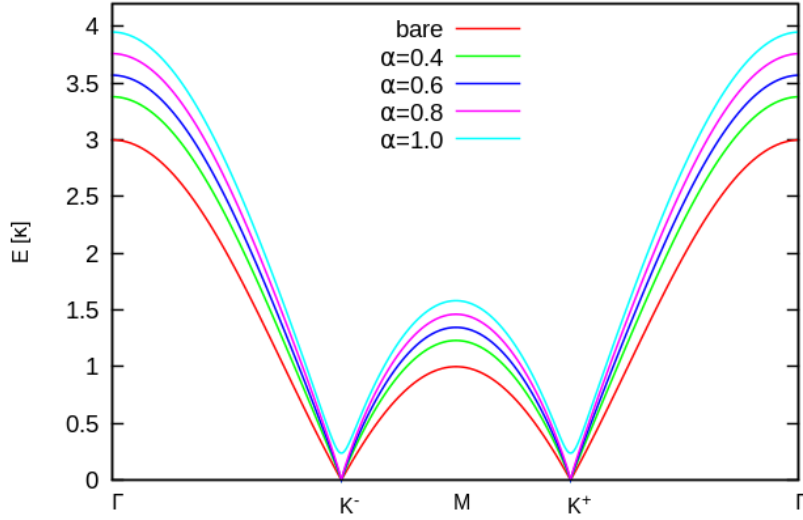


Figure 32: The energy in units of the hopping parameter κ is illustrated along the high symmetry points for different values of α . For a better comparison also the undressed structure function (bare $\alpha = 0$) is shown.

In comparison to Fig. 32 one cannot only see an effective shift (caused by the mass renormalization) of the energy dispersion for coupling values above the critical coupling, one can also observe an enormous change in the form of the dispersion relation. Especially, the slope near the Dirac points identifies the Fermi-velocity as pointed out in section 2.2 (see Eq. 2.15). Here, an energy gap for $\alpha = 1.0$ can be clearly observed but the structural changes can even be observed for much smaller coupling values.

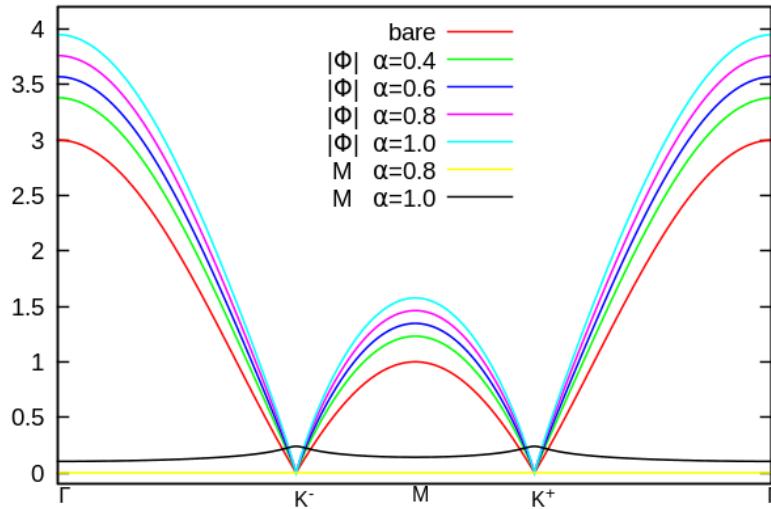


Figure 33: The several parts of the energy function $E = \sqrt{|\Phi|^2 + M^2}$ are plotted along the high symmetry points. The mass contribution for the plotted coupling constants smaller than $\alpha = 1.0$ are nearly zero.

In Fig. 33 also the two contributions of the energy dispersion ($M, |\Phi|$) are plotted separately (see Eq. (6.7)). Of course the mass renormalization cannot be observed for coupling constants below the critical coupling. For $\alpha = 1$ a mass renormalization was obtained that clearly differs from zero. Furthermore it can be observed that the mass renormalization has the biggest effect on the energy dispersion around the Dirac points. A comparison of Fig. 32 and Fig. 33 shows that e.g. in vicinity of the Γ -point the mass renormalization has roughly no influence on the energy dispersion.

Within the Dirac-cone approximation one would expect a logarithmic behaviour of the Fermi-velocity renormalization around the Dirac-points. Here the corresponding Fermi-velocity renormalization can be calculated analytically (see Appendix C). This effect cannot be observed in our calculations.

For completeness we again want to have a look on the three dimensional representations to be sure that we have found a meaningful way of representation by only plotting along the high symmetry points. For that the energy-momentum relation has been plotted in the broken phase for $\alpha = 1.0$ (Fig. 34).

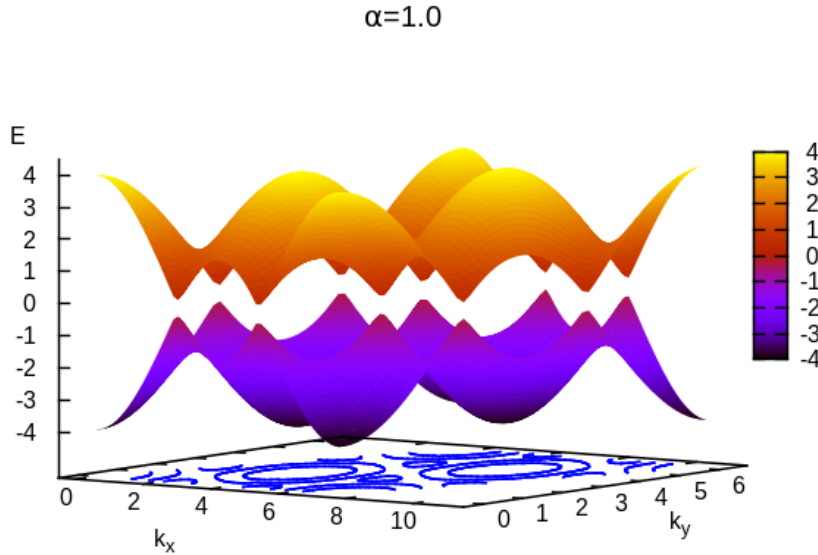


Figure 34: The energy dispersion is shown for the BZ (Basis 2) in the symmetry broken phase for $\alpha = 1.0$. The energy is given in units of the hopping parameter κ .

On the three times larger Brioullin zone (compare with Fig. 17) there are now obviously more than only two Dirac points. Plotting along the high symmetry points means plotting along one of the basis vectors in case of Basis 2. This can better be observed in the contour plot of Fig. 35. This plots has been made for a qualitative understanding for $N = 900$.

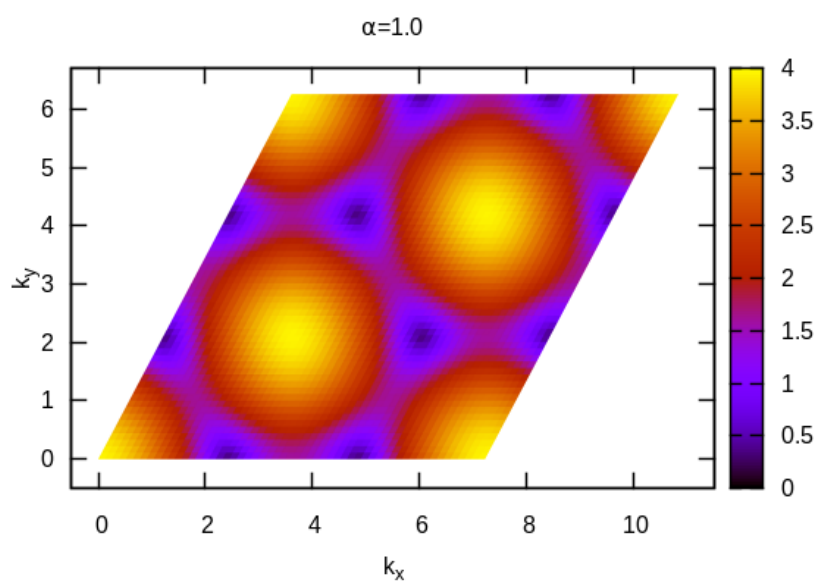


Figure 35: Fig. 34 has been converted into a contour plot, where the structure of the BZ can be clearly observed.

8. Inclusion of Screening Effects

8.1. Partially Screened Potential

In order to obtain a more realistic potential, especially the on-site interaction term has to be fixed to a reliable value. Until now this term has been calculated from a summation of all interaction terms in momentum space. It already turns out that this on-site part of the interaction has a crucial influence on the whole calculation, which is evident from the meaning of a local repulsion term and the fact that we would naively find a singularity for zero distances in the Coulomb potential.

In Ref. [11] the Coulomb interaction strength has been investigated on the basis of a constrained random phase approximation (cRPA). Within this approximation the on-site interaction term U_{00} , the nearest-neighbour interaction term U_{01} , the next-nearest-neighbour interaction term U_{02} and the third-nearest-neighbour interaction U_{03} has been determined. In this model the screening effects from the high-energy σ -bands play an important role, but also screening from lower orbitals was considered. Screening effects arising from the p_z -electrons themselves are not contained due to avoid double counting. These effects should be taken into account with help of a momentum dependent screening function (Lindhard screening), analogically to a vacuum polarization function in QED_3 [16, 15].

The values, worked out in Ref. [11] are summarized in the following table.

U_{00}	U_{01}	U_{02}	U_{03}
9.3 eV	5.5 eV	4.1 eV	3.6 eV

Table 1: The Coulomb interaction strength for $r \leq 2a$ is given, taken from Ref. [11] where a cRPA approach has been applied.

For the long-wavelength part of the potential, a very good agreement with a quite simple approximation of a thin dielectric film with dielectric function $\epsilon(\vec{k})$ was found [11].

The corresponding electrostatic potential was elaborated in Ref. [35] and adopted to the situation of free standing graphene in Ref. [11]. Here a thin dielectric film with a small thickness d , surrounded by air was assumed. The screening of charge carriers in the middle of the film, representing the graphene sheet, becomes negligible in the long-wavelegh limit ($\epsilon(k) \rightarrow 1$ for $k \rightarrow 0$), as it should be for any twodimensional material [11]. This delivers the following momentum dependence of the dielectric function

$$\epsilon(\vec{k}) = \frac{1}{\epsilon_1} \frac{\epsilon_1 + 1 + (\epsilon_1 - 1)e^{-kd}}{\epsilon_1 + 1 - (\epsilon_1 - 1)e^{-kd}} \quad (8.1)$$

with ϵ_1 being the appropriate dielectric constant and $k = |\vec{k}|$. This model was confirmed by the cRPA calculations with a very good fit presented in Ref. [11], providing $d = 2.8 \text{ \AA}$ and $\epsilon_1 = 2.4$. This model seems to be also conclusive with regard to the spatial extension of the p_z -orbitals which is of the order of d .

Furthermore in Ref. [11] it was pointed out that there is only a slight frequency dependence of the Coulomb interaction, this is why the static approach should give a good approximation for the considered energy regime. This nicely supports the basis of our theory.

In Ref. [9] an appropriate potential in position space combining the presented models has been developed. Here the potential was divided into three regimes, the regime for $r \leq 2a$ where the potential is given by the terms of table 1, the intermediate regime for distances between $2a$ and $120a$, here the potential is obtained with the help of the screening function (Eq. (8.1)) and

the regime for $r > 120a$. In the last regime the potential smoothly turns into an unscreened $1/r$ -potential. The unscreened potential in momentum space (see Eq. (4.8)) and the appropriate potential in position space (see Eq. (4.8)) were already presented in the previous chapter. The partially screened potential in position space in the intermediate regime is then given by

$$\tilde{V}(\vec{r}) = \int_{\mathbb{R}^2} \frac{d^2k}{(2\pi)^2} V(\vec{k}) \epsilon^{-1}(\vec{k}) e^{-i\vec{k}\vec{r}}. \quad (8.2)$$

The intermediate potential was additionally divided into separate regions and fitted to an exponential function:

$$V(r) = \begin{cases} V_{00}, V_{01}, V_{02}, V_{03}, & r \leq 2a \\ \frac{1}{2\pi} \left(\frac{m_0}{(m_1 r)^\gamma} e^{-m_2 r} + m_3 \right), & r > 2a \end{cases} \quad (8.3)$$

where the values for V_{0i} are simply given by U_{0i} via $V_{0i} = U_{0i}/2\pi\alpha$, with $\alpha \approx 1/137$ being the fine-structure constant, to directly apply our conventions to that of Ref. [9].

The fit parameters for the mentioned regions are shown in table 2 and were exactly taken from Ref. [9].

	m_0 [eV]	γ	m_2 [eV]	m_3 [eV]
$8a \geq r > 2a$	9.0380311	0.632469	144.354	62.41496
$30a \geq r > 8a$	2.0561977	0.862664	27.8362	15.29088
$120a \geq r > 30a$	1.03347891	0.990975	0.0	-0.134502
$r > 120a$	1.0	1.0	0.0	0.0

Table 2: Represented are the fit parameters for the intermediate region fitted to the exponential function (Eq. (8.3)), taken from Ref. [9].

The parameter m_1 is given by $m_1 = 1$ eV in every region, with the interatomic distance $a = 1.42$ Å and $10^{-7} m = 0.506$ eV⁻¹; the units of eV can be simply transferred into the unit system used until now, where the potential in position space should be given in units of $1/a$ to obtain the DSE's (Eq. (5.15)) in units of κ . The potential that now has to be constructed in position space is shown in Fig. 36 in comparison to the potential described in the last chapter (see Eq. (7.31)) along the index i indicating the y-axis in position space. A detailed comparison can be found in [9].

Also in the three dimensional representation (Fig. 37) a slightly change of the potential in momentum space can be observed. This change has a large effect as it is shown in the next section.

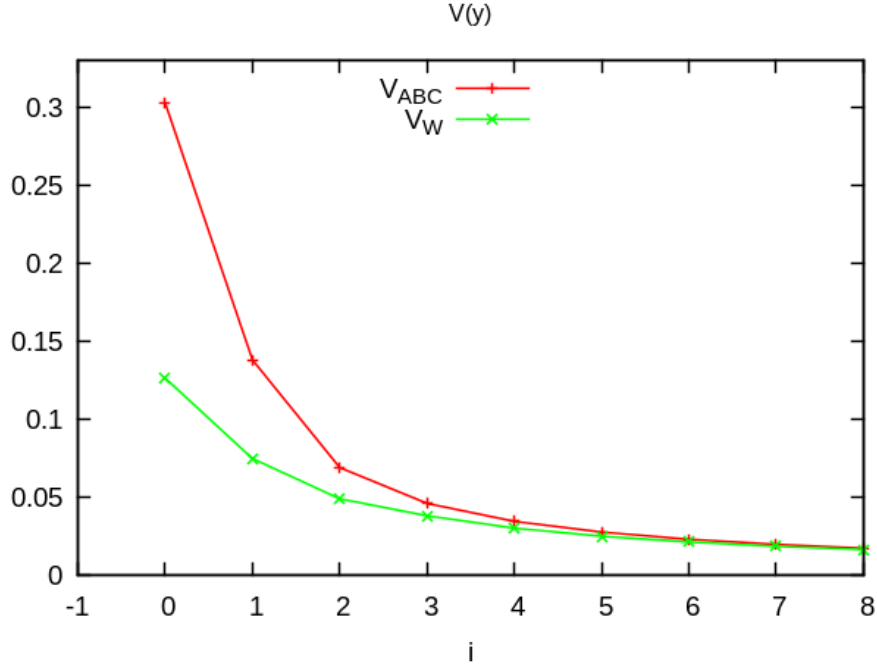


Figure 36: For comparison the Coulomb potential (V_{ABC}) from Eq. (7.31) is plotted as well as the partially screened potential from Eq. (8.3) denoted by V_W . One can observe that V_W smoothly changes into an unscreened Coulomb potential (V_{ABC}).

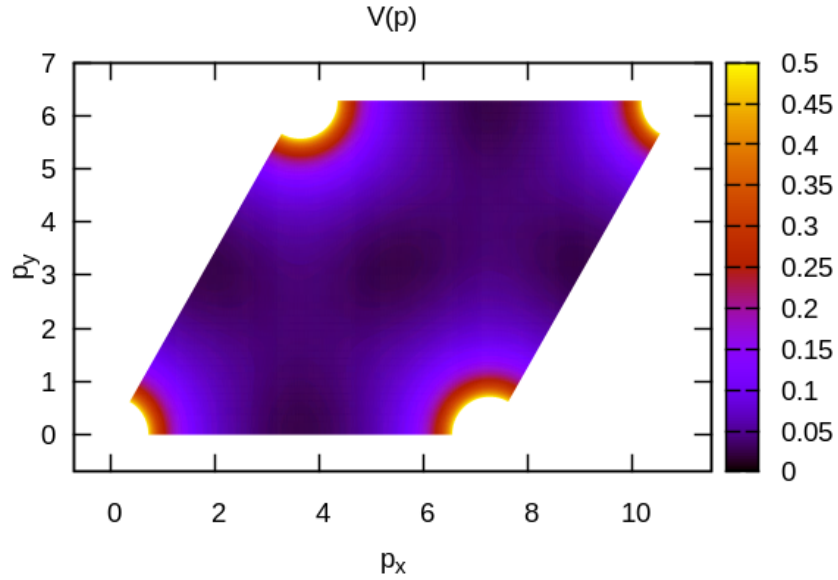


Figure 37: The obtained potential (8.3) is plotted on the complete Brillouin zone for comparison to Fig. 24.

8.2. Renormalization

The described potential has been implemented in the calculation and again the DSE'S has been solved. The finite volume behaviour here was slightly different. For the regime away from the critical coupling perfect horizontals (see Fig. 38) were obtained instead of sloped lines, here very good estimations can be already made for $N = 360$. Of course the situation is rather different in the near-critical regime, otherwise it would be possible to extract the critical coupling with much less lattice points.

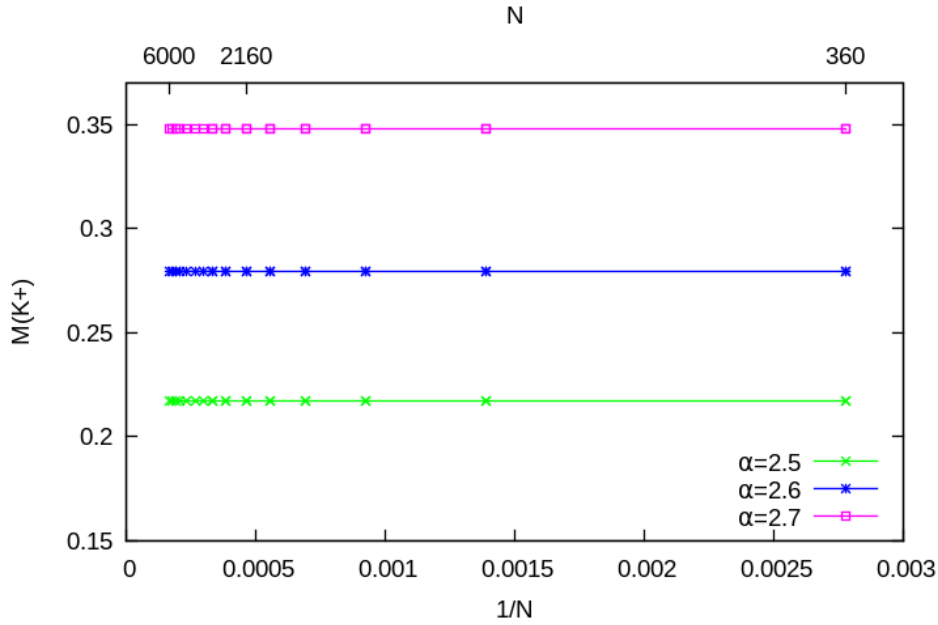


Figure 38: The energy gap at the Dirac point is plotted against the reciprocal of N . For coupling constants away from the critical coupling there is almost no change with the volume.

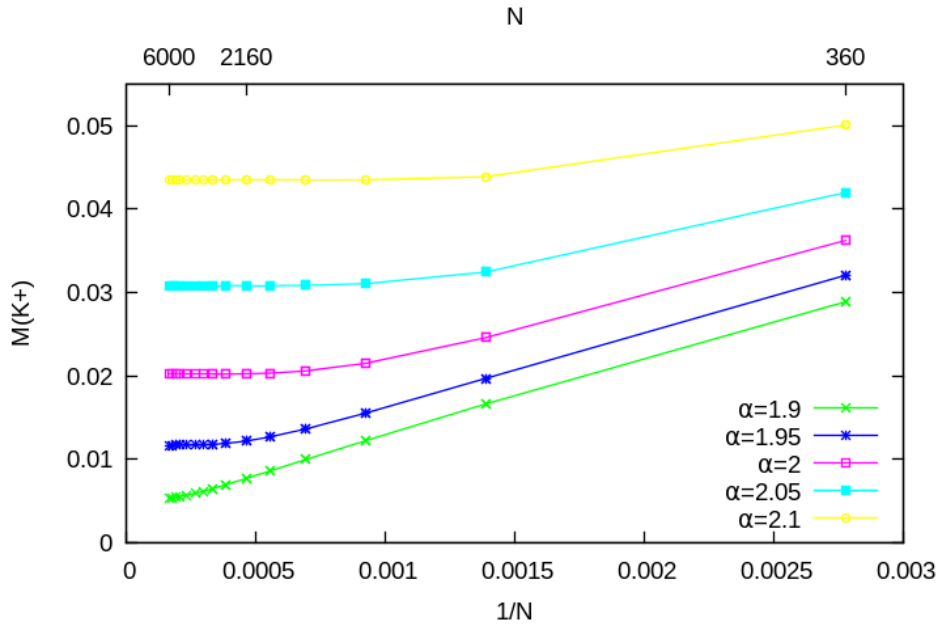


Figure 39: $M(K+)$ is plotted against the reciprocal number of lattice points for coupling constants in the symmetry broken phase (not close to the critical coupling).

For lower coupling constants the constant behaviour can only be found for a much larger number of lattice points (see Fig. 39). This plateau region has to be reached to make a meaningful extrapolation. For the other values of α one cannot make any statement about the energy gap for $N \rightarrow \infty$. As it is shown exemplary for $\alpha = 1.9$ in Fig. 39.

In Fig. 40 the extrapolated values are again fitted to the function from Eq. (6.3) providing a scaling behaviour of Miransky type. The result seems to be qualitatively similar to the fit of Fig. 30.

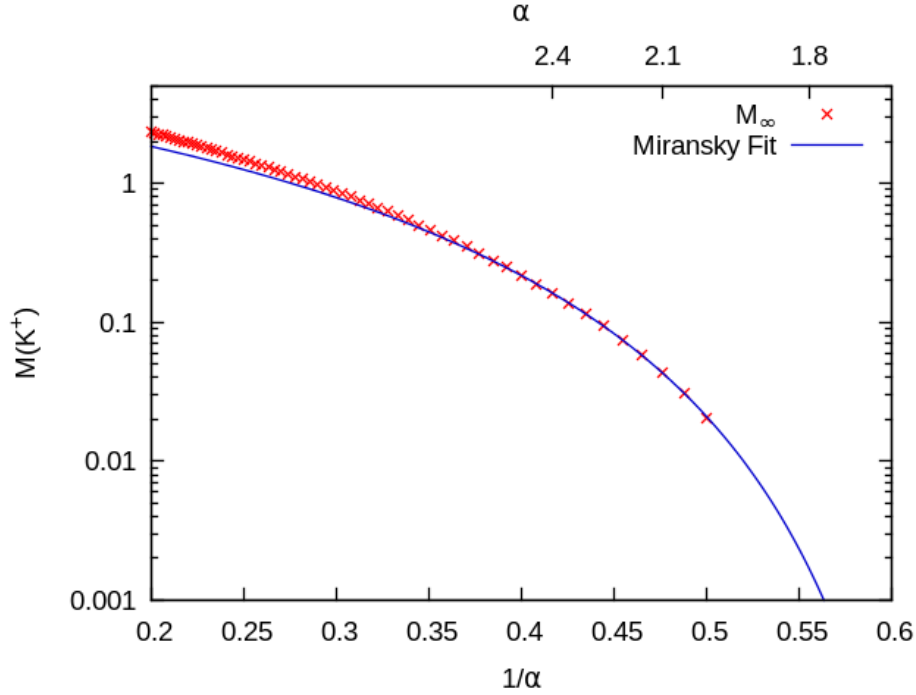


Figure 40: The extrapolated data has been fitted to the function from Eq. 6.3 identifying a phase transition of Miransky-type.

The least-square fit delivers the following fit parameters

$$\begin{aligned}
 a &= 3268.77 \pm 873.9 \quad (26.74\%), \\
 b &= -5.1119 \pm 0.2145 \quad (4.196\%), \\
 \alpha_c &= \mathbf{1.46486} \pm 0.0169 \quad (1.154\%).
 \end{aligned} \tag{8.4}$$

As anticipated a much higher value for the critical coupling was reached, since also the screening effects lower the effective coupling. But the critical coupling is still well below the limit of the physically realizable region at about $\alpha \approx 2.2$.

In Fig. 41 and Fig. 42 again the energy dispersion and the several parts of the energy dispersion are plotted along the symmetry points of the Brioullin zone (in this zone realized by plotting against k_x or k_y). One can qualitatively observe the same effects as in the case where screening is neglected but only realized at higher couplings α .

Until now the electronic screening caused by the p_z electrons itself were not considered (taking the Lindhard screening into account). This point might provide an access to critical couplings above $\alpha \approx 2.2$ and therefore explain the experimental finding that graphene stays in the semimetal phase [10].

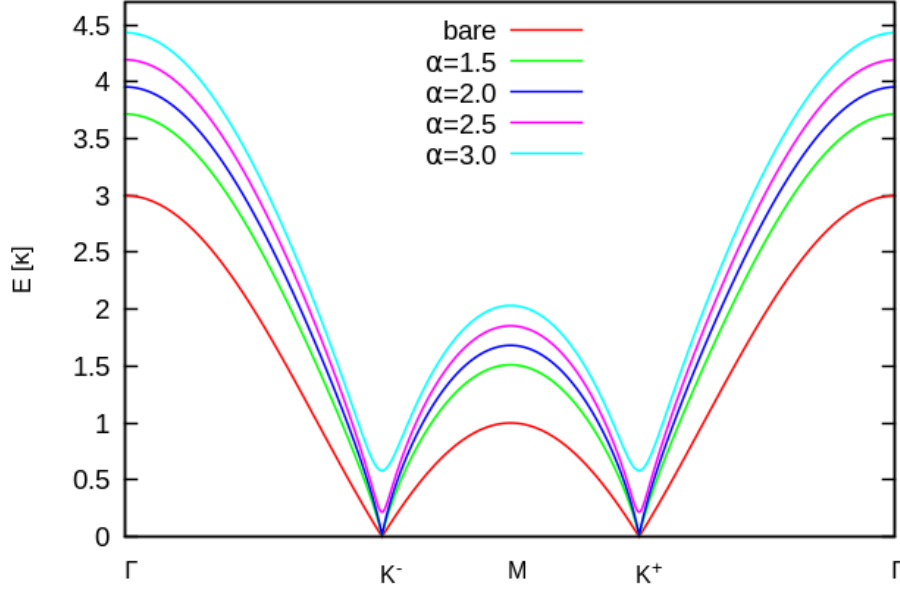


Figure 41: The energy function has been plotted along the high symmetry points for different values of α . The bare energy function is also plotted for a better comparison.

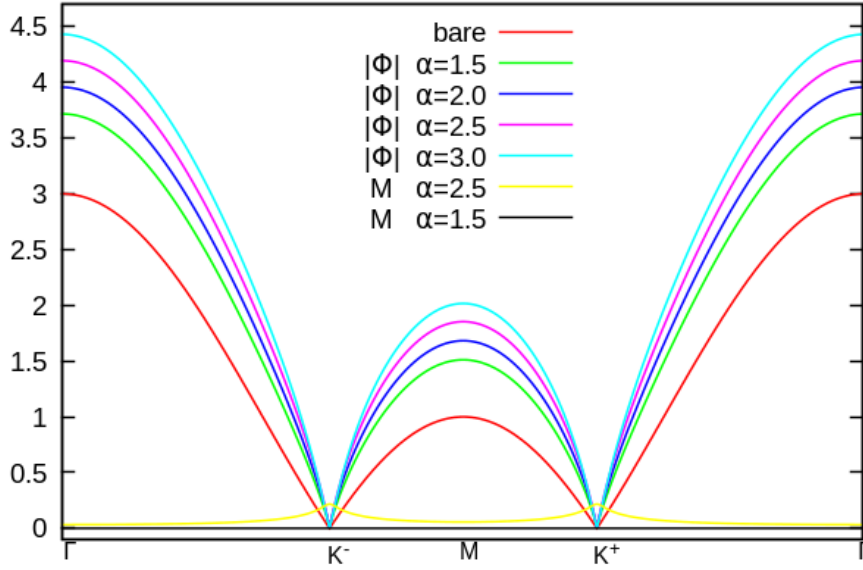


Figure 42: The single parts of the energy dispersion (M , $|\Phi|$) are plotted along the symmetry points of the Brillouin zone. For $\alpha = 2.5$ one can clearly observe a mass gap. The structure function already changes for much smaller values of α . But in comparison to Fig. 33 also the change of the Fermi-velocity seems to be suppressed by the screening effects, as one would expect.

9. Conclusion and Outlook

It was shown that the analytically obtained critical coupling can be reproduced with an adequate accuracy within the developed computation scheme in the framework of Dyson-Schwinger equations by neglecting the Fermi-velocity renormalization. Moreover, a clear indication of the reliability of the extrapolation procedure to an infinite number of lattice points can be obtained. Also the typical scaling behaviour which was already verified in Ref. [15] could be confirmed for the first time on the hexagonal lattice.

In a next step the renormalization of the structure function was included. For that it was necessary to change to a larger Brillouin zone where a higher resolution in position space can be reached. Here the elaborated procedure could also be validated on the basis of the analytical value for the critical coupling (Eq. (6.5)), so the renormalization of the Fermi-velocity was included.

With the implementation of a more realistic potential (partially screened), based on the interaction terms up to third-nearest neighbour interaction determined by a constrained Random Phase Approximation (cRPA), a critical coupling of about $\alpha \approx 1.5$ was extracted. By the inclusion of the described potential (see Eq. (8.3)) we are coming closer to the setup of the HMC simulations from Ref. [9]. If the Lindhard-function is additionally taken into account it would be in accordance with HMC calculations if the critical coupling of $\alpha \approx 2.2$ (marking the physical limit of a realizable semimetal-insulator phase for suspended graphene) is then passed. Within this setup (including the Lindhard-function) the same situation as used in the HMC studies would be built, excepting the static approximation that was made in this work. So, by taking a nonzero vacuum polarization into account the static approximation can be validated with the help of a comparison to the results of the HMC calculations [9].

This would be the next step in order to unify the formalism presented in this work with already existing studies. As already worked out the described procedure has a high potential to reach beyond the Dirac-cone approximation but it is also able to explore areas that are not accessible via HMC simulations.

In this work the symmetry breaking (causing the semimetal-insulator phase transition) is only induced by an asymmetry of the charge density on the two sublattices (see Hamiltonian (3.1)). This alternating charge density (generating a Charge Density Wave (CDW) state) breaks the chiral symmetry down to: $U(4) \rightarrow U(2) \times U(2)$. The same pattern of symmetry breaking can be caused by an asymmetry regarding the spin density of the system [36, 37] (generating a Spin Density Wave (SDW) state). These two possible realizations of the same phase transition can be distinguished by their different vacuum alignments [6, 38]. In terms of the Dirac-cone approximation where a continuous rotational invariance is a consequence of the used assumptions, this vacuum alignments cannot be separated. Even in the case of Monte-Carlo methods the necessary mass term that turns the system to the symmetry broken phase causes a sign problem [39].

Furthermore, it is supposed that there can be another electronic phase that can be realized in graphene which is similar to a high-temperature superconductor phase (d-wave superconductor) which would be of enormous industrial interest. At the introduced M-points (see Fig. 4), being van-Hove singularities from a solid-state physical point of view (where the density of states diverges), the electron conduction changes to a hole conduction. So the control parameter to generate this kind of phase transition would be the chemical potential (regulating the relation between electrons and holes). If the chemical potential passes the van-Hove singularity a so called Lifshitz transition [40] is expected. Here the region of relativistic excitations is separated from the region of non-relativistic excitations.

Also the investigation of this phase transition would be possible within the presented framework. Considering the Lifshitz transition the HMC calculations are as well confronted with a sign problem. Moreover with the presented Dyson-Schwinger method it is possible to reach much higher ranges of volumina and one can therefore provide a promising investigation of the finite volume behaviour and scaling effects themselves. Finally one has to think about the physical realization of the phase transition that might be excluded experimentally as well as theoretically (e.g. in the case of the semimetal-insulator phase). But graphene can be modified mechanically, chemically or for example by an external influence (e.g. a magnetic field). So one has to examine the different possibilities and decide with which modification the system can be turned into the broken phase most efficiently. This work is regarded as the basis for the described widely ranged possibilities of an application of the developed methods.

A. Tight-Binding Model

Three of the four valence electrons of a single carbon atom form strong covalent σ -bonds in terms of an sp^2 -hybridization of the atomic orbitals [6]. Based on the idea that these electrons, producing the honeycomb lattice, are not essentially contributing to the electronic properties of graphene, we only consider the remaining electron of the p_z -orbital. These electron orbitals are arranged perpendicular to the graphene plane forming a π -orbital with weak overlap and could be treated in a tight-binding approach.

The ansatz of the wavefunction ψ for the graphene sheet in the tight-binding model is generally based on a linear combination of atomic orbitals (LCAO). In the case of graphene this reduces to the wavefunction of the $2p_z$ -orbital $\chi(\vec{r})$ that satisfies the Schrödinger equation for a single carbon atom. Moreover the wavefunction in the tight-binding approximation has to agree with Bloch's theorem in terms of periodicity [41]. That leads to

$$\psi = \alpha \varphi_A + \beta \varphi_B \quad (\text{A.1})$$

with

$$\begin{aligned} \varphi_A &= \sum_A e^{i\vec{k}\vec{r}_A} \chi(\vec{r} - \vec{r}_A) \\ \varphi_B &= \sum_B e^{i\vec{k}\vec{r}_B} \chi(\vec{r} - \vec{r}_B) \end{aligned}$$

for the two-component basis with \vec{r}_A describing the position vectors of the sublattice A and \vec{r}_B respectively. So, for now the Schrödinger equation for an electron in the graphene sheet on the position \vec{R} should be considered:

$$H_{\vec{R}} = \frac{p_{\vec{R}}^2}{2m} + \sum_{\vec{R}'} V(\vec{r} - \vec{R}') = H_{at, \vec{R}} + \sum_{\vec{R}' \neq \vec{R}} V(\vec{r} - \vec{R}') = H_{at, \vec{R}} + \Delta V_{\vec{R}}(\vec{r}). \quad (\text{A.2})$$

By multiplying the Schrödinger equation with φ_A and φ_B respectively and integrating over the crystal area as defined by the variational principle (here denoted by $\int d\tau$), one can solve the system of equations for their Eigenvalues E_{\pm} .

Assuming, within the meaning of tight-binding, that the overlap between adjacent wavefunctions is zero

$$\int \chi^*(\vec{r} - \vec{r}_A) \chi(\vec{r} - \vec{r}_B) d\tau = 0, \quad (\text{A.3})$$

leads to the Eigenvalue problem [1]

$$\begin{pmatrix} H_{11} & H_{12} \\ H_{21} & H_{22} \end{pmatrix} \begin{pmatrix} \alpha \\ \beta \end{pmatrix} = E \begin{pmatrix} \alpha \\ \beta \end{pmatrix}. \quad (\text{A.4})$$

Since $H_{11} = H_{22}$ and $H_{12} = H_{21}$ for reasons of symmetry (\mathcal{PT} -symmetry [6]) we obtain

$$E = H_{11} \pm \|H_{12}\| \quad (\text{A.5})$$

for the energy states of the tightly bonded graphene sheet.

The single entries of the matrix are given by the following expressions [1]:

$$H_{11} = \frac{1}{N} \sum_{A, A'} e^{-i\vec{k}(\vec{r}_A - \vec{r}_{A'})} \int \chi^*(\vec{r} - \vec{r}_A) H \chi(\vec{r} - \vec{r}_{A'}), \quad (\text{A.6})$$

$$H_{12} = \frac{1}{N} \sum_{A,B} e^{-i\vec{k}(\vec{r}_A - \vec{r}_B)} \int \chi^*(\vec{r} - \vec{r}_A) H \chi(\vec{r} - \vec{r}_B), \quad (\text{A.7})$$

where N is the number of unit cells in the crystal.

For now, the six nearest neighbours of the sublattice A (ρ_n) and the three nearest neighbours of the sublattice B (δ_n) should be taken into account.

With the ground state of a single carbon atom (which only appears in H_{11})

$$E_0 = \int \chi^*(\vec{r}) H_{at,\vec{R}} \chi(\vec{r}) d\tau \quad (\text{A.8})$$

and the hopping parameters for the respective sublattices

$$\kappa' = - \int \chi(\vec{r} - \vec{\rho}_n) \Delta V_{\vec{R}}(\vec{r}) \chi(\vec{r}) d\tau \quad (\text{A.9})$$

$$\kappa = - \int \chi(\vec{r} - \vec{\delta}_n) \Delta V_{\vec{R}}(\vec{r}) \chi(\vec{r}) d\tau \quad (\text{A.10})$$

the following dispersion relation [4] is obtained:

$$E_{\pm}(\vec{k}) = E_0 \pm \kappa \sqrt{\phi^2(\vec{k})} - \kappa' (\phi^2(\vec{k}) - 3) \quad (\text{A.11})$$

with the structure function

$$\phi(\vec{k}) = \sum_{n=1}^3 e^{i\vec{k}\vec{\delta}_n} = \frac{-b_1(\vec{k}) + ib_2(\vec{k})}{\kappa} \quad (\text{A.12})$$

and

$$|\phi(\vec{k})|^2 = 3 + 2 \cos(\sqrt{3}k_y a) + 4 \cos\left(\frac{\sqrt{3}}{2}k_y a\right) \cos\left(\frac{3}{2}k_x a\right). \quad (\text{A.13})$$

For simplification we will only take the nearest neighbour interaction into account ($\kappa' = 0$) but should keep in mind that the inclusion of the next nearest neighbour potentials would lead to a break of particle hole symmetry (see Eq. (A.11)).

By the introduction of the common notation in second quantization, the wavefunction is given by

$$\psi = \sum_A \alpha e^{i\vec{k}\vec{r}_A} a_i^\dagger |0\rangle + \sum_B \beta e^{i\vec{k}\vec{r}_B} b_i^\dagger |0\rangle \quad (\text{A.14})$$

where a^\dagger and b^\dagger are the abstract creation operators for electrons of the sublattice A and B respectively. They have to satisfy the usual anticommutator relations for fermions with the associated annihilation operators a and b :

$$\{c_i, c_j\} = \{c_i^\dagger, c_j^\dagger\} = 0 \quad \{c_i, c_j^\dagger\} = \delta_{ij} \quad \text{with} \quad c \in \{a, b\}. \quad (\text{A.15})$$

With that it can be easily recomputed that the Hamilton operator in second quantization

$$H = -\kappa \sum_{\langle i,j \rangle} a_i^\dagger b_j + b_j^\dagger a_i \quad (\text{A.16})$$

leads to the same Eigenvalue problem [41]:

$$\begin{pmatrix} 0 & -\kappa\phi(\vec{k}) \\ -\kappa\phi^*(\vec{k}) & 0 \end{pmatrix} \begin{pmatrix} \alpha \\ \beta \end{pmatrix} = E \begin{pmatrix} \alpha \\ \beta \end{pmatrix}, \quad (\text{A.17})$$

where the energy E_0 is set to zero and the next nearest neighbour potentials are neglected ($\kappa' = 0$). The crucial information is again contained in the coordination between the lattice sites since the structure function depends on the momentum and therefore changes the energy-momentum relation.

B. Conventions and Relations

The free Hamilton operator from Eq. (3.1) has been constructed in the 2×2 dimensional sublattice space. Consequently the operators can be represented by the usual Pauli matrices

$$\sigma_1 = \begin{pmatrix} 0 & 1 \\ 1 & 0 \end{pmatrix} \quad \sigma_2 = \begin{pmatrix} 0 & -i \\ i & 0 \end{pmatrix} \quad \sigma_3 = \begin{pmatrix} 1 & 0 \\ 0 & -1 \end{pmatrix} \quad (\text{B.1})$$

indicating the sublattice space. To come closer to a quantum field theoretical representation of the fermion propagator the description by the following Dirac matrices is introduced:

$$\gamma_0 = \sigma_3, \quad \gamma_1 = \sigma_3 \sigma_1, \quad \gamma_2 = \sigma_3 \sigma_2, \quad (\text{B.2})$$

that are satisfying the Clifford algebra $\{\gamma_\mu, \gamma_\nu\} = 2g_{\mu\nu}$ with

$$g_{\mu\nu} = \begin{pmatrix} 1 & 0 & 0 \\ 0 & -1 & 0 \\ 0 & 0 & -1 \end{pmatrix} \quad (\text{B.3})$$

of the two-dimensional sublattice space belonging to the pseudospin degree of freedom. In matrix notation they are given by:

$$\gamma_0 = \begin{pmatrix} 1 & 0 \\ 0 & -1 \end{pmatrix}, \quad \gamma_1 = \begin{pmatrix} 0 & -1 \\ 1 & 0 \end{pmatrix}, \quad \gamma_2 = \begin{pmatrix} 0 & -i \\ -i & 0 \end{pmatrix}. \quad (\text{B.4})$$

B.1. Basis 1

Basis vectors in position space:

$$\vec{a}_1 = \frac{a}{2} \begin{pmatrix} \sqrt{3} \\ 3 \end{pmatrix}, \quad \vec{a}_2 = \frac{a}{2} \begin{pmatrix} \sqrt{3} \\ -3 \end{pmatrix}. \quad (\text{B.5})$$

Basis vectors in momentum space:

$$\vec{b}_1 = \frac{2\pi}{3a} \begin{pmatrix} \sqrt{3} \\ 1 \end{pmatrix}, \quad \vec{b}_2 = \frac{2\pi}{3a} \begin{pmatrix} \sqrt{3} \\ -1 \end{pmatrix}. \quad (\text{B.6})$$

Unit cell area in position space:

$$\mathcal{AZ} = |\vec{a}_1 \times \vec{a}_2| = \frac{3\sqrt{3}a^2}{2}. \quad (\text{B.7})$$

Area of the Brillouin zone:

$$\mathcal{BZ} = |\vec{b}_1 \times \vec{b}_2| = \frac{8\pi^2}{3\sqrt{3}a^2}. \quad (\text{B.8})$$

Next nearest neighbours:

$$\vec{\delta}_1 = \frac{\vec{a}_1 - \vec{a}_2}{3}, \quad \vec{\delta}_2 = \frac{\vec{a}_1 + 2\vec{a}_2}{3}, \quad \vec{\delta}_3 = -\frac{2\vec{a}_1 + \vec{a}_2}{3}. \quad (\text{B.9})$$

With the discretized momentum vector and position vector

$$\vec{k} = \frac{1}{N}(m \vec{b}_1 + n \vec{b}_2), \quad \vec{r} = i \vec{a}_1 + j \vec{a}_2, \quad (\text{B.10})$$

one finds the corresponding structure function:

$$\phi_{mn} = \sum_{n=1}^3 e^{i\vec{k}\delta_n} = e^{\frac{2\pi i}{3N}(m-n)} + e^{\frac{2\pi i}{3N}(m+2n)} + e^{\frac{-2\pi i}{3N}(2m+n)}. \quad (\text{B.11})$$

This leads to the following symmetries:

$$\phi_{mn} = \phi_{m+Nn+N}, \quad \phi_{mn} = \phi_{N-mN-n}^*, \quad \phi_{mn} = \phi_{nm}^*, \quad \rightarrow \quad \phi_{mn} = \phi_{N-mN-n}, \quad (\text{B.12})$$

but

$$\phi_{mn} \neq \phi_{m+Nn}, \quad \phi_{mn} \neq \phi_{mn+N}.$$

B.2. Basis 2

Basis vectors in position space:

$$\vec{a}_1 = a \begin{pmatrix} 0 \\ 1 \end{pmatrix}, \quad \vec{a}_2 = \frac{a}{2} \begin{pmatrix} \sqrt{3} \\ -1 \end{pmatrix}. \quad (\text{B.13})$$

Basis vectors in momentum space:

$$\vec{b}_1 = \frac{2\pi}{3a} \begin{pmatrix} \sqrt{3} \\ 3 \end{pmatrix}, \quad \vec{b}_2 = \frac{4\pi}{3a} \begin{pmatrix} \sqrt{3} \\ 0 \end{pmatrix}. \quad (\text{B.14})$$

Unit cell area in position space:

$$\mathcal{AZ} = |\vec{a}_1 \times \vec{a}_2| = \frac{\sqrt{3}a^2}{2}. \quad (\text{B.15})$$

Area of the Brillouin zone:

$$\mathcal{BZ} = |\vec{b}_1 \times \vec{b}_2| = \frac{8\pi^2}{\sqrt{3}a^2}. \quad (\text{B.16})$$

Next nearest neighbours:

$$\vec{\delta}_1 = \vec{a}_1, \quad \vec{\delta}_2 = \vec{a}_2, \quad \vec{\delta}_3 = -(\vec{a}_1 + \vec{a}_2). \quad (\text{B.17})$$

With the discretized momentum vector and position vector

$$\vec{k} = \frac{1}{N}(m \vec{b}_1 + n \vec{b}_2), \quad \vec{r} = i \vec{a}_1 + j \vec{a}_2, \quad (\text{B.18})$$

the corresponding structure function is obtained:

$$\phi_{mn} = \sum_{n=1}^3 e^{i\vec{k}\delta_n} = e^{\frac{2\pi i}{3N}m} + e^{\frac{2\pi i}{3N}n} + e^{\frac{-2\pi i}{3N}(m+n)}. \quad (\text{B.19})$$

This leads to the following symmetries:

$$\phi_{mn} = \phi_{m+Nn+N}, \quad \phi_{mn} = \phi_{N-mN-n}^*, \quad \phi_{mn} = \phi_{nm}, \quad (\text{B.20})$$

and

$$\phi_{mn} \neq \phi_{m+Nn}, \quad \phi_{mn} \neq \phi_{mn+N}.$$

C. Comparison to the Dirac-cone Approximation

The results that were obtained in the ansatz without low-energy approximation smoothly disagree with the results from calculations in the Dirac-cone approximation [15]. To understand the differences we just want to compare the solved Dyson-Schwinger equations in our truncation with the Dyson-Schwinger equations from the Dirac-cone approximation.

In the radial symmetric ansatz of the Dirac-cone approximation one gets the following Dyson-Schwinger equations for the mass renormalization function $\Delta(p)$ and the Fermi-velocity renormalization function $A(p)$ [15].

$$\Delta(p) = \alpha v_f \int \frac{d\omega d^2k}{(2\pi)^3} \frac{\Delta(k)}{\omega^2 + v_f^2 A^2(k) k^2 + \Delta^2(k)} [-4\pi i D_C(i\omega, \vec{p} - \vec{k})] \quad (C.1)$$

$$A(p) = 1 + \alpha v_f \int \frac{d\omega d^2k}{(2\pi)^3} \frac{\vec{p} \cdot \vec{k}}{p^2} \frac{A(k)}{\omega^2 + v_f^2 A^2(k) k^2 + \Delta^2(k)} [-4\pi i D_C(i\omega, \vec{p} - \vec{k})] \quad (C.2)$$

The Dyson-Schwinger equations shown in this work (deduced from a more general ansatz) can be written as

$$M(\vec{p}) = \mu_3 + \alpha v_f \int \frac{d\omega d^2k}{(2\pi)^3} \frac{M(\vec{k})}{\omega^2 + B_1^2(\vec{k}) + B_2^2(\vec{k}) + M^2(\vec{k})} [-4\pi i D_C(i\omega, \vec{p} - \vec{k})], \quad (C.3)$$

$$\vec{B}(\vec{p}) = \vec{b}(\vec{p}) + \alpha v_f \int \frac{d\omega d^2k}{(2\pi)^3} \frac{\vec{B}(\vec{k})}{\omega^2 + |\vec{B}(\vec{k})|^2 + M^2(\vec{k})} [-4\pi i D_C(i\omega, \vec{p} - \vec{k})]. \quad (C.4)$$

Here $\Phi(\vec{k}) = B_1(\vec{k}) - iB_2(\vec{k})$ is a complex function taking the renormalization of the whole band structure into account. By the following ansatz in terms of the Dirac-cone approximation, the Dyson-Schwinger equations can be converted into each other:

$$\vec{b}(\vec{p}) \rightarrow v_f \vec{q}, \quad \vec{B}(\vec{q}) \rightarrow v_f \vec{q} A(q). \quad (C.5)$$

In this Appendix bifurcation theory should be applied on the considered DSE's from Eq. (C.3) and Eq. (C.4) analogically to the investigation of Eq. (C.2) and Eq. (C.1) from Ref. [15]. Here an expansion in leading order of the mass renormalization function has been made ($\Delta(p) = M(\vec{p}) = 0$). This approach becomes exact at the critical point. The corresponding linearized equations within the low energy approximation are given by (see Ref. [15])

$$\Delta(p) = \frac{\alpha}{2\pi} \int d^2k \frac{1}{|\vec{p} - \vec{k}|} \frac{\Delta(k)}{k A(k)}, \quad (C.6)$$

$$A(p) = 1 + \frac{\alpha}{2\pi} \int d^2k \frac{\vec{p} \cdot \vec{k}}{p^2} \frac{1}{|\vec{p} - \vec{k}|}, \quad (C.7)$$

with the vacuum polarization being neglected. The second integral can be solved analytically and leads to the common logarithmic behaviour of the Fermi-velocity renormalization, that could not be recomputed in the framework of our approximation.

The linearized equations of the more general approach read

$$M(\vec{p}) = \frac{\alpha}{2\pi} \int d^2k \frac{1}{|\vec{p} - \vec{k}|} \frac{M(\vec{k})}{|\vec{B}(\vec{k})|}, \quad (C.8)$$

$$\vec{B}(\vec{p}) = \vec{b}(\vec{p}) + \frac{\alpha}{2\pi} \int d^2k \frac{1}{|\vec{p} - \vec{k}|} \frac{\vec{B}(\vec{k})}{|\vec{B}(\vec{k})|}. \quad (\text{C.9})$$

So, in the case of no Fermi-velocity renormalization the equations for the mass function renormalization becomes equal near the Dirac points (the influence of higher momenta is suppressed in this equation). In the second equation the Fermi-velocity renormalization function remains in the integrand and thus the integral can not be solved analytically anymore. This equation is obviously more sensitive to the higher momenta regime (compare Eq. (C.6) and Eq. (C.7)). So the conclusion of this consideration is that there is no need to expect the same results as obtained from a radial symmetric (if a possible velocity renormalization is included) approach and there is no reason to expect a logarithmic behaviour of the Fermi-velocity renormalization since higher momenta become more important if the Fermi-velocity renormalization is taken into account.

D. Fourier Transform and Convolution Theorem

In the whole work the two-dimensional Fourier transform is defined as

$$\tilde{f}(\vec{r}) = \mathcal{F}^{-1}(f) = \int_{\mathcal{BZ}} \frac{d^2k}{(2\pi)^2} e^{i\vec{k}\vec{r}} f(\vec{k}) \quad (\text{D.1})$$

$$f(\vec{k}) = \mathcal{F}(\tilde{f}) = \int_{\mathcal{AZ}} d^2r e^{-i\vec{k}\vec{r}} \tilde{f}(\vec{r}) \quad (\text{D.2})$$

and can be discretized by using

$$\vec{r}_{ij} = i\vec{a}_1 + j\vec{a}_2 \quad (\text{D.3})$$

$$\vec{k}_{mn} = \frac{m\vec{b}_1 + n\vec{b}_2}{N} \quad (\text{D.4})$$

and $\vec{a}_i \vec{b}_j = 2\pi\delta_{ij}$. So, for the discrete Fourier transform, we get

$$\tilde{f}(\vec{r}) \approx \frac{\mathcal{BZ}}{(2\pi)^2 N^2} \sum_{mn} e^{\frac{2\pi i}{N}(im+jn)} f(\vec{k}_{mn}) = \frac{\mathcal{BZ}}{(2\pi)^2} \mathcal{F}_D^{-1}(f_{mn}), \quad (\text{D.5})$$

$$f(\vec{k}) \approx \mathcal{AZ} \sum_{ij} e^{-\frac{2\pi i}{N}(im+jn)} \tilde{f}(\vec{r}_{ij}) = \mathcal{AZ} \mathcal{F}_D(\tilde{f}_{ij}), \quad (\text{D.6})$$

with $\mathcal{AZ} \cdot \mathcal{BZ} = (2\pi)^2$. The discrete transform is abbreviated by \mathcal{F}_D and exactly equates to what we are numerically calculating with several libraries.

The representation of the discrete Fourier transforms are given by

$$\tilde{f}_{ij} = \frac{1}{N^2} \sum_{mn} e^{\frac{2\pi i}{N}(im+jn)} f(\vec{k}_{mn}) = \mathcal{F}_D^{-1}(f_{mn}) \quad (\text{D.7})$$

$$f_{mn} = \sum_{ij} e^{-\frac{2\pi i}{N}(im+jn)} \tilde{f}(\vec{r}_{ij}) = \mathcal{F}_D(\tilde{f}_{ij}) \quad (\text{D.8})$$

and are usually used in this work.

For a better understanding of the convolution theorem we want to take a look on the integral directly contained in the DSE's (see Eq. (5.27))

$$\int d\vec{q} \mathcal{V}(\vec{k} - \vec{q}) \chi(\vec{q}) = \int d\vec{q} \left(\int d\vec{x} \tilde{\mathcal{V}}(\vec{x}) e^{-i(\vec{k}-\vec{q})\vec{x}} \right) \left(\int d\vec{y} \tilde{\chi}(\vec{y}) e^{-i\vec{q}\vec{y}} \right) \quad (\text{D.9})$$

$$= \int d\vec{x} \int d\vec{y} \tilde{\mathcal{V}}(\vec{x}) \tilde{\chi}(\vec{y}) e^{-i\vec{k}\vec{x}} \int d\vec{q} e^{-i\vec{q}(\vec{y}-\vec{x})} \quad (\text{D.10})$$

$$= \int d\vec{x} \int d\vec{y} \tilde{\mathcal{V}}(\vec{x}) \tilde{\chi}(\vec{y}) e^{-i\vec{k}\vec{x}} (2\pi)^2 \delta(\vec{x} - \vec{y}) \quad (\text{D.11})$$

$$= (2\pi)^2 \int d\vec{x} \tilde{\mathcal{V}}(\vec{x}) \tilde{\chi}(\vec{x}) e^{-i\vec{k}\vec{x}} \quad (\text{D.12})$$

$$= (2\pi)^2 \mathcal{F}[\tilde{\mathcal{V}}(\vec{x}) \cdot \tilde{\chi}(\vec{x})]. \quad (\text{D.13})$$

It was shown that the convolution contained in the DSE's can be written as a Fourier transform of the position space representations of the functions. Analogously this can be calculated for the discrete case but would probably be more confusing.

E. Discrete Potential

Here we want to investigate the different types of interaction introduced in 4.1.1. In position space we have

$$\begin{aligned}
 \mathcal{V}_A(\vec{r}) &= \mathcal{V}(\vec{r}_{ij})|_{(i+j)\%3=0} = \mathcal{V}(\vec{r}_{ij})|_{(i+j)\%3=0}, \\
 \mathcal{V}_B(\vec{r}) &= \mathcal{V}(\vec{r}_{ij} - \vec{\delta})|_{(i+j)\%3=1} = \mathcal{V}(\vec{r}_{ij})|_{(i+j)\%3=0}, \\
 \mathcal{V}_{AB}(\vec{r}) &= \mathcal{V}(\vec{r}_{ij})|_{(i+j)\%3=1} = \mathcal{V}(\vec{r}_{ij})|_{(i+j)\%3=1}, \\
 \mathcal{V}_{BA}(\vec{r}) &= \mathcal{V}(\vec{r}_{ij} - \vec{\delta})|_{(i+j)\%3=0} = \mathcal{V}(\vec{r}_{ij})|_{(i+j)\%3=2},
 \end{aligned} \tag{E.1}$$

since the potential only depends on the distance, the shift of $\vec{\delta}$ (indicating one of the three nearest neighbour vectors) can be absorbed in the restriction of i and j .

For the potential in momentum space we find the following relations

$$\begin{aligned}
 \mathcal{V}_A(\vec{k}) &= \sum_{\vec{r} \in G} \mathcal{V}(\vec{r}_{ij})|_{(i+j)\%3=0} e^{-i\vec{k}\vec{r}} = \sum_{\vec{r} \in A} \mathcal{V}(\vec{r}_{ij}) e^{-i\vec{k}\vec{r}} \\
 &= \sum_{(i+j)\%3=0} \mathcal{V}_{ij} e^{-\frac{2\pi i}{N}(im+jn)} \\
 &= \mathcal{V}_B(\vec{k})
 \end{aligned} \tag{E.2}$$

and

$$\begin{aligned}
 \mathcal{V}_{AB}(\vec{k}) &= \sum_{\vec{r} \in G} \mathcal{V}(\vec{r}_{ij})|_{(i+j)\%3=1} e^{-i\vec{k}\vec{r}} = \sum_{\vec{r} \in G} \mathcal{V}(\vec{r} + \vec{\delta})|_{(i+j)\%3=0} e^{-i\vec{k}\vec{r}} \\
 &\stackrel{r \rightarrow r - \vec{\delta}}{=} e^{i\vec{k}\vec{\delta}} \sum_{\vec{r} \in G} \mathcal{V}(\vec{r})|_{(i+j)\%3=0} e^{-i\vec{k}\vec{r}} = e^{i\vec{k}\vec{\delta}} \mathcal{V}_A(\vec{k}).
 \end{aligned} \tag{E.3}$$

for the potential in momentum space.

Similarly we find

$$\mathcal{V}_{BA}(\vec{k}) = e^{-i\vec{k}\vec{\delta}} \mathcal{V}_A(\vec{k}). \tag{E.4}$$

That exactly agrees with the required symmetry transformations from Eq. (7.12) but has not been numerically included in our calculation yet.

References

- [1] P. R. Wallace, “The band theory of graphite,” *Phys. Rev.*, **71**, 622–634 (1947).
- [2] A. K. Geim and K. S. Novoselov, “The rise of graphene,” *Nature Materials*, **6** (3), 183–191 (2007).
- [3] K. S. Novoselov, A. K. Geim, S. V. Morozov, D. Jiang, Y. Zhang, S. V. Dubonos, I. V. Grigorieva, and A. A. Firsov, “Electric field effect in atomically thin carbon films,” *Science*, **306** (5696), 666–669 (2004), <http://www.sciencemag.org/content/306/5696/666.full.pdf>.
- [4] A. H. Castro Neto, F. Guinea, N. M. R. Peres, K. S. Novoselov, and A. K. Geim, “The electronic properties of graphene,” *Rev. Mod. Phys.*, **81**, 109–162 (2009).
- [5] V. N. Kotov, B. Uchoa, V. M. Pereira, F. Guinea, and A. H. Castro Neto, “Electron-electron interactions in graphene: Current status and perspectives,” *Rev. Mod. Phys.*, **84**, 1067–1125 (2012).
- [6] V. P. Gusynin, S. G. Sharapov, and J. P. Carbotte, “Ac conductivity of graphene: From tight-binding model to 2 + 1-dimensional quantum electrodynamics,” *International Journal of Modern Physics B*, **21** (27), 4611–4658 (2007), <http://www.worldscientific.com/doi/pdf/10.1142/S0217979207038022>.
- [7] O. Gamayun, E. Gorbar, and V. Gusynin, “Gap generation and semimetal-insulator phase transition in graphene,” *Phys. Rev. B*, **81**, 075429 (2010).
- [8] C. Popovici, C. S. Fischer, and L. von Smekal, “Effects of electron-electron interactions in suspended graphene,” *Proceedings of Science*, (**Confinement X**), 269–276 (2013).
- [9] D. Smith and L. von Smekal, “Monte carlo simulation of the tight-binding model of graphene with partially screened coulomb interactions,” *Phys. Rev. B*, **89**, 195429 (2014).
- [10] D. Elias, R. Gorbachev, A. Mayorov, S. Morozov, A. Zhukov, P. Blake, L. Ponomarenko, I. Grigorieva, K. Novoselov, F. Guinea, et al., “Dirac cones reshaped by interaction effects in suspended graphene,” *Nature Physics*, **7** (9), 701–704 (2011).
- [11] T. O. Wehling, E. Şaşıoğlu, C. Friedrich, A. I. Lichtenstein, M. I. Katsnelson, and S. Blügel, “Strength of effective coulomb interactions in graphene and graphite,” *Phys. Rev. Lett.*, **106**, 236805 (2011).
- [12] P. V. Buividovich and M. I. Polikarpov, “Monte carlo study of the electron transport properties of monolayer graphene within the tight-binding model,” *Phys. Rev. B*, **86**, 245117 (2012).
- [13] M. V. Ulybyshev, P. V. Buividovich, M. I. Katsnelson, and M. I. Polikarpov, “Monte carlo study of the semimetal-insulator phase transition in monolayer graphene with a realistic interelectron interaction potential,” *Phys. Rev. Lett.*, **111**, 056801 (2013).
- [14] O. Gamayun, E. Gorbar, and V. Gusynin, “Supercritical coulomb center and excitonic instability in graphene,” *Phys. Rev. B*, **80**, 165429 (2009).

- [15] C. Popovici, C. S. Fischer, and L. von Smekal, “Fermi velocity renormalization and dynamical gap generation in graphene,” *Phys. Rev. B*, **88**, 205429 (2013).
- [16] T. Stauber and G. Gómez-Santos, “Dynamical current-current correlation of the hexagonal lattice and graphene,” *Phys. Rev. B*, **82**, 155412 (2010).
- [17] N. Ashcroft and D. Mermin, *Festkörperphysik* (Oldenbourg Wissenschaftsverlag, 2012).
- [18] M. E. Peskin and D. V. Schroeder, *An introduction to Quantum Field Theory* (Westview Press, 1995).
- [19] V. P. Gusynin, V. A. Miransky, S. G. Sharapov, and I. A. Shovkovy, “Excitonic gap, phase transition, and quantum hall effect in graphene,” *Phys. Rev. B*, **74**, 195429 (2006).
- [20] E. V. Gorbar, V. P. Gusynin, V. A. Miransky, and I. A. Shovkovy, “Magnetic field driven metal-insulator phase transition in planar systems,” *Phys. Rev. B*, **66**, 045108 (2002).
- [21] M. R. Pennington, “Swimming with quarks,” Lecture at the XI. Mexican School of Particles and Fields (2004).
- [22] R. Alkofer and L. von Smekal, “The infrared behaviour of {QCD} green’s functions: Confinement, dynamical symmetry breaking, and hadrons as relativistic bound states,” *Physics Reports*, **353** (5–6), 281 – 465 (2001).
- [23] R. Williams, *Schwinger-Dyson Equations In QED and QCD*, Ph.D. thesis, University of Durham (2007).
- [24] C. S. Fischer, “Dynamical chiral symmetry breaking in unquenched qed3,” *Phys. Rev.*, **D 70** (2004).
- [25] J. González, F. Guinea, and M. Vozmediano, “Non-fermi liquid behavior of electrons in the half-filled honeycomb lattice (a renormalization group approach),” *Nuclear Physics B*, **424** (3), 595 – 618 (1994).
- [26] W. Greiner and J. Reinhardt, *Feldquantisierung: ein Lehr- und Übungsbuch ; mit zahlreichen Beispielen und Aufgaben mit ausführlichen Lösungen*, *Theoretische Physik : ein Lehr- und Übungsbuch* (Deutsch, 1993).
- [27] F. Schwabl, *Quantenmechanik für Fortgeschrittene (QM II)*, Springer-Lehrbuch (Springer-Verlag, 2008).
- [28] W. H. Press, S. A. Teukolsky, W. T. Vetterling, and B. P. Flannery, *Numerical Recipes-The Art of scientific Computing* (Cambridge University Press, 2007).
- [29] H. Schwarz and N. Köckler, *Numerische Mathematik*, Vieweg Studium (Vieweg+Teubner Verlag, 2009).
- [30] G. Bärwolff, *Numerik für Ingenieure, Physiker und Informatiker: für Bachelor und Diplom, Für Bachelor und Diplom* (Spektrum Akademischer Verlag, 2006).
- [31] A. Munshi, B. Gaster, T. G. Mattson, J. Fung, and D. Ginsburg, *OpenCL Programming Guide* (Addison-Wesley Professional, 2011), 1st edition.

- [32] B. Gaster, L. Howes, D. R. Kaeli, P. Mistry, and D. Schaa, *Heterogeneous Computing with OpenCL* (Morgan Kaufmann Publishers Inc., San Francisco, CA, USA, 2011), 1st edition.
- [33] M. Frigo and S. G. Johnson, “The design and implementation of FFTW3,” *Proceedings of the IEEE*, **93** (2), 216–231 (2005).
- [34] V. A. Miransky and K. Yamawaki, “Conformal phase transition in gauge theories,” *Phys. Rev. D*, **55**, 5051–5066 (1997).
- [35] A. Emelyanenko and L. Boinovich, “On the effect of discrete charges adsorbed at the interface on nonionic liquid film stability: charges in the film,” *Journal of Physics: Condensed Matter*, **20** (49), 494227 (2008).
- [36] I. F. Herbut, “Interactions and phase transitions on graphene’s honeycomb lattice,” *Phys. Rev. Lett.*, **97**, 146401 (2006).
- [37] C. Honerkamp, “Density waves and cooper pairing on the honeycomb lattice,” *Phys. Rev. Lett.*, **100**, 146404 (2008).
- [38] D. Mesterházy, J. Berges, and L. von Smekal, “Effect of short-range interactions on the quantum critical behavior of spinless fermions on the honeycomb lattice,” *Phys. Rev. B*, **86**, 245431 (2012).
- [39] L. von Smekal, “Universal aspects of qcd-like theories,” *Nuclear Physics B - Proceedings Supplements*, **228**, 179 – 220 (2012).
- [40] B. Dietz, F. Iachello, M. Miski-Oglu, N. Pietralla, A. Richter, L. von Smekal, and J. Wambach, “Lifshitz and excited-state quantum phase transitions in microwave dirac billiards,” *Phys. Rev. B*, **88**, 104101 (2013).
- [41] J. González, F. Guinea, and M. Vozmediano, “The electronic spectrum of fullerenes from the dirac equation,” *Nuclear Physics B*, **406** (3), 771 – 794 (1993).

Selbstständigkeitserklärung

Hiermit versichere ich, die vorgelegte Thesis selbstständig und ohne unerlaubte fremde Hilfe und nur mit den Hilfen angefertigt zu haben, die ich in der Thesis angegeben habe. Alle Textstellen, die wörtlich oder sinngemäß aus veröffentlichten Schriften entnommen sind, und alle Angaben die auf mündlichen Auskünften beruhen, sind als solche kenntlich gemacht. Bei den von mir durchgeführten und in der Thesis erwähnten Untersuchungen habe ich die Grundsätze guter wissenschaftlicher Praxis, wie sie in der 'Satzung der Justus-Liebig-Universität zur Sicherung guter wissenschaftlicher Praxis' niedergelegt sind, eingehalten. Gemäß § 25 Abs. 6 der Allgemeinen Bestimmungen für modularisierte Studiengänge dulde ich eine Überprüfung der Thesis mittels Anti-Plagiatssoftware.

Ort, Datum

Unterschrift

